Report, Published Version

Rahlf, Holger; Benndorf, Julia; Naulin, Marie

MudEstuary Die Beeinflussung der Dynamik der Tideästuare durch Flüssigschlick : MudEstuary_B Numerische Simulation des Emsästuars ; Förderkennzeichen 03KIS113. FuE-Abschlussbericht B3955.03.04.70235

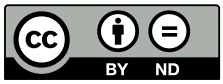

BAW
Bundesanstalt für Wasserbau

MudEstuary
Die Beeinflussung der Dynamik der Tideästuare durch Flüssigschlick

MudEstuary_B
Numerische Simulation des Emsästuars

Förderkennzeichen 03KIS113
BAW-Nr. B3955.03.04.70235

GEFÖRDERT VOM

Bundesministerium
für Bildung
und Forschung

März 2020

Kompetenz für die Wasserstraßen

FuE-Abschlussbericht
MudEstuary_B
B3955.03.04.70235

GEFÖRDERT VOM

Bundesministerium
für Bildung
und Forschung

Der Verantwortung für den Inhalt dieser Veröffentlichung liegt beim Autor.

Client:	Kuratorium für Forschung im Küsteningenieurwesen (KFKI) Bundesministerium für Bildung und Forschung (BMBF) Projektträger Jülich (PtJ)
Order Date:	July 2015 Az.: 03KIS113 (MudEstuary_B)
Order Number:	BAW-No. B3955.03.04.70235

Prepared by:	Department:	Hydraulic Engineering in Coastal Areas
	Section:	Estuary Systems II (K3)
	Project leader:	Holger Rahlf
	Responsible person:	Julia Benndorf, Marie Naulin

Hamburg, March 2020

Bundesanstalt für Wasserbau

Postfach 21 02 53 · 76152 Karlsruhe
Tel.: (0721) 97 26 – 0

Wedeler Landstraße 157 · 22559 Hamburg
Tel.: (0 40) 8 19 08 – 0

Zusammenfassung

In Küstengewässern und Ästuaren kann die Bildung von Flüssigschlick zu ökonomischen und ökologischen Beeinträchtigungen führen. Dabei versteht man unter Flüssigschlick eine hoch konzentrierte, wässrige Suspension aus feinsten Sedimenten und organischen Bestandteilen. Die Akkumulation von Flüssigschlick in Ästuaren, Hafenanlagen und küstennahen Bereichen beeinflusst die Tidedynamik und hat erhebliche Auswirkungen auf den Ausbau und Unterhaltungsmaßnahmen der Bundeswasserstraßen. Neben ökonomischen Aspekten wirkt sich die Verschlickung der Gewässer auch auf die Ökologie aus und führt zu einer Verschlechterung des ökologischen Zustands.

Um zukünftige Unterhaltungsmaßnahmen und Renaturierungsvorhaben entwickeln und planen zu können, ist vertieftes Verständnis zum Einfluss der Flüssigschlickbildung auf die Tidedynamik und umgekehrt nötig. Dabei sollen die aktuellen Simulationsmethoden weiterentwickelt werden, um den Einfluss von Flüssigschlick für die Wirkungsprognosen von Unterhaltungs- und Renaturierungsmaßnahmen berücksichtigen zu können.

Im BMBF Vorgängerprojekt „MudSim_A“ wurde an der Universität der Bundewehr (UniBw) München das viskoelastische Fließverhalten von Ems-Schlick untersucht und eine Parametrisierung der rheologischen Viskosität durchgeführt. Währenddessen wurde im Teilprojekt „MudSim_B“ an der Bundesanstalt für Wasserbau (BAW) in Hamburg ein numerisches Modell entwickelt, welches Schlickströmungen durch eine isopyknische vertikale Auflösung modelliert. Eine Erkenntnis des Projekts ist die bis dato fehlende Kopplung des rheologischen Fließens mit der Turbulenz der darüber fließenden Wassersäule. Insbesondere der Übergang von „freier“ Turbulenz zu gedämpfter Turbulenz und letztendlich zu laminarem Fließen kann durch herkömmliche Turbulenzmodelle bisher nicht dargestellt werden.

Vom 01.06.2015 bis 30.06.2019 hat das BMBF Nachfolgeprojekt „MudEstuary“ diese Fragestellung experimentell und numerisch untersucht. Das Projekt „MudEstuary“ ist ebenfalls ein Verbundprojekt, das wiederum gemeinsam mit der UniBw München und der BAW in Hamburg bearbeitet wurde. Dafür ist das Gesamtprojekt in die Teilprojekte „MudEstuary_A“ an der UniBw München und „MudEstuary_B“ bei der BAW in Hamburg unterteilt. Dieser Abschlussbericht bezieht sich auf das Teilprojekt „MudEstuary_B“.

Während der Fokus in „MudEstuary_A“ auf experimentellen Laborversuchen zum turbulenten Verhalten von granularen Suspensionen bestand, lag der Schwerpunkt von „MudEstuary_B“ in der Weiterentwicklung eines numerischen 3D-Modells und einer Anwendung auf das Emsästuar. Die Grundlage dieser Untersuchungen ist ein Modellansatz, der mit Hilfe einer effektiven Viskosität einen grenzfreien Übergang von freier Turbulenz zu rheologischem, laminaren Fließen ermöglicht und im Folgenden „kontinuierlicher Modellansatz“ genannt wird. Das Ziel von „MudEstuary_B“ lag darin, diesen Ansatz im dreidimensionalen hydrodynamisch-numerischen Modell zu implementieren.

Für das Teilprojekt MudEstuary_B war folgendes Arbeitsprogramm erforderlich:

Arbeitspaket 1
AP 1.1: Konzeption und Literaturrecherche
AP 1.2: Weiterentwicklung Simulationsmodell

Für eine effiziente Konzeption und Weiterentwicklung des 3D-Modells wurde zusätzlich im ersten Projektjahr ein numerisches 1DV-Modell gemeinsam im Verbundprojekt entwickelt. In dieses Modell wurde der kontinuierliche Modellansatz implementiert, sodass erste Ergebnisse damit berechnet werden konnten. Vor- und Nachteile des neuen Ansatzes wurden aufgrund der kurzen Rechenzeiten im 1D-Modell somit sofort sichtbar, so dass eine effiziente Optimierung erfolgen konnte, bevor der Ansatz in das 3D-Modell überführt wurde.
Für den erweiterten kontinuierlichen Modellansatz wurden eine Formulierung für behindertes Absinken nach van Rijn (1993), die rheologische Viskosität nach Knoch und Malcherek (2011), die Beschreibung der effektiven Viskosität als Summe aus turbulenter rheologischer Viskosität und sowie ein angepasstes k-ω-Turbulenzmodell mit entsprechenden Randbedingungen implementiert.

Arbeitspaket 2
AP 2.1: Anwendung Simulation auf Labormodell
AP 2.2: Anwendung schematisches Ästuarmodell ~~(Anwendung Emsmodell)~~
AP 2.3: Integration Viskositätsmodell

Im zweiten Arbeitspaket wurden die experimentell gewonnenen Ergebnisse in einem numerischen 3D-Modell nachgebildet. Dabei lag der Fokus besonders auf der Implementierung der mit dem neu entwickelten kontinuierlichen Modellansatz einhergehenden neuen Simulationsmethoden wie z.B. der Integration des Viskositätsmodells. Dafür wurden Module für das Simulationsprogramm UnTRIM in FORTRAN neu programmiert oder erweitert. Das Konzept des kontinuierlichen Modellansatzes bringt neue Herausforderungen an die bestehenden numerischen Simulationsmethoden mit sich. Im Verbundprojekt MudEstuary wurden die benötigten numerischen Methoden herausgearbeitet und sowohl in 1DV, wie auch in 3D-Modellen getestet. Eine erfolgreiche Anwendung des 3D-Modells konnte für die numerische Simulation des Labormodells und eines schematischen Ästuarmodells realisiert werden. Für diese Fälle wurden Parameterstudien zur Untersuchung der rheologischen Viskosität durchgeführt.
Da die neuen Simulationsmethoden jedoch eine hohe Rechenleistung benötigen sowie die Bildung und die Dynamik von Flüssigschlick ein sensitives Zusammenspiel diverser Prozesse und Effekte ist und noch keine Validierungsdaten existieren, war eine Anwendung auf Natursysteme wie dem Emsästuar zurzeit nicht zielführend. Dies ist jedoch im weiteren Verlauf der Arbeiten im Rahmen von eigenfinanzierten Nachfolgeprojekten (Ressortforschung) vorgesehen.

Arbeitspaket 3
AP 3.1 Anwendung Emsmodell und historische Zustände
AP 3.2 Untersuchung der Ursache der Verschlickung

Im dritten Arbeitspaket lag der Schwerpunkt auf der Ermittlung der Ursachen der Verschlickung von Ästuaren. Hierfür erfolgten numerische Simulationen mit einem klassischen hydrodynamischen 3D-Modell. Es wurden umfangreiche historische Daten zu Bathymetrien und weiteren Daten gesichtet, aufbereitet und bewertet.
Aus diesen Daten wurden drei Szenarien herausgearbeitet, welche anschließend in 3D-Modellen simuliert wurden. Diese repräsentieren die 1930er Jahre, eine Zeit vor vielen maßgeblichen anthropogenen Veränderung, die 1980er Jahre, während der Ausbauarbeiten, und 2015 als aktuellen Zustand.
Diese Szenarienbetrachtung der historischen Zustände des Emsästuars liefert einen wertvollen Beitrag zur Ermittlung der Ursachen der Verschlickung. Es wurden die Einflüsse von Topographie, Sohlrauheit sowie Meeresspiegelanstieg untersucht. All diese Aspekte haben allein schon maßgebliche Auswirkungen auf die Hydrodynamik, doch nur durch die Überlagerung, zusammen mit der erhöhten Verfügbarkeit von Sedimenten z. B. durch veränderte Baggerstrategien, wurden die Voraussetzungen für eine Verschlickung nach van Rijn und Grasmeijer (2018) erfüllt. Auch die Strömungsgeschwindigkeiten haben sich im Laufe der Zeit durch anthropogene Maßnahmenverändert, sodass insbesondere bei niedrigen Oberwasserzuflüssen der Flutstrom stärker ist als der Ebbstrom und so den Sedimenteintrag begünstigt. Die Untersuchung der historischen Entwicklung anhand des Tideprismas zeigte, dass sich das Verhältnis von Einlassquerschnitt zu Tidevolumen im Emsästuar im Vergleich zu den empirischen Formeln von O'Brien (1969) nicht ausgeglichen verändert hat. Dies deutet auf ein System hin, welches sich nicht im Gleichgewicht befindet.

Die Erkenntnisse des Projekts MudEstuary wurden in die Simulationssoftware der Bundesanstalt für Wasserbau implementiert, mit der sie für die zukünftige numerische Simulation der Küsten und Ästuare angewendet werden können. Diese Programmbausteine sollen an der BAW in einem nachfolgenden eigenfinanzierten Ressortforschungsprojekt weiterentwickelt und angewandt werden, wobei der Fokus auf der Anwendung des erweiterten Modellverfahrens auf das Emsästuar liegen soll. Im Rahmen dieses Abschlussberichtes sowie zahlreicher Veröffentlichungen und Vorträgen bei nationalen und internationalen Konferenzen und Workshops werden die Ergebnisse außerdem der Öffentlichkeit zur Verfügung gestellt.

Da das Emsästuar nicht nur eine deutsche Bundeswasserstraße ist, sondern auch die niederländisch-deutsche Grenze umfasst und somit die Forschung und Entwicklung in dieser Region von internationaler Bedeutung ist, wurde dieser Abschlussbericht in englischer Sprache verfasst.

Eine ausführliche Beschreibung des Vorgehens sowie der Ergebnisse von MudEstuary_B ist in englischer Sprache in diesem Abschlussbericht zu finden.

Summary

In coastal waters and estuaries, the formation of fluid mud can lead to economic and ecological damage. Fluid mud is a highly concentrated, aqueous suspension of finest sediments and organic components. The accumulation of fluid mud in estuaries, port facilities and coastal areas influences the tidal dynamics and has considerable effects on the development and maintenance of the federal waterways. In addition to economic aspects, the increase of fluid mud in the waterways also has an impact on the ecology and leads to a deterioration of the ecological status.

In order to be able to develop and plan future maintenance and renaturation measures, a deeper understanding of the influence of fluid mud formation on tidal dynamics and vice versa is necessary. Current simulation methods should be extended in order to take the influence of fluid mud into account.

In the preceding BMBF project "MudSim_A", the viscoelastic flow behavior of Ems mud was investigated at the University of the Federal Armed Forces (UniBw) Munich and a parameterization of the rheological viscosity was carried out. Meanwhile, in the sub-project "MudSim_B" at the Federal Waterways Engineering and Research Institute (BAW) in Hamburg, a numerical model was developed which simulates mud flows by an isopycnical vertical resolution. One of the findings of the project is the lack of coupling between the rheological flow and the turbulent flow of the water column above. Especially the transition from "free" turbulence to damped turbulence and finally to laminar flow cannot be represented by conventional turbulence models.

On June 1, 2015, the follow-up BMBF project "MudEstuary“ began to investigate this issue experimentally and numerically. The "MudEstuary" project is also a collaborative project, carried out jointly by the UniBw Munich and the BAW in Hamburg. For this purpose, the overall project is divided into the subprojects "MudEstuary_A" at the UniBw Munich and "MudEstuary_B" at the BAW in Hamburg. This report refers to the subproject "MudEstuary_B".

While the focus in "MudEstuary_A" was on experimental laboratory tests on the turbulent behavior of granular suspensions, the focus of "MudEstuary_B" was on the further development of a numerical 3D model and an application to the Ems estuary. The basis of these investigations is a so called “continuous model approach”, which allows a borderless transition from free turbulence to rheological, laminar flow by means of an effective viscosity.

The following work program was assembled for the subproject MudEstuary_B:

Work package 1
WP 1.1: concept and literature review
WP 1.2: further development of simulation model

For an efficient conception of the further development of the 3D model, a numerical 1DV model was additionally developed jointly by the project partners in the first year of the project. The

continuous model approach was implemented in this model, so that first results could be calculated. Advantages and disadvantages of the approach became immediately visible due to the short computing times of the 1D model. Hence, an efficient optimization could take place before the approach was transferred to the 3D model.

Work package 2:
WP 2.1: application laboratory model
WP 2.2: application schematic estuary ~~(Application Ems Estuary)~~
WP 2.3: integration viscosity model

In the second work package the experimentally obtained results were reproduced in a suitable numerical 3D model. The focus was especially on the implementation of the new simulation methods associated with the continuous model approach. The concept of the continuous model approach brings new challenges to the existing numerical simulation methods. In the joint project MudEstuary, the required numerical methods were worked out and tested in 1DV as well as in 3D models. A successful application of the 3D model could be realized for the numerical simulation of the laboratory model and a schematic estuary model. However, since the new simulation methods require high computing power and the formation and dynamics of fluid mud is interplay of various processes and effects, for which the parameters are sensitive and validation data do not yet exist, an application to a nature system such as the Ems estuary was at this time not feasible.

Work package 3:
WP 3.1: application ems estuary
WP 3.2: investigation of the causes of siltation

The third work package focused on identifying the causes of siltation in estuaries. For this purpose numerical simulations with a classical hydrodynamic 3D model were carried out. Extensive historical data on bathymetries and other data were sighted and processed. This scenario analysis of the historical conditions of the Ems estuary provides a valuable contribution to the determination of the causes of the formation and increase of fluid mud.

The results of MudEstuary_B are summarized in this report.

Table of contents

List of figures

Page

List of tables

Page

I Tidal dynamics with fluid mud

1 Motivation and objectives

1.1 Motivation

Fluid mud is a high concentration aqueous suspension of fine-grained sediment and is often associated with a lutocline, a sudden change in sediment concentration with depth. Fluid Mud typically forms in near-bottom layers in lakes and estuaries, but can occur in any water body with sufficient fine-sediment supply and periods of low intensity flow (McAnally et al. 2007).

The occurrence of fluid mud can lead to high maintenance costs of waterways such as estuaries, e.g. for dredging, prevention of pollutant propagation and nature conservation. In Germany in particular the Ems Estuary is affected by fluid mud: high fine-sediment concentrations up to 300 kg/m^3 and fluid mud layers up to a thickness of 2 m were measured by Schrottke (2006).

Furthermore, fluid mud may lead to a change in tidal dynamics. The flow behavior of high-concentration fine sediment suspensions is non-Newtonian. As a consequence in classical hydrodynamic-numerical models, the applied Reynolds equations for Newtonian flow behavior are not suitable to model the fluid mud dynamics.

Therefore enhanced predictive methods are needed for a description of the interaction between tidal dynamics and fluid mud. The long-term objective is the development of a predictive engineering tool required for maintenance strategies of estuaries in order to minimize siltation and thus lower the economic and ecological costs.

1.2 Theoretical background

In classical hydrodynamic-numerical models for large-scale applications, e.g. in coastal engineering, the interaction between tidal dynamics and fluid mud are barely considered so far. Among the first solutions a two-dimensional model was developed by H.R. Wallingford (Crapper and Ali 1997). Furthermore, in the Delft3D software package a module for the simulation of fluid mud has been integrated (Winterwerp et al. 2002) and extended by a mud buffer model (van Kessel et al. 2011). However, these models are not applicable for the simulation of the rheological behavior of fluid mud.

Methods to simulate the fluid mud dynamics were further developed by Knoch and Malcherek (2011) and Wehr (2012). The complex non-Newtonian behavior of fluid mud was simulated by an isopycnal numerical model. Therefore, the shear-thinning flow behavior of fluid mud and the rheometrical investigation of the yield stress were analyzed. This model describes the complex rheological properties of fluid mud. However, the vertical interaction of individual layers under consideration of the turbulence has not yet been analyzed. Another approach to simulate the dynamics of fluid mud was developed by Roland et al. (2012): the FLMUD module is based on

Cartesian coordinates. The module was validated qualitatively by numerical experiments. However, a detailed validation and application to an estuary are still needed.

As stated in Burchard et al. (2018): *"Le Hir et al. (2001), Winterwerp (2001), and Winterwerp et al. (2006) developed one-dimensional point models containing some of the processes mentioned above in order to study the temporal dynamics of SPM stratification and the formation of lutoclines in a water column. These water column models were able to qualitatively reproduce the observed behavior of SPM stratification in estuaries by including SPM-induced turbulence damping and hindered settling effects. One of the current challenges is to extend the above models beyond one-dimensional models while resolving the flow-turbidity feedbacks, hindered settling, and flocculation processes accurately enough. In addition, accurately describing the bottom boundary conditions, especially in the presence of fluid mud, remains challenging."*

1.3 Objectives

The main objective is to develop and analyze a method describing the interaction of tidal dynamics and fluid mud with an application to the Ems Estuary.

Therefore, a numerical model based on the continuous modelling approach (Le Hir et al. 2001) is suited. This modelling approach is extended by a rheological viscosity and an adapted k-ω turbulence model. Hence, the model simulates the water column as well as a fluid mud layer with one set of momentum, transport and turbulence model equations. The model is able to recognize automatically whether the flow is turbulent, laminar or motionless due to high concentrations of suspended matter. Therefore, the viscous behavior of water is represented by turbulence models, e.g. k-omega model, and the viscous-elastic behavior of fluid mud is represented by rheological models.

For this purpose, the continuous modelling approach was at first implemented in a numerical 1DV model which was additionally developed jointly by the project partners in the first year of the project (MudEstuary_A&B). After an efficient testing of the method, this modelling approach should be transferred into a three-dimensional scale in MudEstuary_B.

Malcherek et al. (2017) developed

This comprises the following steps

- Extended set-up of 3D numerical model including
    - continuous model concept in momentum equations
    - rheological viscosity
    - flocculation and hindered settling
    - adapted boundary conditions for the turbulence model
- Application examples: laboratory flume and schematic estuary
- Investigation of causes of siltation by historic scenarios of Ems Estuary

1.4 Work packages and structure of this report

The work packages (WP) of MudEstuary_B were defined as follows:

Work package 1
WP 1.1: concept and literature review
WP 1.2: further development of simulation model

Work package 2:
WP 2.1: application laboratory model
WP 2.2: application schematic estuary ~~(Application Ems Estuary)~~
WP 2.3: integration viscosity model

Work package 3:
WP 3.1: application Ems Estuary
WP 3.2: investigation of the causes of siltation

The structure of this report and the associated work packages are shown in Figure 1.

Part I of this report includes an introduction on tidal dynamics with fluid mud. After the motivation and objectives a brief overview of in-situ observations of the Ems Estuary is given in order to show the current situation of fluid mud dynamics in the estuary. Furthermore, a short summary of the experiments of the laboratory flume is given which was part of MudEstuay_A. Since a comparison with the results between laboratory and numerics will be made later, the experimental setup will be explained briefly.

For WP 1 the results can be found at different places in this report: The concept as motivation and objectives is described in the introduction of part I. The results of the literature review are given in the respective thematic sections of the chapters, i.e. for mathematic descriptions in section 5 of part II and for the historic development of the Ems estuary in section 7 of part III as well as in appendix 12.

In part II of this report the results of WP 2, i.e. the extended continuous modelling concept with application examples of the laboratory flume and a schematic estuary, are summarized.

Part III includes the results of WP 3, i.e. the historic scenarios of the Ems Estuary with an application to the Ems Estuary and an investigation of the causes of siltation.

Finally, an overall summary and future prospects are discussed in the conclusion in part IV of this report.

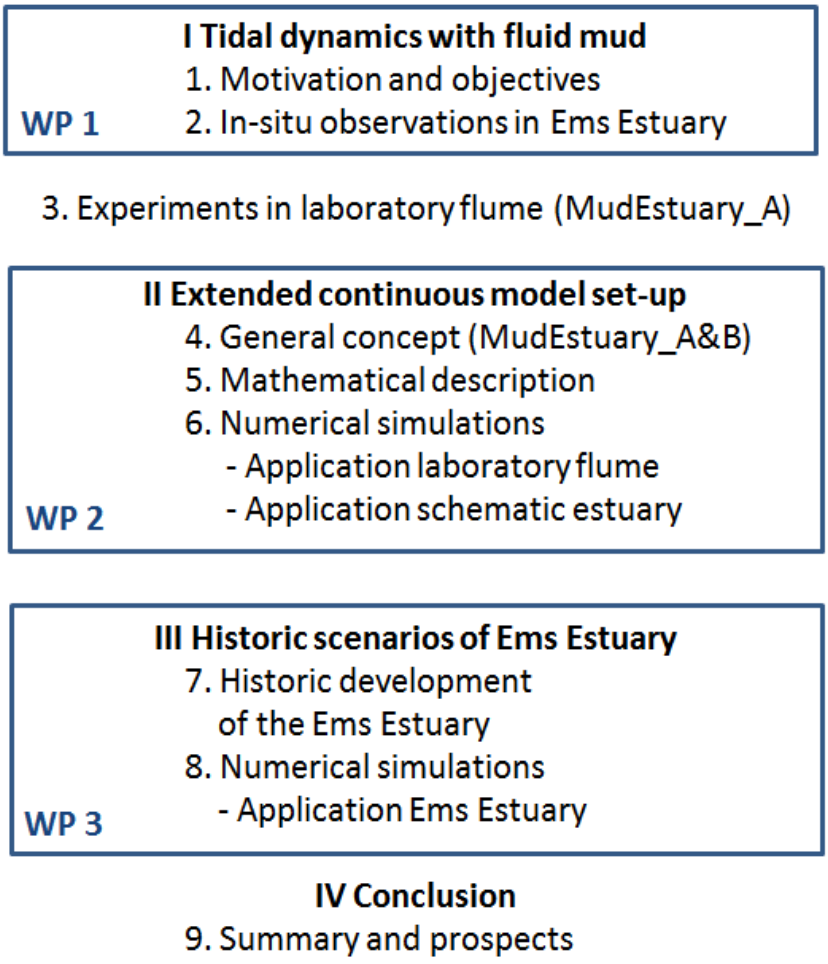

Figure 1: Structure of report and associated work packages (WP).

2 In-situ observations in Ems Estuary

In-situ observations of the high concentrated mud suspensions in the Ems Estuary are an important component for phenomenological descriptions of processes as well as for the verification and validation of numerical simulations. In the following chapter a brief overview of in-situ observations of longitudinal profiles (section 2.1) as well as vertical profiles (section 2.2) is given.

2.1 Longitudinal profiles

In order to determine the fluid mud distribution in the Ems estuary, regular measurements of longitudinal cross sections with ADCP (15 Hz, 38 Hz, 200 Hz) are carried out by FSK NLWKN. In Figure 2 the fluid mud distributions in the Ems estuary at low and high discharge are shown. Wurpts (9/25/2017) identified a discharge threshold of 80 m^3/s, at which the fluid mud from Papenburg to Leerort is increasingly displaced downstream the estuary. At high discharge rates the fluid mud layer ends at the seaward end of the Emder fairway (Knock).

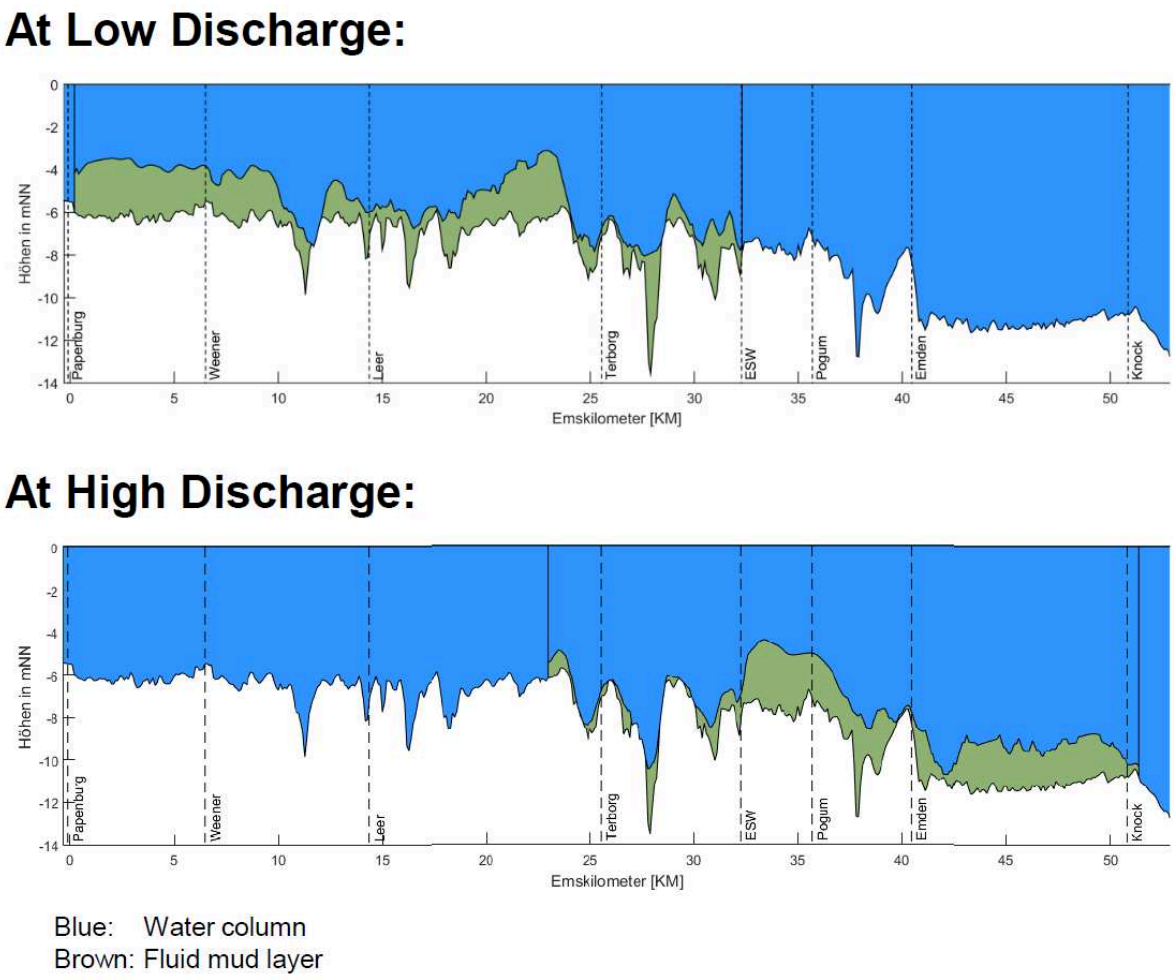

Figure 2: Fluid mud distribution in the Ems estuary at low (< 80 m^3/s) and high discharge (> 80 m^3/s) (Wurpts 9/25/2017).[1]

2.2 Vertical profiles

Sediment-induced stratification and density currents in the Ems estuary were observed by Becker et al. (2018). The in-situ observations were carried out in the center of the estuarine turbidity zone (at Jemgum) at the edge of the fairway in November 2014. Prior to the start of the measurements there was a longer period of low discharge (< 60 m^3/s). Until shortly before and during the measurements the discharge conditions were moderate (120 m^3/s). This could indicate that there has been a flush leading to a mobilization of fluid mud and a shifting of the estuarine turbidity zone downstream towards Emden.

[1] The direction of the longitudinal profile deviates from the other shown longitudinal profiles; here direction from weir (left) to sea (right)

For the ship-based measuring campaign the following instruments were applied:

- CTD-OBS combination (conductivity temperature depth - optical back scatter)
- ADCP (acoustic Doppler current profiler)
- SES (sediment echo sounder)
- ECM (electromagnetic current meter)

The results show the vertical profile of the water column and the variability of sediment-induced stratification (Figure 3, Figure 4).

In Figure 3 the vertical distribution is shown for

a) velocity magnitude and salinity
   (plot: ADCP current velocity [m/s]; dots: ECM current velocity [m/s]; bars: salinity [PSU])
b) SSC and max. vertical SSC gradient
   (plot: OBS interpolated SSC [g/l], dots: max. vertical SSC gradient [g/(lm)]; dashed lines: OBS measurements)
c) SES intensity including isolutals (derived from OBS) [g/l]

In Figure 4 the vertical distribution is shown for

a) acceleration $\Delta u/\Delta t$ [m/(s h)] including isolutals [g/l]
b) vertical velocity shear [1/s] including isolutals [g/l]
c) gradient Richardsen number [-]

The reversal of the direction of the flow, i.e. from flood- to ebb directed and vice versa, is indicated by white lines in Figure 3 (a, b) and in Figure 4 (a, b).

Moreover, particular stages of stratification are highlighted by Roman numerals:

(I) beginning of the flood: entrainment and vertical mixing;
(II) middle of flood: restratification;
(III) around high water: full stratification;
(IV) later ebb phase: stratification with shear dispersion;
(V) ebb slack water: short settling phase.

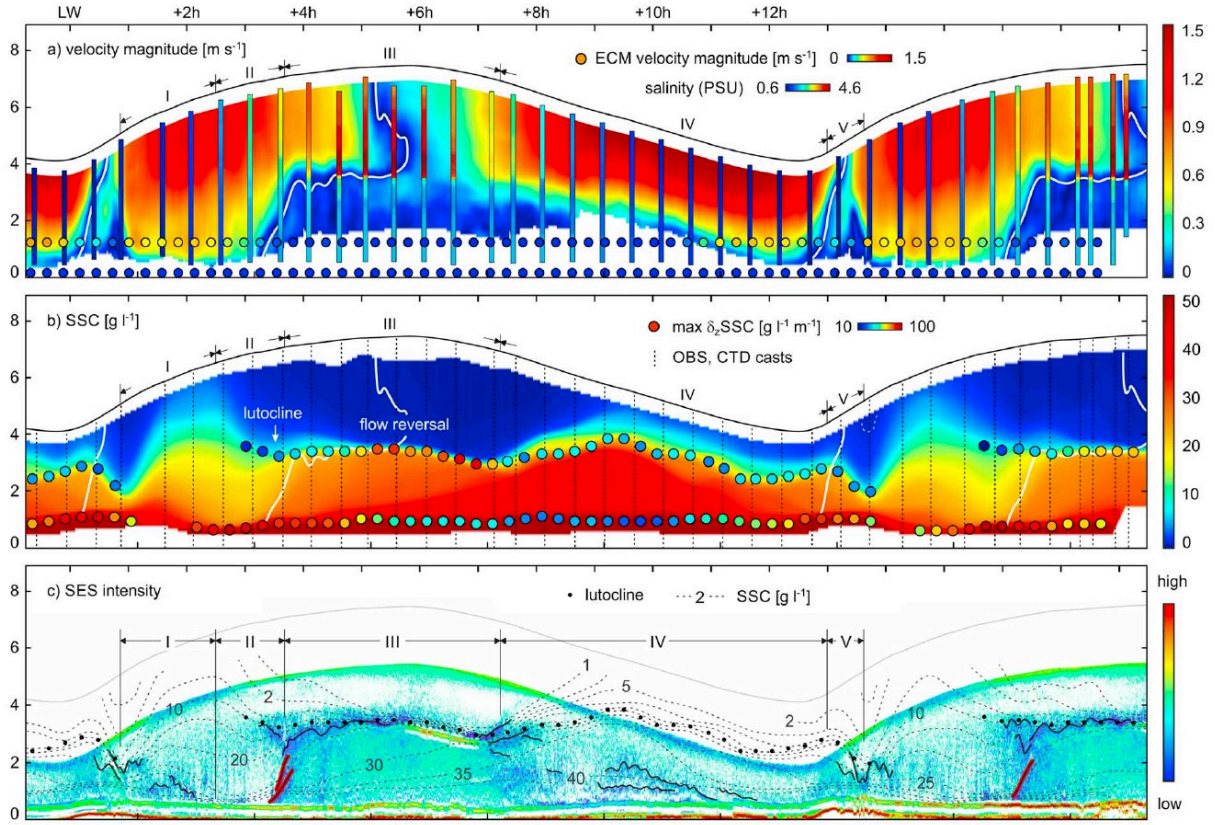

Figure 3: Velocity and stratification a) velocity magnitude, b) SSC, and c) SES intensity at Jemgum in November 2014 (Becker et al. 2018).

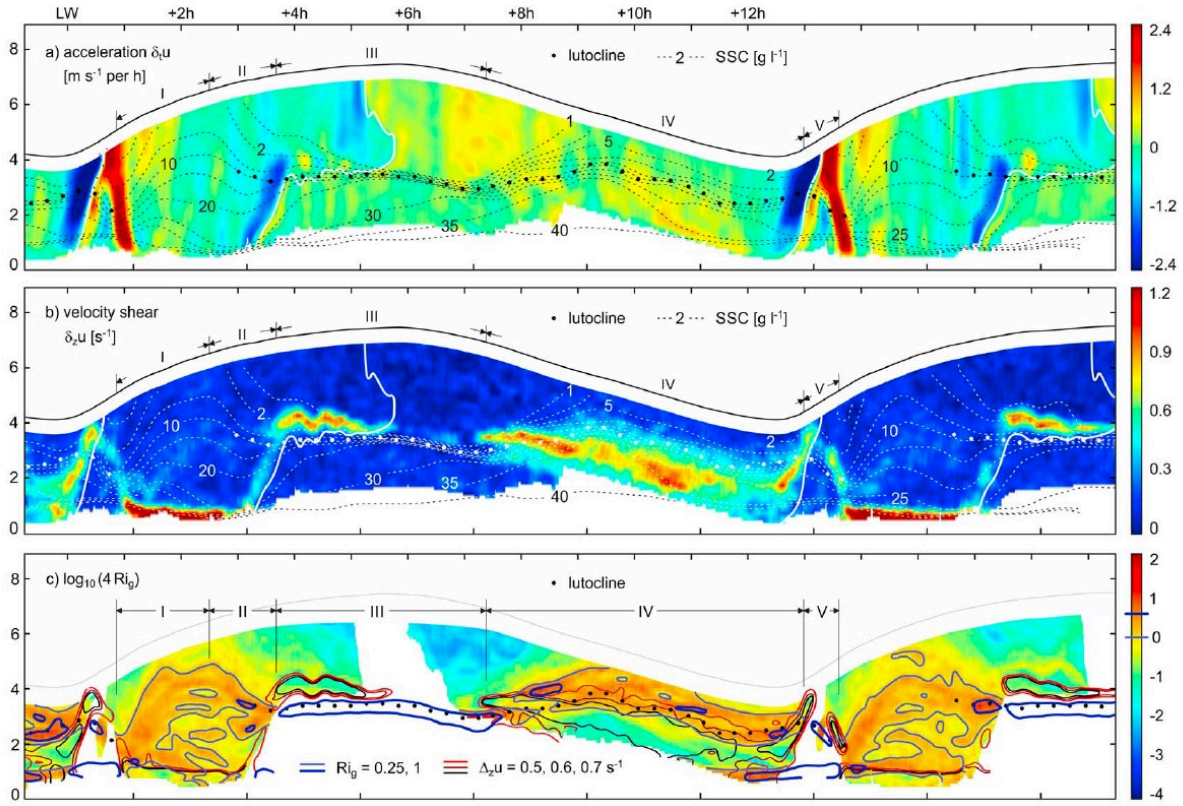

Figure 4: Dynamics and stability of a) acceleration, b) velocity shear, and c) gradient Richardson number at Jemgum in November 2014 (Becker et al. 2018).

In summary, the following main conclusions on the feedback of mud-induced periodic stratification on the flow are drawn(Becker et al. 2018):

- *"Forced by an asymmetric tide, the flow structure in a hyperturbid tidal channel is controlled by mud-induced periodic stratification,*
- *Restratification during flood leads to vertical decoupling, counter directed flow, and the development of an inverse salinity profile*
- *Intratidal transport of mud depends on the entrainment asymmetry, inducing upstream pumping during flood and shear dispersion during ebb"*

3 Experiments in laboratory flume (MudEstuary_A)

A detailed overview of existing laboratory experiments related to fluid mud which have been described in the literature is given by Chmiel (2016). Thereof, Chmiel (2016) developed the concept for the laboratory experiments within MudEstuary_A. The final results of MudEstuary_A are described in Chmiel & Malcherek (2018). In the following chapter a very brief overview of the setup and results of the laboratory experiments is given in order to be able to understand the comparison with the numerical results.

The set-up of the experiments in a 26 m long flume is shown in Figure 5. As sediment Quartz powder was chosen due to similar properties compared to mud samples of the Ems Estuary regarding density and mean grain diameter. The Quartz powder was put in an area between an inflow and outflow box. As measurement instruments ADV VectrinoProfiler (100 Hz) and Vectrino+ (200 Hz) were applied to simultaneously measure velocity, turbulence and concentration at nine positions along the flume. The inflow was varied from 40, 50, 60, 70, 80, to 90 l/s.

The experiments reproduce vertically mixed, low concentrated suspensions up to 2 g/l.
The final evaluation of the experiments revealed complex turbulent flow behavior. The vertical current velocity profiles along the measuring section of the flume show deviations from the known logarithmic profile. For certain discharges and measuring locations a linearization of the current velocity profile could be observed which could also be expected for a laminar mud flow with damped turbulence. However, if the associated turbulence and concentration profiles were analyzed, both turbulence damping and turbulence production could be observed in the flume. It showed that the flow behavior is more complex than expected. The flow is highly unsteady and not at all homogeneous in the direction of the flow. Due to the fact that for example the applied quartz powder does not contain any organic constituents the formation of a fluid mud layer could not be obtained, but rather a suspension of suspended matter that shows transient concentration curves. Furthermore, at the sediment bed in the flume both erosion and deposition could be observed which could be confirmed by the observation of ripple formation. It was assumed that such ripple structures have an additional influence on the damping and production of turbulence (Chmiel & Malcherek 2018).

The following essential findings could be derived from the experiments:

- a high resolution data set of velocity, turbulence and concentration could be measured simultaneously
- Some of the velocity profiles show a linearization over the vertical.
- It could be shown that the turbulent kinetic energy becomes zero towards the ground.
- The turbulent kinetic energy profiles describe both turbulence damping as well as increasing turbulence.

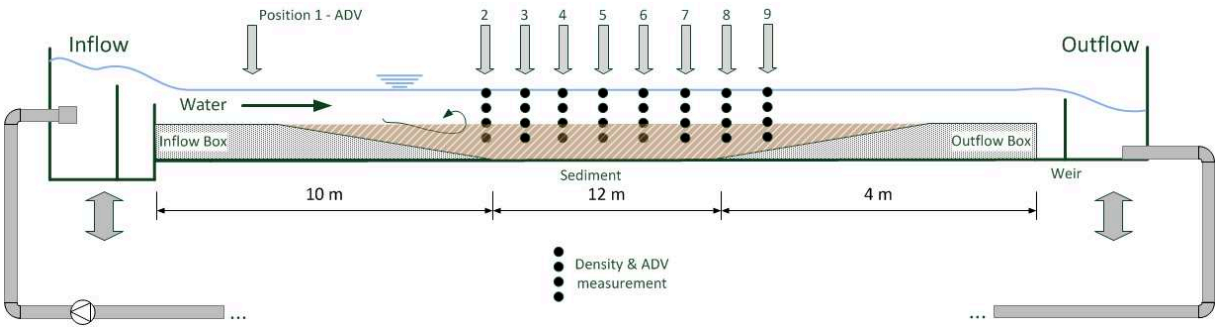

Figure 5: Set-up of laboratory flume in MudEstuary_A (Chmiel 2017).

II Extended continuous model set-up

4 General concept

In this project, we introduce an extended continuous model approach, which defines an effective viscosity $\nu = f(\nu_m, \nu_t, \nu_{rh})$ as the interaction of the molecular viscosityν_m, the turbulent viscosity ν_t and the rheological viscosity ν_{rh}. In the extended continuous model approach the rheological viscosity of an estuarine parametrization is implemented, as well as an adapted k-ω turbulence model, which can be calculated down to the immobile ground.

Thus, this model approach describes the foundation for a new holistic model understanding in the simulation of morphology in water bodies. The model simulates the water column as well as a fluid mud layer with one set of momentum, transport and turbulence model equations. The model is able to recognize automatically whether the flow is turbulent, laminar or motionless due to high concentrations of suspended matter.

The general model concept of the continuous model approach and the underlying assumptions are shown in Figure 6. In Figure 6 (a) a sketch of possible different viscosities across the water column are shown. In Figure 6 (b) a qualitative sketch of the vertical profiles of flow velocity, shear stress, turbulent kinetic energy, concentration, and effective viscosity is shown.

The assumptions of the vertical profiles of the parameters should be verified by the laboratory experiments conducted in MudEstuary_A and the appropriate methods should be implemented in a numerical model.

As mentioned before, for the numerical model the extended continuous modelling approach was at first implemented in a numerical 1DV model which was additionally developed jointly by the project partners in the first year of the project (MudEstuary_A&B). For further details and results of the 1DV model it is referred to Chmiel & Malcherek (2018). After an efficient testing of the method, this modelling approach is transferred into a three-dimensional scale.

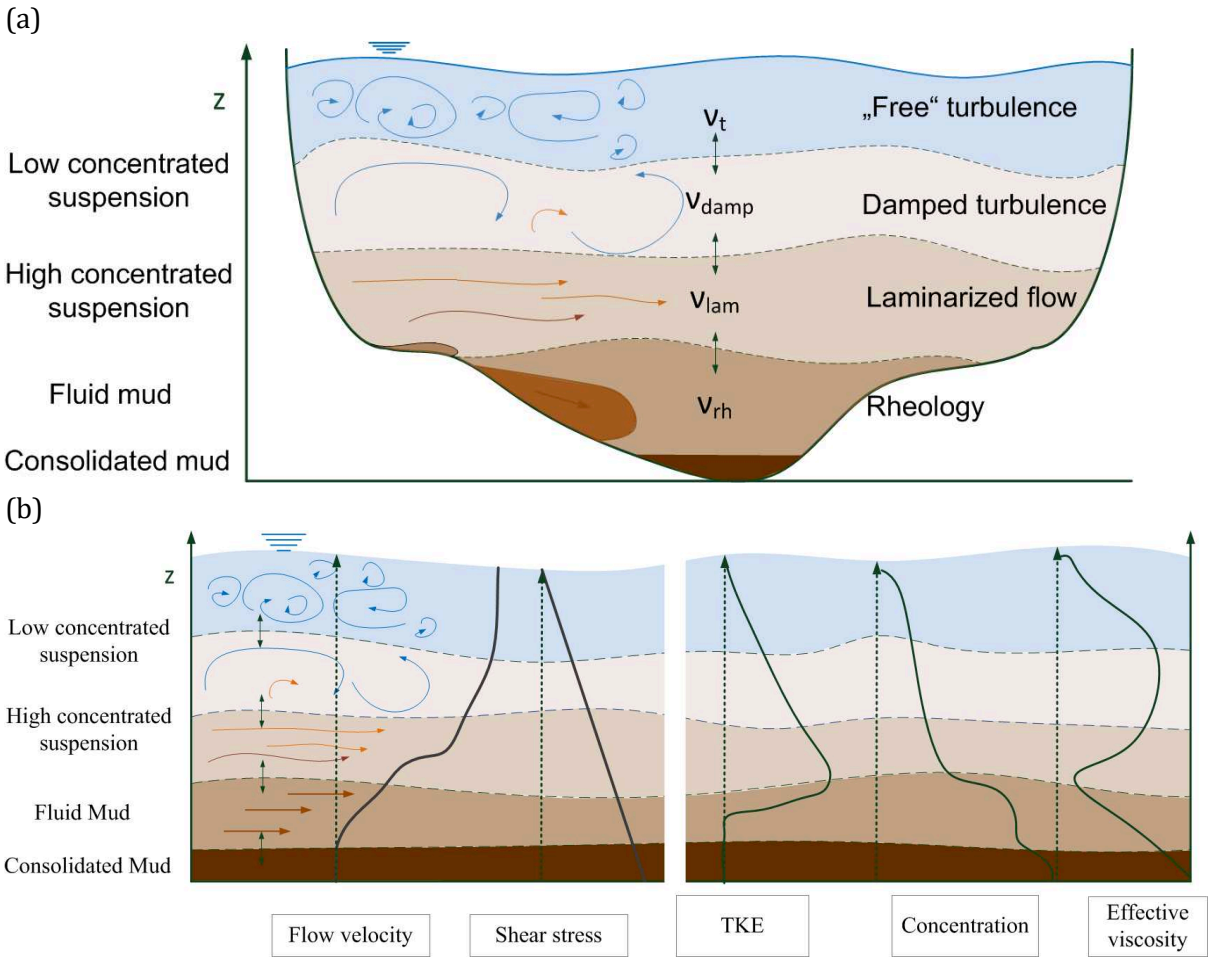

Figure 6: General model concept and assumptions (a) Viscosities across the water column; (b) Vertical profiles of flow velocity, shear stress, turbulent kinetic energy, concentration, effective viscosity (Chmiel & Malcherek, 2018)

For this study, the 3D model UnTRIM was applied and extended with an extended continuous model set-up. The numerical method UnTRIM was developed by Prof. Vincenzo Casulli (Trento University, Italy). UnTRIM is a semi-implicit finite difference (-volume) model based on the three-dimensional shallow water equations as well as on the three-dimensional transport equation for salt, heat, dissolved matter and suspended sediments. UnTRIM is able to operate on an unstructured orthogonal grid. It solves the Reynolds-averaged Navier-Stokes equations (RANS) in a Cartesian (x,y,z)-coordinate system. For detailed references of the mathematical model it is referred to Casulli & Walters (2000). Moreover, the model was further developed to describe the bathymetry on subgrid level (Casulli 2009; Casulli and Stelling 2011). For the validation document and a general introduction to UnTRIM it is referred to Casulli & Lang (2004). A summary and description of the governing equations based on Casulli & Lang (2004) is given in the appendix 11.3.

The applied version of UnTRIM is coupled to different sub-models such as the k-model for spectral waves, the sedimentological model SediMorph, and the general ocean turbulence model GOTM.

For this work, we applied the model UnTRIM and extended the model set-up by the following components which were programmed in FORTRAN:

(i) effective viscosity after eq. **(1)**
(ii) flocculation and hindered settling after eq. **(4)** and eq. **(5)**,
(iii) vertical rheological viscosity after eq. **(14)**
(iv) adapted boundary conditions for the turbulence model after eq. **(29)**

5 Mathematical description

In the following chapter a mathematical description of the components of the extended continuous model set-up is given.

5.1 Effective viscosity

The tidal dynamics under the influence of fluid mud can be described by a continuous modelling approach (Le Hir et al. 2001). Therefore, the interaction of the water column (turbulence) and fluid mud (rheology) are functions of the turbulent viscosity ν_t and rheological viscosity ν_r.

The interaction of the two viscosity components is not known. For an approximation, we assume the effective viscosity to be the sum of both parts, i.e. the turbulent eddy viscosity ν_t and the rheological viscosity ν_r.

$$\nu = \nu_t + \nu_r \qquad \textbf{(1)}$$

ν_t	m^2/s	turbulent viscosity
ν_r	m^2/s	rheological viscosity

The turbulent viscosity has to become zero in a resting mud bottom on the one hand, and on the other hand, the rheological viscosity has to vanish if no suspended matter is present. It has to be mentioned that both viscosities have different physical meanings. As an increase of turbulent viscosity is interpreted as an increase of turbulence, the rheological viscosity is the opposite. An increase of rheological viscosity goes with an increase of the solid content and therefore with a decrease of turbulence. In a resting sediment bottom the turbulent kinetic energy is zero and therefore the turbulent viscosity also vanishes. On the other hand in a clear water column the rheological viscosity transforms into the molecular viscosity of water.

Moreover, in order to simulate fluid mud dynamics, Le Hir et al. (2001) identify as most important processes in order of importance:
(i) turbulence damping
(ii) hindered settling and
(iii) viscoplastic behavior of mud.

These processes and their mathematical descriptions as well as the chosen method for the implementation are defined and described in the following sections.

5.2 Hindered settling

As defined in Whitehouse et al. (2000), hindered settling is the process by which a high concentration of settling flocs interferes with the surrounding flow of fluid (displaced water, collisions, group settling, etc.). It usually commences at suspended sediment concentrations between 2 kg/m^3 to 10 kg/m^3.

Due to interactions with neighboring particles, the effective settling velocity is reduced relative to the settling velocity of an individual particle as shown in eq. **(2)**. The effective (hindered) settling velocity is usually expressed by an empirical correction as a function of the effective volumetric concentration.

$$h_s = \frac{w_s}{w_{s,0}} \quad \textbf{(2)}$$

h_s	-	relative settling velocity
w_s	[mm/s]	effective settling velocity (hindered)
$w_{s,0}$	[mm/s]	settling velocity of individual particle (unhindered)

The effective settling velocity has been determined, among others, by the following authors:

5.2.1 Richardson and Zaki (1954)

A first power law equation is described by Richardson and Zaki (1954). The equation is also implemented in Delft3D (Deltares 2014) and applied for the Ems estuary e.g. by van Maren et al. (2015b):

$$w_s = w_{s,0}\left(1 - \frac{c}{c_{ref}}\right)^5 \quad \textbf{(3)}$$

w_s	[mm/s]	effective settling velocity (hindered)
$w_{s,0}$	[mm/s]	settling velocity of individual particle (unhindered)
c	[kg/m^3]	suspended sediment concentration
c_{ref}	[kg/m^3]	reference concentration

The reference concentration is sometimes defined as the concentration of the immobile sediment bed, i.e. 1600 kg/m^3, which is the default value considered in Delft3D. However, the reference concentration can also be assumed to represent the gelling concentration of fluid mud. As stated in van Maren et al. (2015b), in this case c_{ref} is the gelling concentration c_{gel} with typical values of 100 kg/m^3 for clay-dominated suspensions.

5.2.2 van Rijn (1993)

In van Rijn (1993) the following equations for flocculation and hindered settling are given:

$w_{s,m} = k \cdot c^m$ (flocculation for 0.1 < c <= 10 g/l) **(4)**

$w_{s,m} = w_s \cdot (1 - \alpha\, c)^{\beta}$ (hindered settling for c > 10 g/l **(5)**

$w_{s,m}$	[mm/s]	settling velocity of flocs in fluid-sediment mixture
w_s	[mm/s]	settling velocity of individual particles (unhindered)
c	[-]	volumetric concentration
m	[-]	coefficient (= 1 to 2)
k	[-]	coefficient
α	[-]	coefficient
β	[-]	coefficient (= 3 to 5)

The equations were applied for modelling the Ems Estuary by FTZ (2016). Therefore the following parameters were chosen:
$k = 0.513; m = 1.29; w_S = 13.48;\ \alpha = 0.008;\ \beta = 3.43$
The associated settling velocities reach max. values of 10 mm/s. The concentration dependent settling velocities are shown in Figure 7.

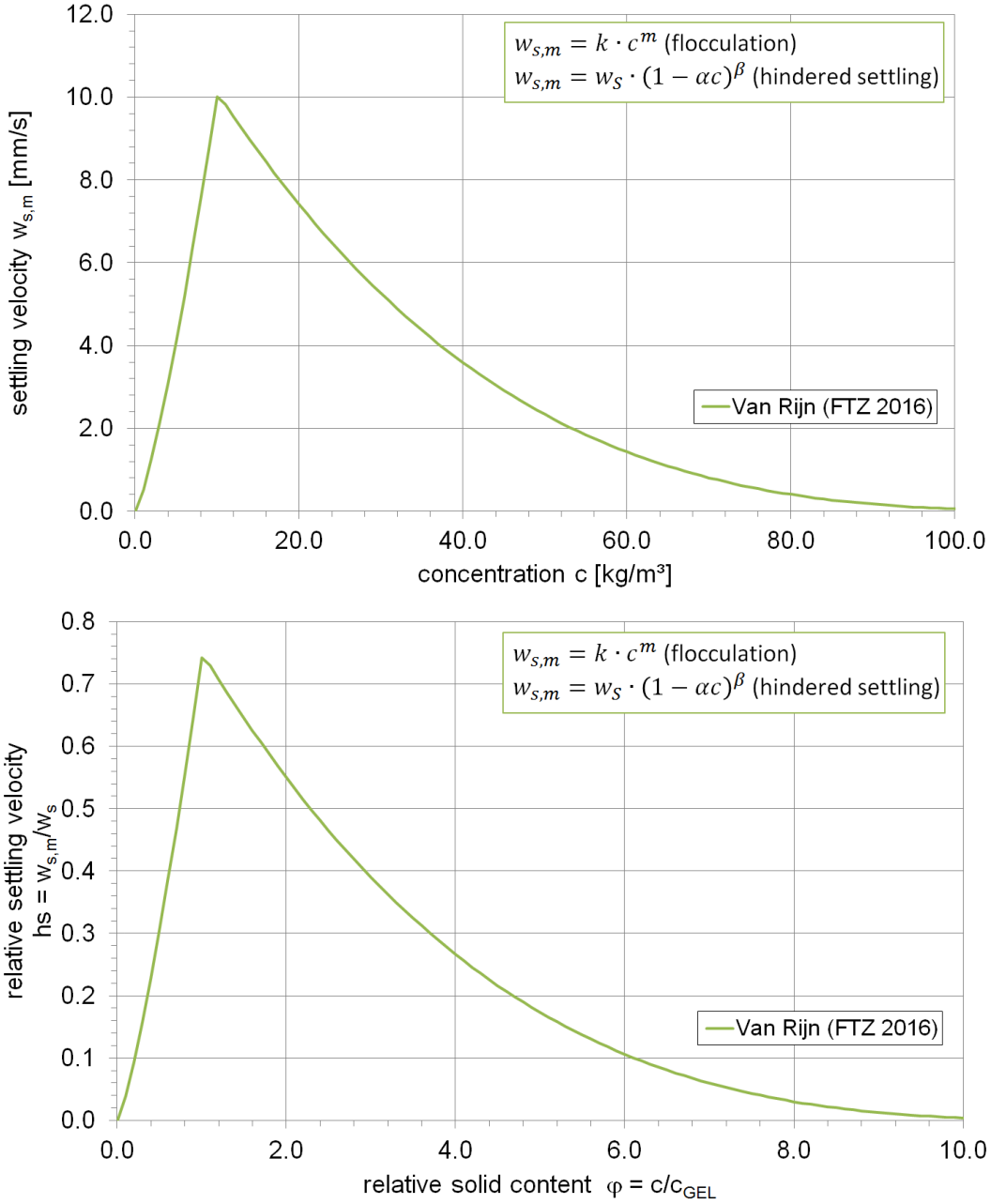

Figure 7: Flocculation and hindered settling by van Rijn (1993) using parameters for Ems Estuary after FTZ (2016); top: absolute; bottom: relative values.

5.2.4 van Rijn, Leo C. (2007)

In van Rijn, Leo C. (2007) the equations are given as

$$w_s = w_{s,0}(1-c)^5 \quad (7)$$

$$w_s = w_{s,0}\left(1 - 0.65\, c/c_{gel}\right)^5 \quad (8)$$

w_s	[mm/s]	effective settling velocity (hindered)
$w_{s,0}$	[mm/s]	settling velocity of individual particle (unhindered)
c	[-]	volume suspended sediment concentration
c_{gel}	[-]	volume gelling concentration

Furthermore, it is stated that experimental data with fine sediments can be represented by the equation $w_s = w_{s,0}\left(1 - 0.65\, c/c_{gel}\right)^n$ with an exponent n in the range of 5-6 or by the expression of $w_s = w_{s,0}\left(1 - c/c_{gel}\right)^{3.5}$.

5.2.5 Winterwerp (2002)

Winterwerp (2002) developed the following equation for hindered settling:

$$w_s = w_{s,0}\frac{(1-\phi_*)^n\left(1-\phi_p\right)}{(1+2.5\,\phi)} \quad (9)$$

w_s	[mm/s]	effective settling velocity (hindered)
$w_{s,0}$	[mm/s]	settling velocity of individual particle (unhindered)
ϕ_*	[-]	volumetric concentration $\phi_* = \min\{1, \phi\}$ (to account for the fact that $c=c_{gel}$ can exceed unity in a consolidating fluid mud layer)
ϕ_p	[-]	volumetric concentration of primary particles $\phi_P = c/\rho_S$
ϕ	[-]	volumetric concentration of mud flocs $\phi = c/c_{gel}$
c	[kg/m³]	mass concentration
c_{gel}	[kg/m³]	gelling concentration
ρ_S	[kg/m³]	density of the sediment
n	[-]	exponent (n=1 in Winterwerp (2002); n=4 Wehr (2012))

An earlier application to the Ems Estuary was performed by Winterwerp (1999) with gelling concentration of 40 g/l and constant settling velocity of w_s = 0.6 mm/s. Furthermore, the hindered settling approach with an exponent of n=4 (instead of n=1) was applied for the Ems estuary by Wehr (2012). The relative settling velocity by Winterwerp (2002) for two different exponents (n=1 in Winterwerp (2002); (n=4 Wehr (2012)) is shown in Figure 8.

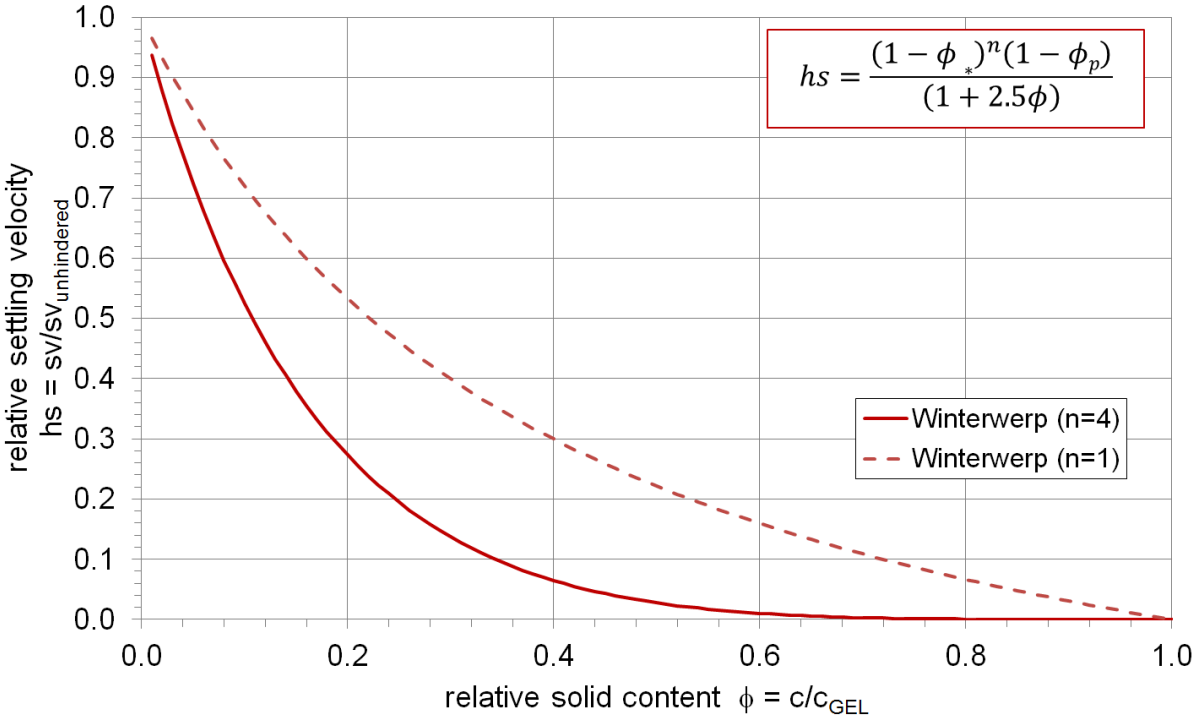

Figure 8: Hindered settling by Winterwerp (2002).

5.2.6 Malcherek (2017)

A hindered settling approach developed by Malcherek (2017) is defined as follows:

$$w_s = \frac{1}{2} w_{s,0} \left(1 - tanh\left(\gamma_1 \left(\frac{c}{c_{50}} - 1 \right) \right) \right) \qquad \textbf{(10)}$$

The associated relative settling velocities are shown in Figure 9 and with a variation of the shape factor in Figure 10.

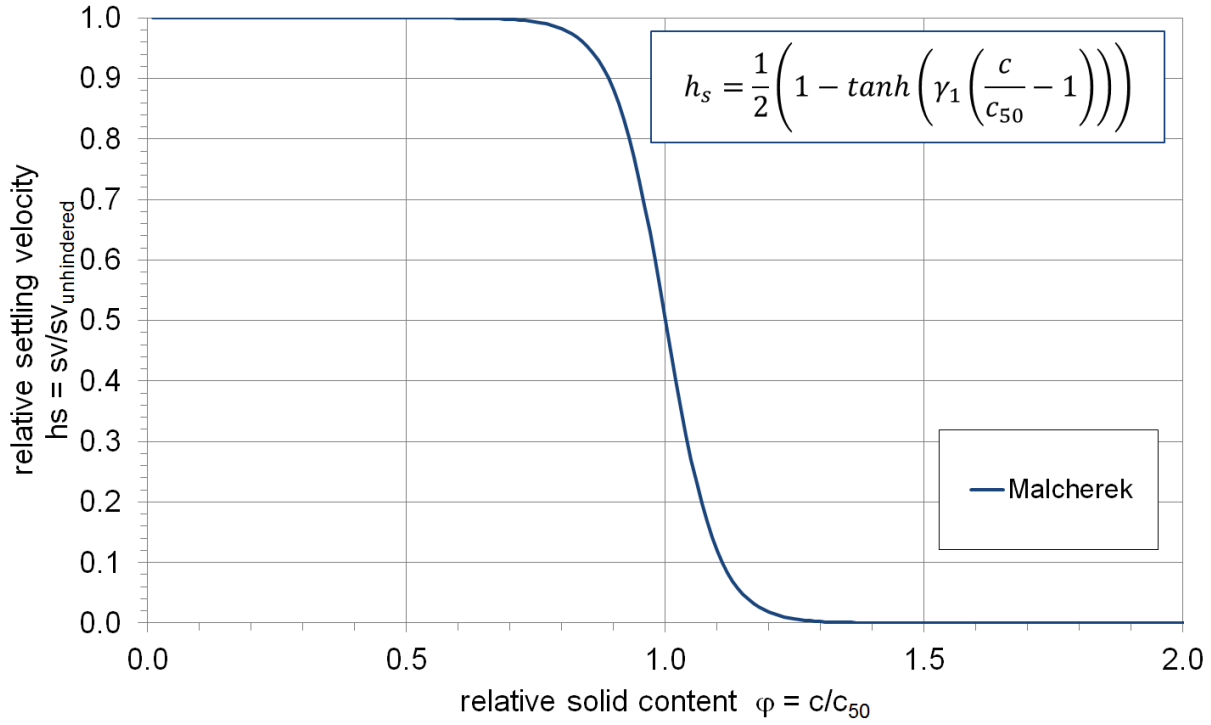

Figure 9: Hindered settling by Malcherek (2017) with shape factor gamma1=10.

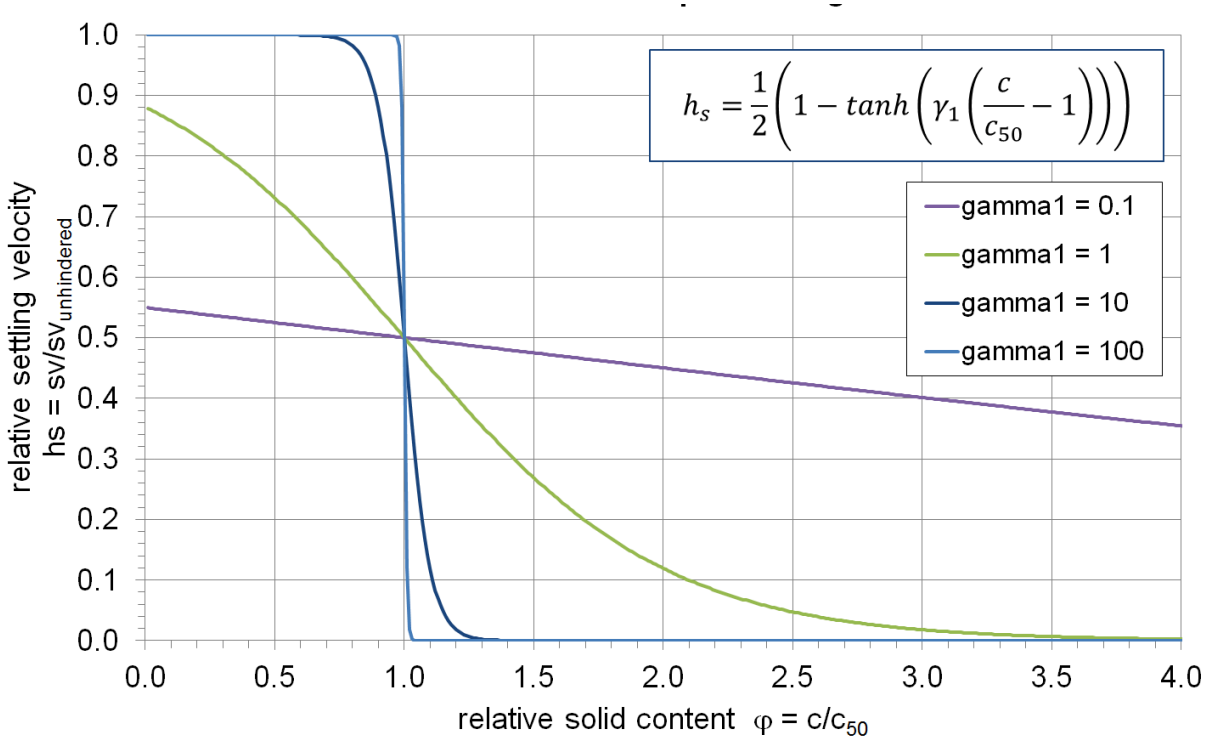

Figure 10: Hindered settling by Malcherek (2017) with variation of shape factor (gamma1 = 0.1; 1; 10; 100).

5.2.7 Model enhancement

All approaches for hindered settling describe the reduction of the settling velocity as a function of the concentration. Hence, all equations are in general comparable. The description of hindered settling is dependent on the choice of the maximum and minimum settling velocity as well as the selection of a critical concentration, e.g. gelling concentration. For this project the hindered settling velocity defined by van Rijn (1993) was implemented in a FORTRAN module and applied for the numerical simulations. The choice for a settling velocity defined by van Rijn (1993) was made because the approach was used in a recent study for the Ems estuary (FTZ 2016) and thus allows comparability.

5.3 Rheological viscosity

The non-Newtonian behavior of fluid mud can be approximated by

- the most important internal stress components of the momentum equation (see appendix 11.1.2), and
- the rheological viscosity with the most important components of the deformation rate tensor (see appendix 11.2).

With these approximations, the general solution algorithm of conventional hydrodynamic models using Navier-Stokes equations is still applicable.

A parametrization of different rheological models for estuarine mud suspensions was developed by Malcherek and Cha (2011). The authors performed rheological analyses of ten samples of fluid mud of Weser estuary and Ems estuary. The parametrizations were developed for a Bingham model and a Worrall-Tuliani model which are defined in the following sections.

5.3.1 Bingham model

A parameterization of the **Bingham model** is defined as:

$$\mu_r = \frac{\tau_y}{\sqrt{\left|\left(\frac{\partial u}{\partial z}\right)^2 + \left(\frac{\partial v}{\partial z}\right)^2\right|}} + 2\mu_B = \frac{6980\ Pa\ \Phi_S^4}{\sqrt{\left|\left(\frac{\partial u}{\partial z}\right)^2 + \left(\frac{\partial v}{\partial z}\right)^2\right|}} + 2 \cdot 1.8 \cdot 10^{-3} Pa\ s\ \cdot \exp(15.39\Phi_S) \qquad \textbf{(11)}$$

Hence, the dynamic rheological viscosity of the Bingham model is:

$$\nu_r = \frac{6980\ Pa\ \Phi_S^4}{\rho_B \sqrt{\left|\left(\frac{\partial u}{\partial z}\right)^2 + \left(\frac{\partial v}{\partial z}\right)^2\right|}} + \frac{2 \cdot 1.8 \cdot 10^{-3} Pa\ s\ \cdot \exp(15.39\Phi_S)}{\rho_B} \qquad \textbf{(12)}$$

5.3.2 Worrall-Tuliani model

A parameterization of the **Worrall-Tuliani model** is given in Knoch and Malcherek (2011):

$$\mu_r = \frac{7021 Pa \phi_s^{4.245}}{\dot{\gamma}} + \mu_0 exp(14.69\phi_s) + \frac{0.8358 Pa \cdot \mathrm{s}\, \phi_s}{0.02193\, s\, {\phi_s}^{-0.5808}\, \dot{\gamma} + 1} \qquad \textbf{(13)}$$

Considering the approximation of $|II_D|$ and the dynamic viscosity, the dynamic rheological viscosity of the Worrall-Tuliani model results in:

$$\nu_r = \frac{7021 Pa \phi_s^{4.245}}{\rho_B \sqrt{\left|\left(\frac{\partial u}{\partial z}\right)^2 + \left(\frac{\partial v}{\partial z}\right)^2\right|}} + \frac{\mu_0 exp(14.69\phi_s)}{\rho_B} + \ldots$$

$$\ldots \frac{0.8358 Pa \cdot s\, \phi_s}{\rho_B \left(0.02193\, s\, {\phi_s}^{-0.5808} \sqrt{\left|\left(\frac{\partial u}{\partial z}\right)^2 + \left(\frac{\partial v}{\partial z}\right)^2\right|} + 1\right)} \qquad \textbf{(14)}$$

The results of the rheological viscosity of the estuarine parametrization by Knoch and Malcherek (2011) is visualized for different densities in Figure 11.

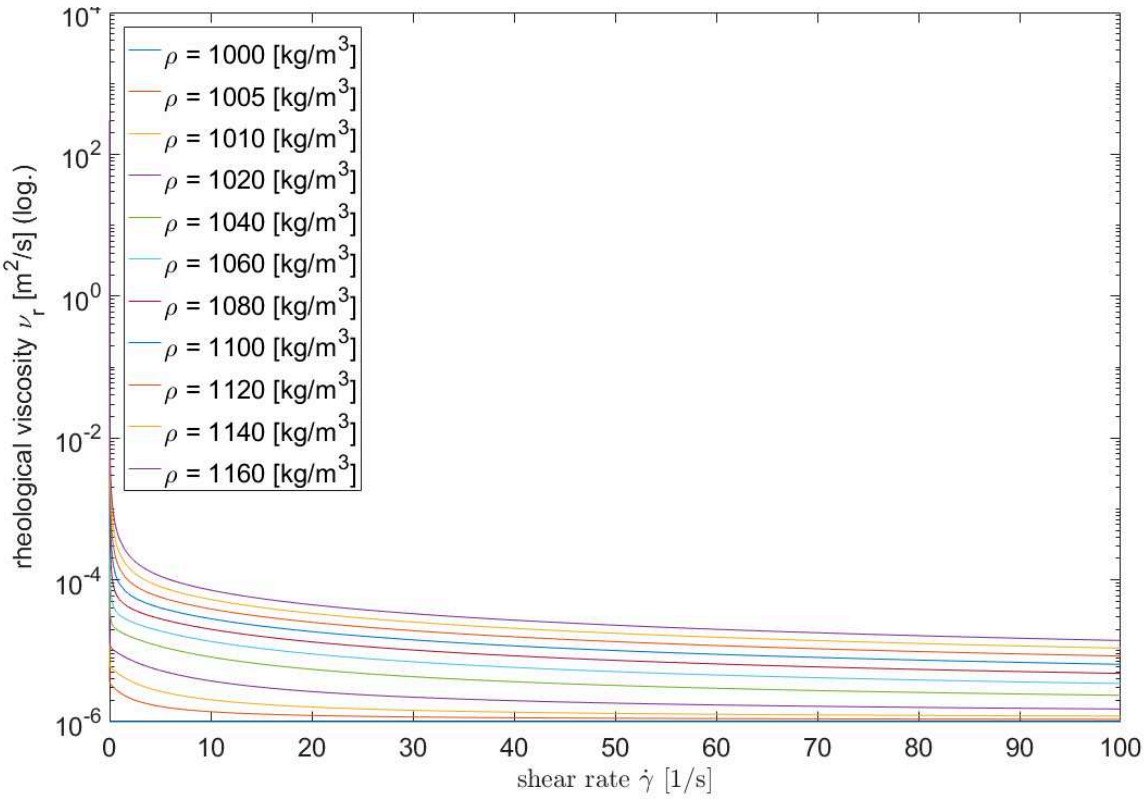

Figure 11: Rheological viscosity of the Worrall-Tuliani model by Knoch and Malcherek (2011).

5.3.3 Model enhancement

The rheological viscosity of the estuarine parametrization by Knoch and Malcherek (2011) was implemented in a FORTRAN module and applied for the numerical simulations. The selection for this parametrization was also made to allow comparability with the results determined by the fluid mud model by Wehr (2012). Moreover, a variation of the parameters of the rheological viscosity was performed which is described in section 6.2.2.3.

5.4 Turbulence

5.4.1 General concept

In general, Reynolds averaged Navier-Stokes (RANS) are often applied for large scale applications such as in coastal engineering (order of km). By averaging the Navier-Stokes equations, the RANS equations are derived. Hence, the mean flow parameters are determined. However, the velocity fluctuations still appear in the RANS equations due to the nonlinearity of the Navier–Stokes equations. The averaging of the advective terms of the momentum equations results in the nonlinear term $-\rho\overline{(u_i' u_j')}$ which is called Reynolds stress term. As a consequence, the system of RANS equations includes more unknowns as equations. This problem is called closure problem. In order to close the system of equations, the Reynolds stress term has to be described by further turbulence models.

Therefore, two-equation models such as the k-ε-model are commonly used. Models involving the partial differential equation (pde) for the mean velocity field and two pde's relating to the turbulence velocity scale and to a turbulence length scale are:

- Two pde for μ_t, e.g. k-ε-model with k=TKE and ε= dissipation of TKE $\mu_t = c_\mu \rho \frac{k^2}{\epsilon}$
- Further alternatives, first pde mostly with k and second pde with $k^m L^n$, e.g. $\varepsilon = k^{3/2} L^{-1}$, $\omega = k^{1/2} L^{-1}$, $L = k^0 L^1$,

The models are simple but sufficient enough and therefore widely applied for modelling natural waters. For most situations, it is a good compromise in terms of accuracy and cost-effectiveness. A library of traditional and state-of-the-art turbulence closure models for natural waters is provided by the General Ocean Turbulence Model (GOTM) (Umlauf and Burchard 2005).

5.4.2 k-ε-turbulence model

The k-ε-turbulence model was described by Launder and Spalding (1974) and further developed by e.g. Rodi (1987).

5.4.2.1 Mathematical description

turbulent kinetic energy

$$\frac{\partial k}{\partial t} + u_j \frac{\partial k}{\partial x_j} = \frac{\partial}{\partial x_j}\left(\left(\nu + \frac{\nu_t}{\sigma_k}\right)\frac{\partial k}{\partial x_j}\right) + P_k + G - \varepsilon \qquad \textbf{(15)}$$

dissipation

$$\frac{\partial \varepsilon}{\partial t} + u_j \frac{\partial \varepsilon}{\partial x_j} = \frac{\partial}{\partial z}\left(\left(\nu + \frac{\nu_t}{\sigma_\varepsilon}\right)\frac{\partial \varepsilon}{\partial z}\right) + \frac{\varepsilon}{k}(C_{1\varepsilon}P_k - C_{2\varepsilon}\varepsilon) \qquad \textbf{(16)}$$

production

$$P_k = \nu_t\left(\frac{\partial u_i}{\partial x_j} + \frac{\partial u_j}{\partial x_i}\right)\frac{\partial u_i}{\partial x_j} \qquad \textbf{(17)}$$

turbulent viscosity

$$\nu_t = c_\mu \frac{k^2}{\varepsilon} \qquad \textbf{(18)}$$

buoyancy term G

$$G = \frac{g}{\rho}\frac{\upsilon_t}{\sigma_s}\frac{\partial \rho}{\partial z} \qquad \textbf{(19)}$$

G describes the destruction of turbulence due to stratification. Stratification is described by gradients of the bulk density of the suspension.
Temperature-induced stratification was analyzed by Viollet (1988).

k	[m^2/s^2]	turbulent kinetic energy
P_k	[m^2/s^3]	turbulence production
ε	[m^2/s^3]	turbulence dissipation
σ_k	[-]	Prandtl-number ($\sigma_k = 1.0$)
c_D	[-]	empiric constant ($c_D = 0.001$)
c_μ/c'_μ	[-]	proportional constant for eddy viscosity ($c'_\mu = 0.09$)
$C_{1\varepsilon}$	[-]	constant for standard k-ε-model ($C_{1\varepsilon} = 1.44$)
$C_{2\varepsilon}$	[-]	constant for standard k-ε-model ($C_{2\varepsilon} = 1.92$)
σ_ε	[-]	constant for standard k-ε-model ($\sigma_\varepsilon = 1.0$)

boundary conditions

- Surface: $\frac{\partial k}{\partial z} = 0$; $\varepsilon = \frac{\left(\sqrt{c_\mu}\,k\right)^{3/2}}{\kappa 0{,}07h} = \frac{(k)^{3/2}}{0{,}18h}$
- Bottom: $k = \frac{u_*^2}{\sqrt{c_\mu}}$; $\varepsilon = \frac{u_*^3}{\kappa z_{0B}}$ **(20)**

  (z_{0b}=0.2;integration limit at bottom = $k_{surface}/30 \sim d_m/10$)

Viscous boundary layer is described by wall functions.

5.4.2.2 Adaptation to fluid mud

Sediment-induced stratification was analyzed by Toorman et al. (2002).
Toorman et al. (2002) suggested an adaptation of the turbulent Schmidt-number:

$$\sigma_s = \sigma_s(1 + \alpha Ri)^{\beta} \qquad \textbf{(21)}$$

Furthermore, a modification of the boundary conditions at the bottom was introduced (Toorman 2000; Toorman et al. 2002):

$$k = \frac{u_*^2}{\sqrt{c_\mu}}(1 - z_{0B}/h)\sqrt{1 - Rf_0} \quad ; \qquad \varepsilon = \frac{u_*^3}{\kappa z_{0B}}(1 - z_{0B}/h)(1 - Rf_0) \qquad \textbf{(22)}$$

One disadvantage of the k-ε-model is that it is only valid for fully turbulent flow and non-separated flows. The application of wall functions for the viscous boundary layer leads to poor results in this area. Moreover, within the viscous sublayer the condition k = 0 has to be full filled, which can produce numerical instabilities in the ε -equation. Hence, an application for fluid mud seems to be inappropriate.

5.4.3 k-ω-turbulence model

The k-ω-turbulence model was refined and improved by Wilcox (1993).

5.4.3.1 Mathematical description

turbulent kinetic energy

$$\frac{\partial k}{\partial t} + u_j \frac{\partial k}{\partial x_j} = \frac{\partial}{\partial x_j}\left(\left(\nu + \frac{\nu_t}{\sigma_k}\right)\frac{\partial k}{\partial x_j}\right) + P_k + G - \beta^* k\omega \qquad \textbf{(23)}$$

dissipation

$$\frac{\partial \omega}{\partial t} + u_j \frac{\partial \omega}{\partial x_j} = \frac{\partial}{\partial z}\left(\left(\nu + \frac{\nu_t}{\sigma_\omega}\right)\frac{\partial \omega}{\partial z}\right) + \alpha \frac{\omega}{k} P_k - \beta\omega^2 \qquad \textbf{(24)}$$

production

$$P_k = \nu_t \left(\frac{\partial u_i}{\partial x_j} + \frac{\partial u_j}{\partial x_i}\right)\frac{\partial u_i}{\partial x_j} \qquad \textbf{(25)}$$

turbulent viscosity

$$\nu_t = \frac{k}{\omega} \qquad \textbf{(26)}$$

buoyancy term G

$$G = \frac{g}{\rho}\frac{\nu_t}{\sigma_s}\frac{\partial \rho}{\partial z} \qquad \textbf{(27)}$$

G describes the destruction of turbulence due to stratification. Stratification is described by gradients of the bulk density of the suspension.

Temperature-induced stratification was analyzed by Viollet (1988).

k	[m^2/s^2]	turbulent kinetic energy
P_k	[m^2/s^3]	turbulence production
ω	[m^2/s^3]	turbulence dissipation
σ_k	[-]	Prandtl-number ($\sigma_k = 2.0$)
α	[-]	constant for standard k-ω-model ($\alpha = 5/9$)
β*	[-]	constant for standard k-ω-model ($\beta^* = 9/100$)
β	[-]	constant for standard k-ω -model ($\beta = 3/40$)
σ_ω	[-]	constant for standard k-ω-model ($\sigma_\omega = 2.0$)

boundary conditions
If the viscous boundary layer at the bottom is not modelled, the following boundary conditions can be applied:

- Surface: $\frac{\partial k}{\partial z} = 0;$ $\omega = \alpha \frac{\sqrt{k_s}}{h}$
  Bottom: $k = \frac{u_*^2}{\sqrt{\beta^*}};$ $\omega = \frac{u_*}{\sqrt{\beta^*}\kappa z_{0B}}$ **(28)**
  (z_{0b}=0.2;;integration limit at bottom = $k_{surface}/30 \sim d_m/10$)

One advantage of the k-ω-model is that the viscous sublayer can be modelled without wall functions. One disadvantage of the k-ω-model is that boundary layer computations are very sensitive to the values of in the free stream.

5.4.3.2 Adaptation to fluid mud

In contrast to the k-ε-turbulence model, for instance, the k-ω-turbulence model is applicable for low-Reynolds flows and for modeling the viscous sublayer without introducing additional damping functions. Within the viscous sublayer the condition k = 0 has to be full filled, which does not produce numerical instabilities in the ω-equation. The transport equation for ω can be rewritten by simple mathematical substitution. With that form it is evident that the ω-equation is being decoupled of the k-equation. Therefore the k-ω model is able to provide a stable solution for laminar flow, even when the turbulent kinetic energy is zero.

However, the steep gradients require a fine resolution.

The boundary conditions at the bottom as originally defined by Wilcox (1993):

$$k = 0$$
$$\omega = S_r \frac{u_*^2}{\nu} \text{ mit } S_r = \begin{cases} \left(\frac{50}{k_s^+}\right)^2, k_s^+ < 25 \\ \frac{100}{k_s^+}, k_s^+ > 25 \end{cases} \quad \textbf{(29)}$$

With dimensionless sand roughness $k_s^+ = \frac{u_* k_s}{\nu}$

The advantage of the k-ω-turbulence model is the ability to consider the Stokes' wall condition ($u_b = 0$, $k_b = 0$) in the bottom boundary conditions for ω. Doing so, the k-ω-model is able to resolve the viscous layer near the immobile bed. In case of an immobile bed, i.e. no shear rate and no turbulence production at the bed, ω will be constant and equal to its lower boundary value ω_b.

Hence, the k-ω-model is capable to reproduce the transient behavior from laminar to turbulent flows. Here the turbulent kinetic energy is zero and therefore ν_t is zero. In this case the viscosity reduces to its laminar value. There remains the question what is ω in that case. Since the introduction of the k-ω-model there is a discussion, what ω really represents. Because it has a finite value at closed boundaries where the turbulent kinetic energy is zero, it cannot be interpreted as a dissipation rate. Within this modeling concept ω is rather the potential of a dissipation rate. It describes the ability of turbulence destruction due to the solid content and not the actually destroyed turbulent energy.

5.4.4 Model enhancement

In contrast to the k-ε-turbulence model, the k-ω-model is capable to reproduce the transient behavior from laminar to turbulent flows. Therefore, the adapted boundary conditions are implemented in an existing FORTRAN module of the k-ω-model.

The disadvantage of the k-ω-model of the free-stream sensitivity is neglected at this stage. After the k-ω-model is successfully applied in fluid mud, the problem can be solved later, e.g. by k-ω-SST-model. Menter (1994) developed with the k-ω-SST-model a zonal model which combines the k-ω and k-ε by a blending function where k-ω is used at the wall and k- ε at the outer part. Furthermore, another alternative would be the new k-ω model developed by Wilcox (2008).

6 Numerical simulations

This chapter summarizes the set-up of the numerical model of the laboratory flume (section 6.1) and the schematic estuary (section 6.2).

The original work plan comprised the set-up of numerical models in order of increased complexity

1. Laboratory flume (channel with steady flow)
2. Schematic estuary (channel with constant width, variation in depth, unsteady flow)
3. Ems Estuary (complex bathymetry and unsteady flow)

The methods and results for the laboratory flume and the tidal channel will be given in the following sections. However, for an application to the real Ems Estuary further research and validation data are needed. The reasons and future prospects will also be discussed at the end of this

chapter. For an application to the Ems Estuary by a classic hydrodynamic model it is referred to part III of this report.

6.1 Laboratory flume

6.1.1 Method

6.1.1.1 Grid

The grid for the numerical model of the laboratory flume is 26 m long and 0.99 m wide (see Figure 12). The horizontal and lateral resolution is approximately 0.12 m; the vertical resolution is 0.01 m. At z = 0.0 m there is a rigid layer. Furthermore, the grid includes an inflow and outflow box at z = 0.15 m. The base inclination is 0.001 %. At the side boundaries free slip is defined.

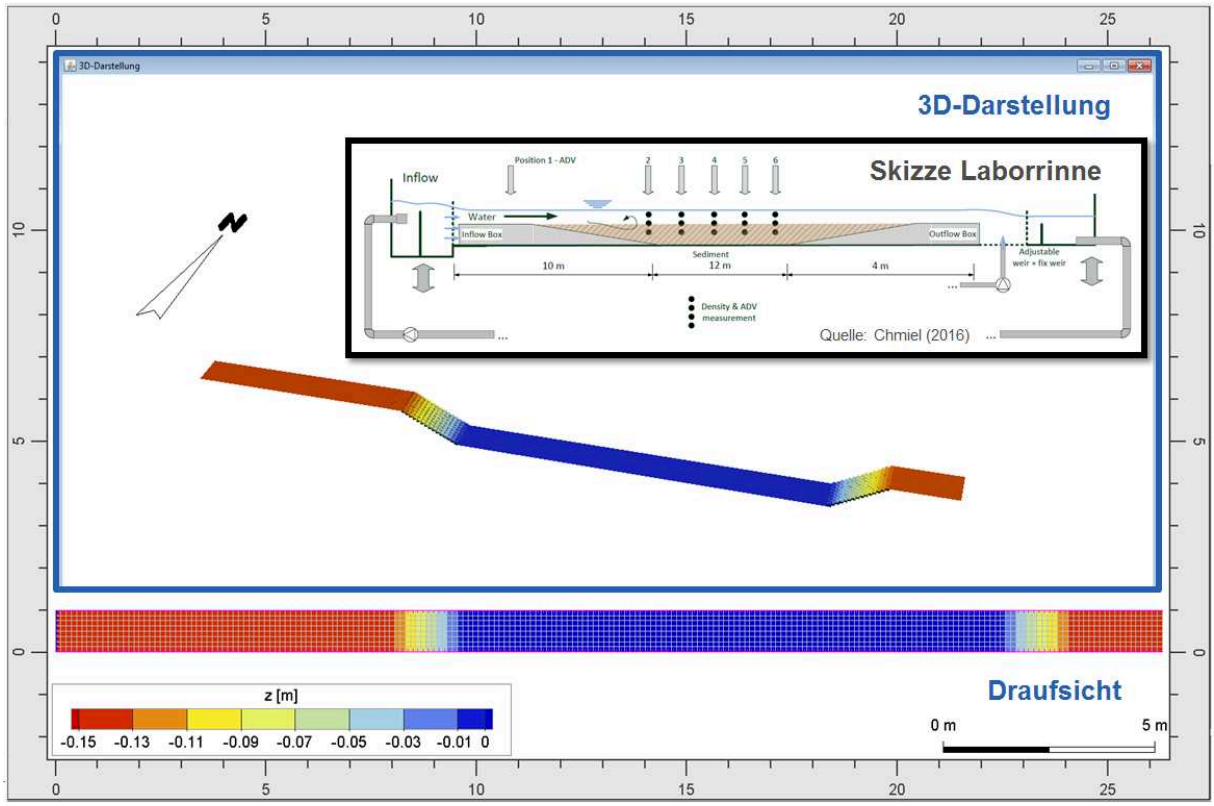

Figure 12: Grid of the laboratory flume.

6.1.1.2 Boundary values

The open water level boundary at the outflow section is set to a constant water level of z=0.35 m (0,20 m above boxes). The inflow area is a flow section with different flow scenarios of 40, 50, 60, 70, 80, and 90 l/s. The flow is linearly increased over a period of 1h.

6.1.1.3 Initial value

The initial water level is set to z = 0.35 m and the initial velocities are set to zero.

6.1.1.4 Further settings

Further setting parameters are summarized in Table 1. The simulation time is 2h. Within the first hour the flow section is defined with a linear increase of inflow and after 2 hours a steady state is reached.

Table 1: Model parameters for Laboratory Flume.

Model parameter	**Variable**	**Value**
Length, width, depth	L, B, depth	26 m, 0.99 m, 0.20 m
Discretization	dx, dy, dz	0.12 m, 0.12 m, 0.01 m
Time step	Dt	2 sec
Sediment: Mean grain diameter of Quartz powder	d_m	18 µm (18.0E-06 m)
Settling velocity	w_s	Stokes
Bottom roughness	z_{ob}	nikuradse_ks
Erosion begin		Shields

6.1.2 Results

The results of the extended continuous modelling set-up are exemplarity shown in Figure 13. The current velocity (left), suspended sediment concentration (middle) and turbulent kinetic energy (right) are shown for the extended continuous model set-up in red as well as the classic model set-up in blue. By applying the extended continuous model set-up, the model is now able to simulate the decrease of turbulent kinetic energy at the bottom of the laboratory flume. The shape of the curve of the kinetic energy corresponds well to the assumed vertical profile of the turbulent kinetic energy of the general concept (see Figure 6). However, a very high vertical resolution of 0.01 m is required.

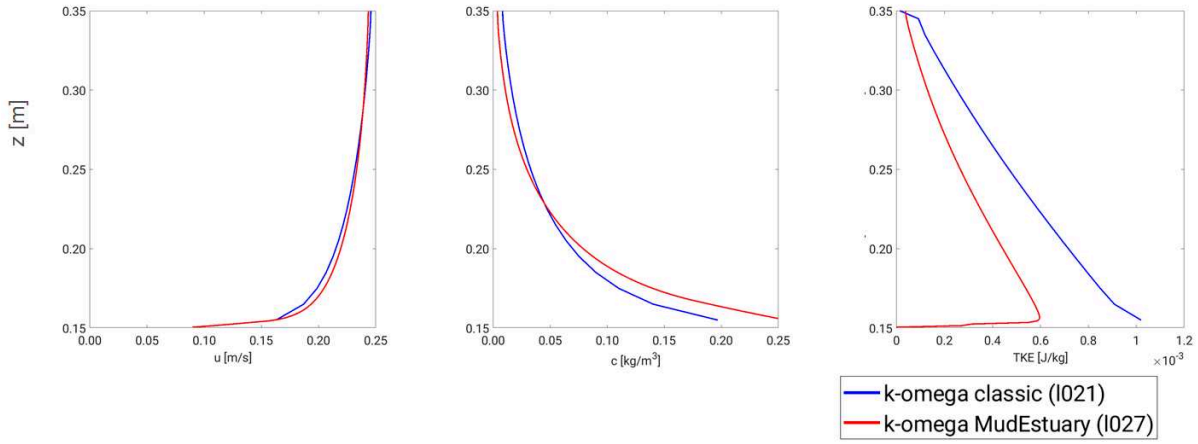

Figure 13: Results of extended continuous model set-up (red) and classic model set-up (blue) for current velocity (left), SSC (middle) and TKE (right).

The results of the numerical simulations are compared to the results of the laboratory experiments. As described in chapter 3, the final evaluation of the experiments revealed complex turbulent flow behavior. The vertical current velocity profiles along the measuring section of the flume show deviations from the known log profile. For certain discharges and measuring locations a linearization of the current velocity profile could be observed which could also be expected for a laminar mud flow with damped turbulence. However, if the associated turbulence and concentration profiles were analyzed, both turbulence damping and turbulence production could be observed in the flume. It showed that the flow behavior is more complex than expected. The flow is highly unsteady and not at all homogeneous in the direction of the flow. Due to the fact that the applied quartz pow-der does for example not contain any organic constituents the formation of a fluid mud layer could not be obtained, but rather a suspension of suspended matter that shows transient concentration curves. Furthermore, at the sediment bed in the flume both erosion and deposition could be observed which could have an additional influence on the damping and production of turbulence (Chmiel & Malcherek 2018).

Hence, a comprehensive comparison between experiments and numerical simulations cannot be made.

However, exemplary results of a comparison between experiment (dots) and numerical simulation (red) are presented in this section. For a discharge of 90 l/s (Q90P), the flow velocities, concentrations and turbulent kinetic energy at nine measurement stations (M1 – M9) along the laboratory flume are shown in Figure 14, Figure 15, and Figure 16. Major qualitative features are reproduced.

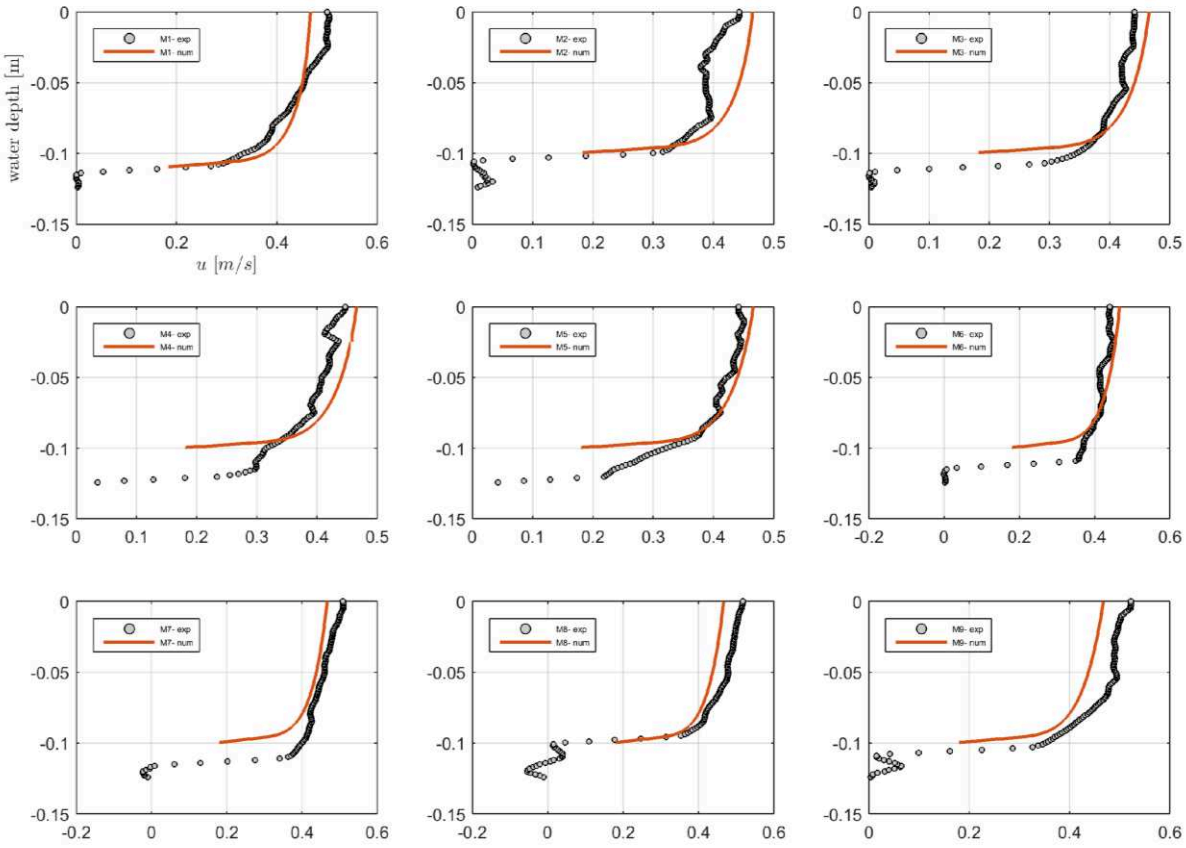

Figure 14: Comparison of flow velocities by experiment (dots) and numerical simulation (red) at nine measurement stations (M1 – M9) along the laboratory flume for a discharge of 90 l/s (Q90P).

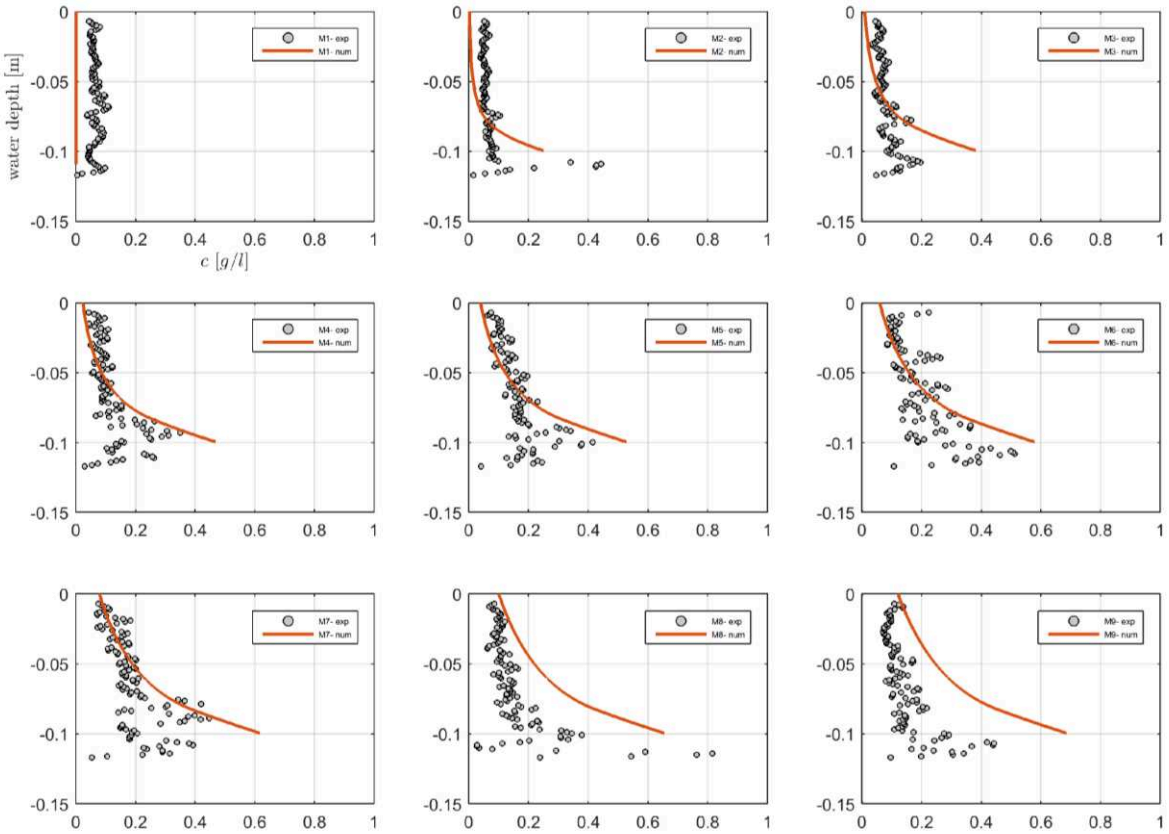

Figure 15: Comparison of concentrations by experiment (dots) and simulation (red) at nine measurement stations (M1 – M9) along the laboratory flume for a discharge of 90 l/s (Q90P).

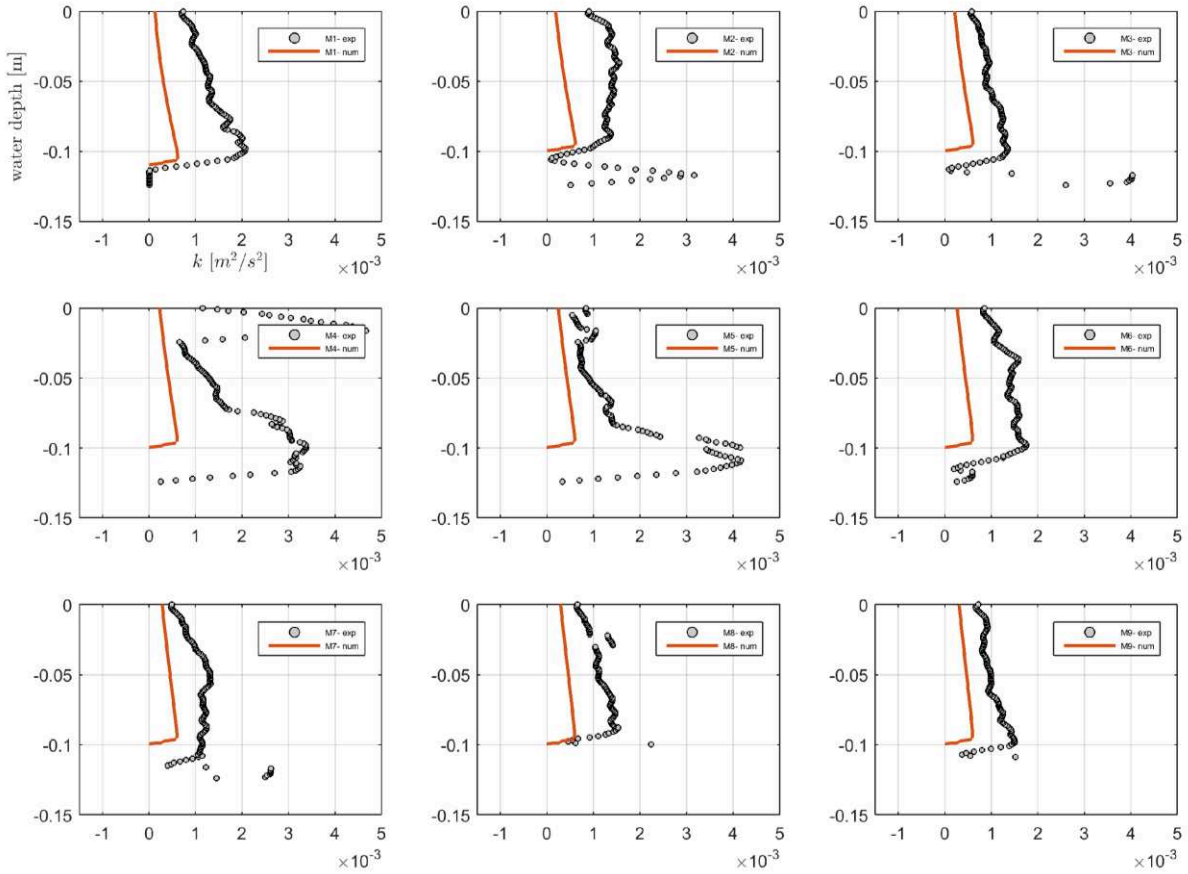

Figure 16: Comparison of turbulent kinetic energy by experiment (dots) and numerical simulation (red) at nine measurement stations (M1 – M9) along the laboratory flume for a discharge of 90 l/s (Q90P).

6.2 Tidal channel

The schematic estuary is based on a channel by Warner et al. (2005), who analyzed the performance of different turbulence models. Therefore, one secondary objective of the application of the extended continuous model set-up to this channel is to compare the performance of UnTRIM and the applied turbulence models with results given in literature (Warner et al. 2005). Afterwards, the main objective is the implementation of fluid mud in the schematic estuary and the sensitivity analysis of the extended model set-up.

6.2.1 Method

6.2.1.1 Grid

The schematic estuary is 100 km long with a variation in depth from -10 m NHN to -5 m NHN (see Figure 17). It has a constant width of 500 m and at the side boundaries free slip is defined.

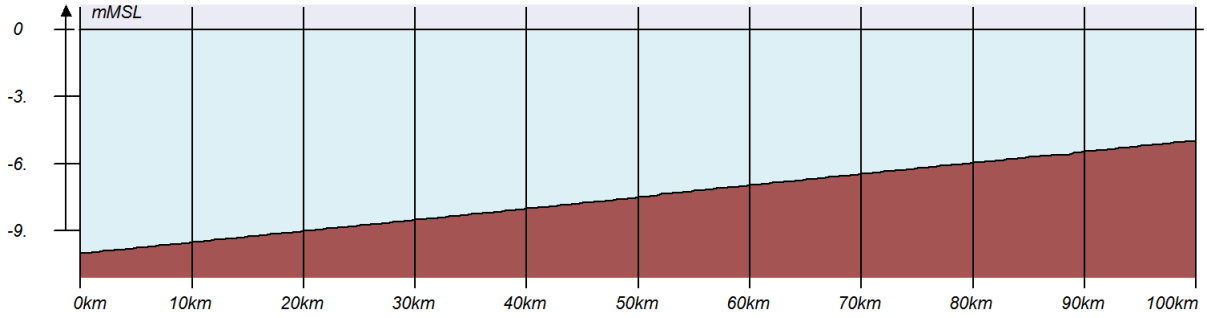

Figure 17: Schematic Estuary, i.e. channel after Warner et al. (2005).

6.2.1.2 Boundary values

In Warner et al. (2005) boundary conditions are specified as depth-averaged river flow at the head (x = 100 km) and the same flow, modulated with tidal oscillations, at the ocean boundary (x = 0 km).
In UnTRIM, the following boundary values are considered:

- Ocean end
  - open water level boundary
    Harmonic Value:
    period: 43200.00 sec; phase: 1.5607 (~π/2), amplitude: 0.40 m
    Constant value: 0.0 m NHN
  - constant salinity 30 PSU
  - SCC: 0 g/l

- River end: flow section
  - inflow 200 m^3/s
  - constant salinity 0 PSU
  - SCC: 0 g/l

6.2.1.3 Initial values

The initial water level is 0.0 m NHN and the initial flow velocities were set to zero. The initial salinity distribution is uniform at each end of the model (0 PSU at river end and 30 PSU in the ocean) and is vertically well mixed with a longitudinal gradient between x =30 km and x = 80 km (see Figure 18).

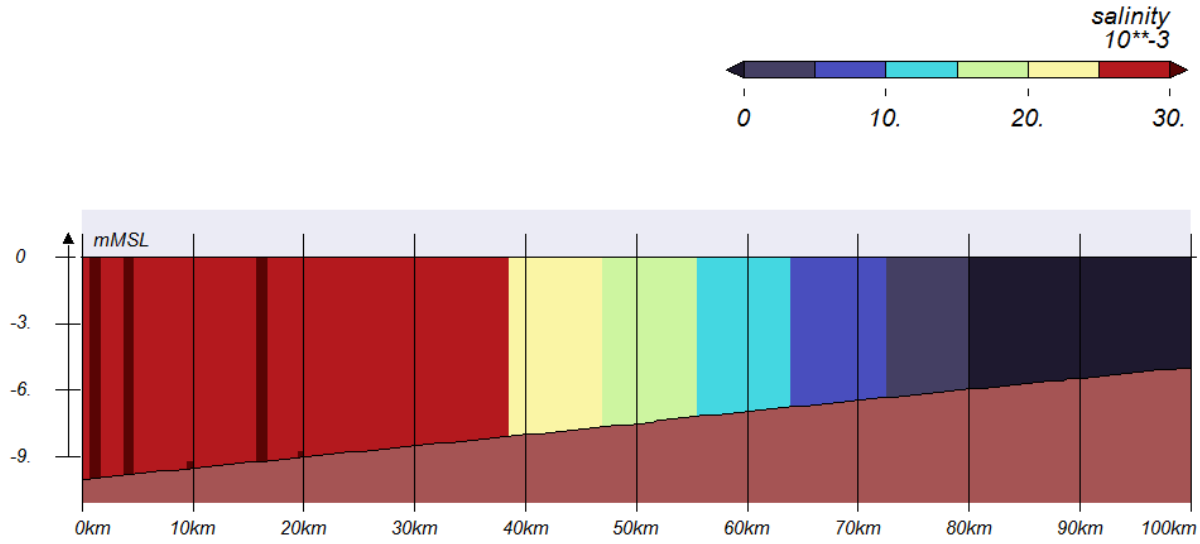

Figure 18: Initial salinity distributions for Warner Estuary.

For the sediments, after ten days the bed is initiated with a uniformly distributed sediment layer of 0.001 m thickness.

6.2.1.4 Further settings

Further model parameters for the schematic estuary are summarized in Table 2.

Table 2: Model parameters for Schematic Estuary.

Model parameter	**Variable**	**Value**
Length, width, depth	L, B, depth	100,000 m, 500 m, 10-5m
Discretization	dx, dy, dz	250 m, 500 m, 1 m
Time step	Dt	10 s
Bottom roughness	z_{ob}	0.005 m
Settling velocity	w_s	0.5 mm/s
Erosion rate	Eo	1x10-4 kg m-2 s-1
Critical stresses	tau_{cd}, tau_{ce}	0.05 N/m^2

6.2.2 Results

6.2.2.1 Comparison with Warner et al. (2005)

The secondary objective is to compare the performance of UnTRIM and the applied turbulence models by results given in literature (Warner et al. 2005). However, there seem to be discrepancies in given values for boundary values, initial values and calculated volumes in Warner et al. (2005). Since the results are very sensitive to these settings, a sound comparison as intended is unfortunately not possible. A general qualitative comparison is given in Figure 19, Figure 20, and Figure 21, showing that major qualitative features are reproduced. The differences are of only

marginal significance. The essential effects are reproduced. As a next step fluid mud can be implemented in the model and system studies can be performed.

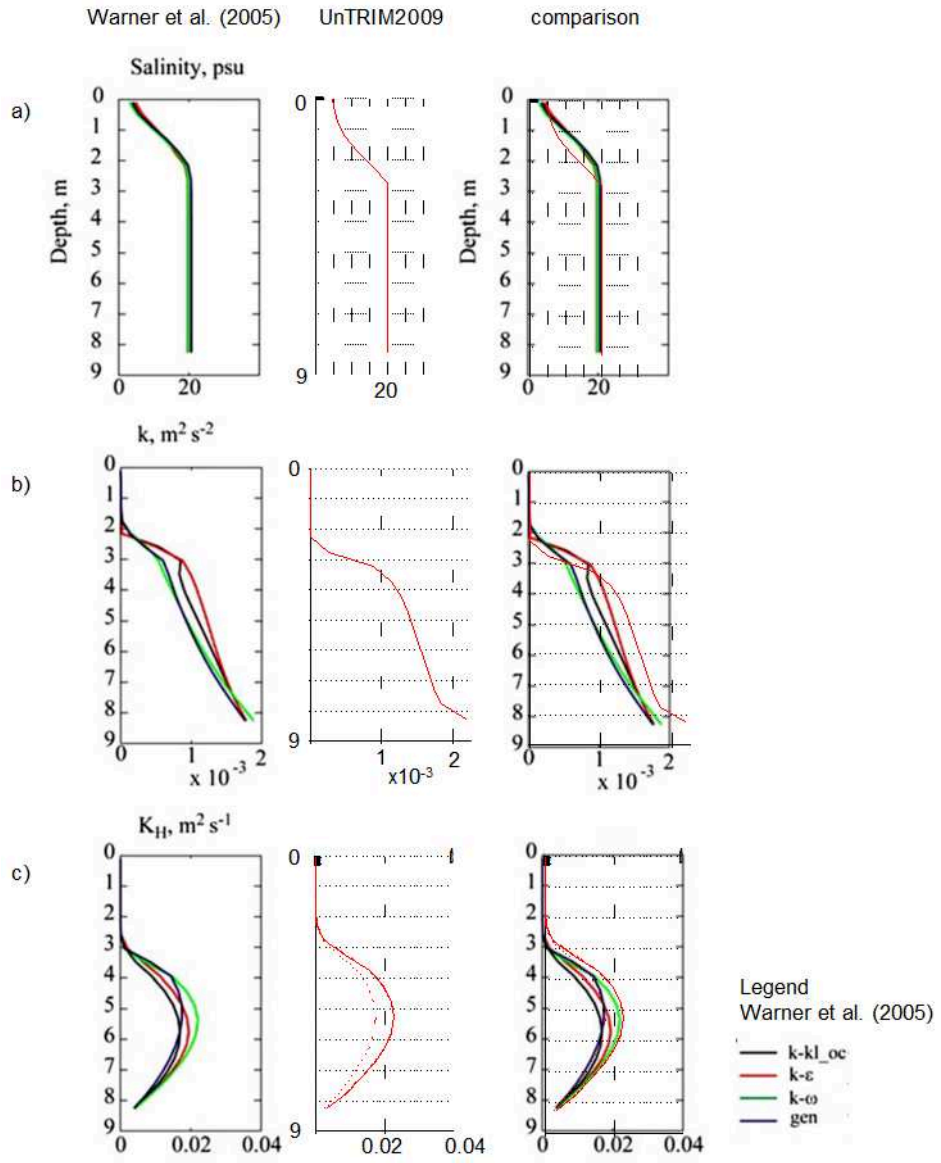

Figure 19: Vertical profiles of a) salinity, b) turbulent kinetic energy, and c) eddy diffusivity; left: Warner et al. (2005), middle: UnTRIM 2009, right: comparison (after 14.4167 days at x = 30 km).

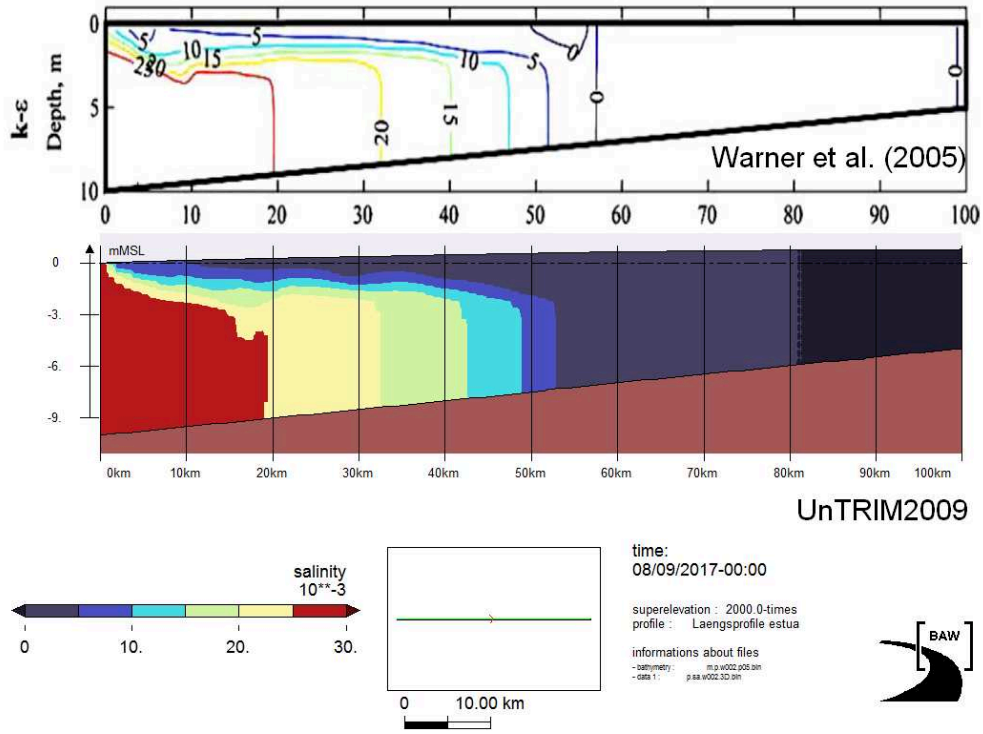

Figure 20: Modelled salinity fields at end of flood after 16 days (32 tidal cycles); top: Warner et al. (2005), bottom: UnTRIM2009.

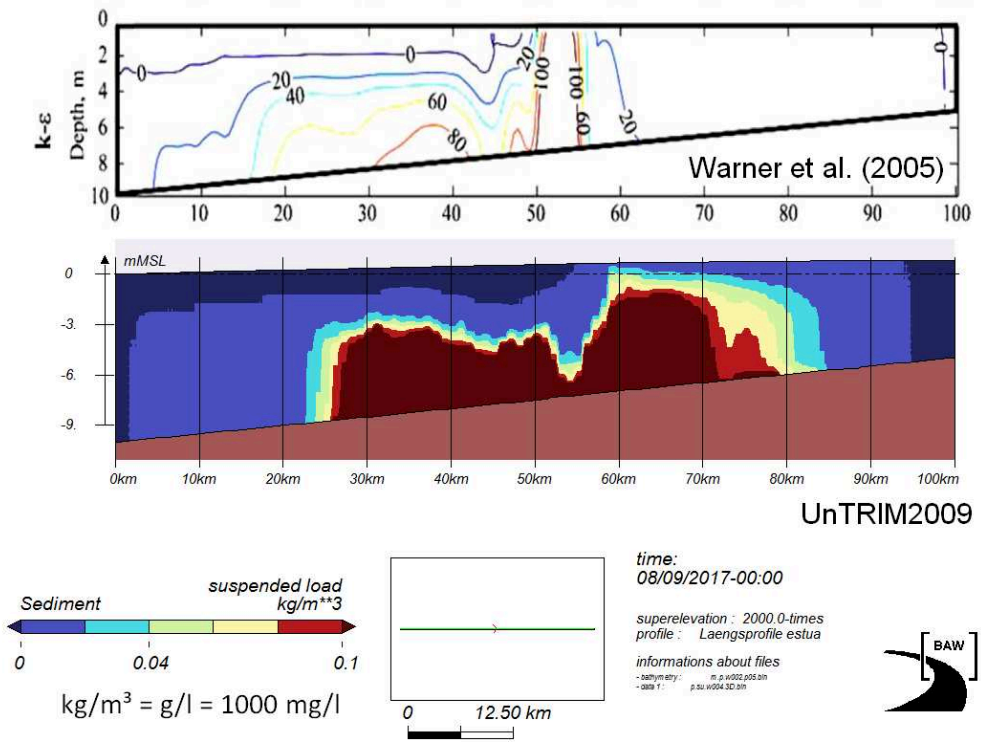

Figure 21: Modelled suspended-sediment concentrations near a maximum ebb current after approximately 16 days (SSC started at day 10, i.e. 12 tidal cycles incl. SCC); top: Warner et al. (2005), bottom: UnTRIM2009.

6.2.2.2 Implementation of fluid mud

For the implementation of fluid mud, the following settings were chosen:

- No exchange with bed layer
- Initial values of sediment concentration of 20 g/l
- Settling velocity considering flocculation and hindered settling by van Rijn (1993), with gelling concentration of 10 g/l and maximum settling velocity of 2.4 mm/s (see Figure 22)
- Vertical resolution of 1 cm at the bottom up to 20 cm

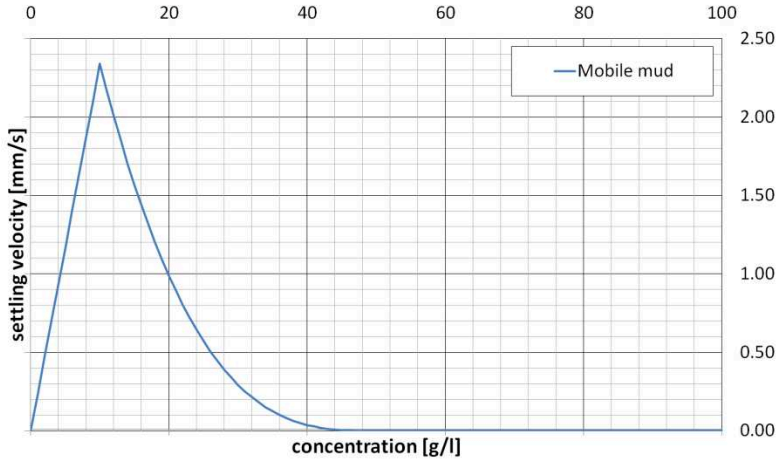

Figure 22: Settling velocity after van Rijn (1993).

The model results of a) SSC, b) current velocity, and c) salinity are shown in Figure 23.

For the schematic estuary is no validation data available. Therefore, a qualitative comparison with in-situ observations in the Ems Estuary by Becker et al. (2018) could be performed. The following results are in general comparable:

- Position of the lutocline at one half of the water column (see Figure 23 a)
- Modelled SSC up to 40 g/l in mobile fluid mud layer (see Figure 23 a)
- Reduction of hydraulic depth due to fluid mud layer, increased flow velocity above fluid mud layer (see Figure 23 b);
- Flow reversal in fluid mud layer, i.e. downstream in fluid mud layer, upstream in upper water column during the end of the flood phase (not shown here);
- Reduction of hydraulic depth due to fluid mud layer, advection of salt in the upper part of the water column could be modelled (see Figure 23 c).

However, further improvements are needed for:

- Turbulence in fluid mud
- Entrainment of fluid mud layer (vertically mixed) at beginning of flood

This will be discussed further in the next section 6.2.2.3.

a) SSC [kg/m^3]

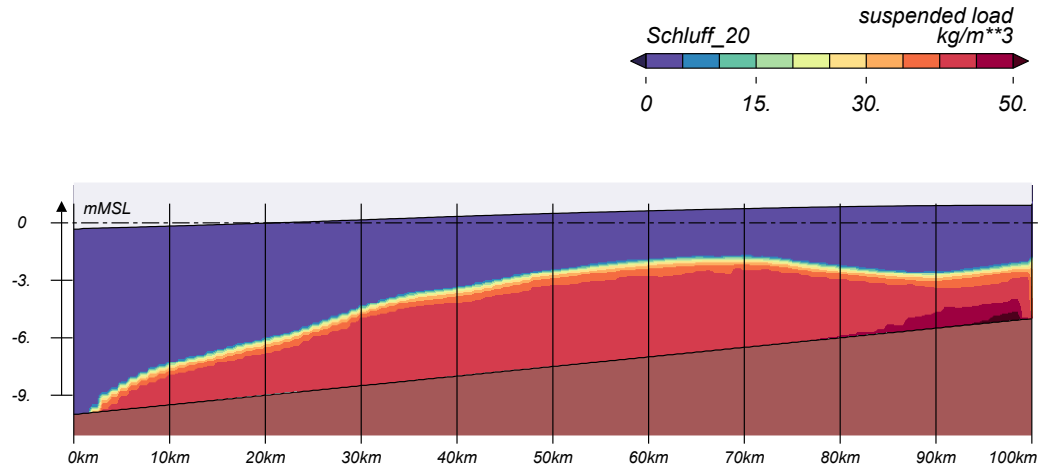

b) current velocity [m/s]

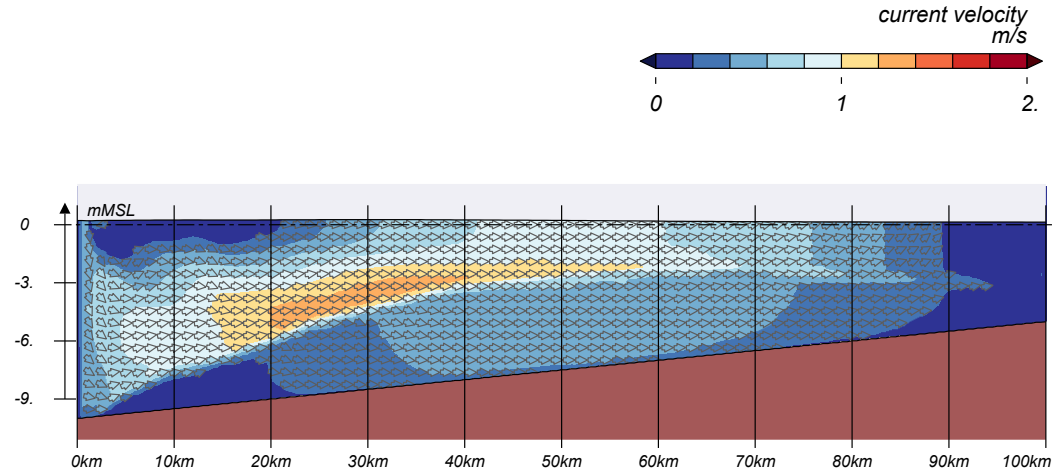

c) salinity

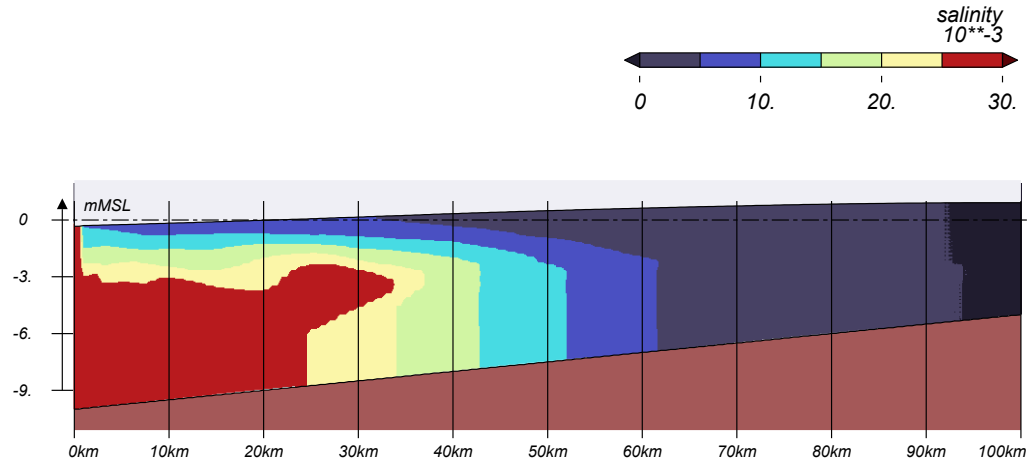

Figure 23: Model results: a) SSC, b) current velocity, c) salinity.

6.2.2.3 Variation of rheological viscosity

The modelling of fluid mud in the schematic estuary revealed that there was still turbulence in the fluid mud. In order to analyze the effect of the rheological viscosity on the turbulence, numerical tests with a variation of the rheological viscosity were performed.

Exemplarily the results for a constant rheological viscosity of $v_r = 0.01$ m^2/s for concentrations above 10 kg/m^3 are discussed and compared to the applied parametrization.

The results are shown in Figure 24. For the two viscosities as results the (a) SSC, (B) current velocity, (c) turbulent kinetic energy, and (d) effective viscosity are shown.

The increase of the rheological viscosity

- reduces the current velocity,
- reduces the tidal range,
- effects the sediment concentration and the position of the lutocline, and
- reduces the turbulence in the fluid mud.

The turbulence is reduced by a rheological viscosity in the range of 0.10 [m^2/s].

Former studies, e.g. Malcherek and Cha (2011) applied high shear rates for the rheometrical analysis of the parametrization of the rheological viscosity, e.g. shear rates of up to 450 [1/s]. Furthermore, Wehr (2012) assumed higher densities inside the fluid mud layer, e.g. 1030 kg/m^3 at the lutocline, 1080 kg/m^3 at half of fluid mud layer, and 1150 kg/m^3 at the bottom.

At that time, the in-situ observations of Becker et al. (2018) were yet not available. Becker et al. (2018) revealed bulk densities of 1020 kg/m^3 at the lutocline and a maximum bulk density inside the fluid mud layer of approximately 1040 kg/m^3. Moreover, maximum shear rates of approximately 26 [1/s] were measured. Hence, the measured values appear to be lower than previously assumed.

As a consequence, an adaptation of the parametrization of the rheological viscosity seems to be necessary. For the schematic estuary an adaptation of the rheological viscosity in the range of 0.10 [m^2/s] seems to be appropriate since the turbulence is then reduced. For the Ems Estuary further research is necessary and further validation data is needed.

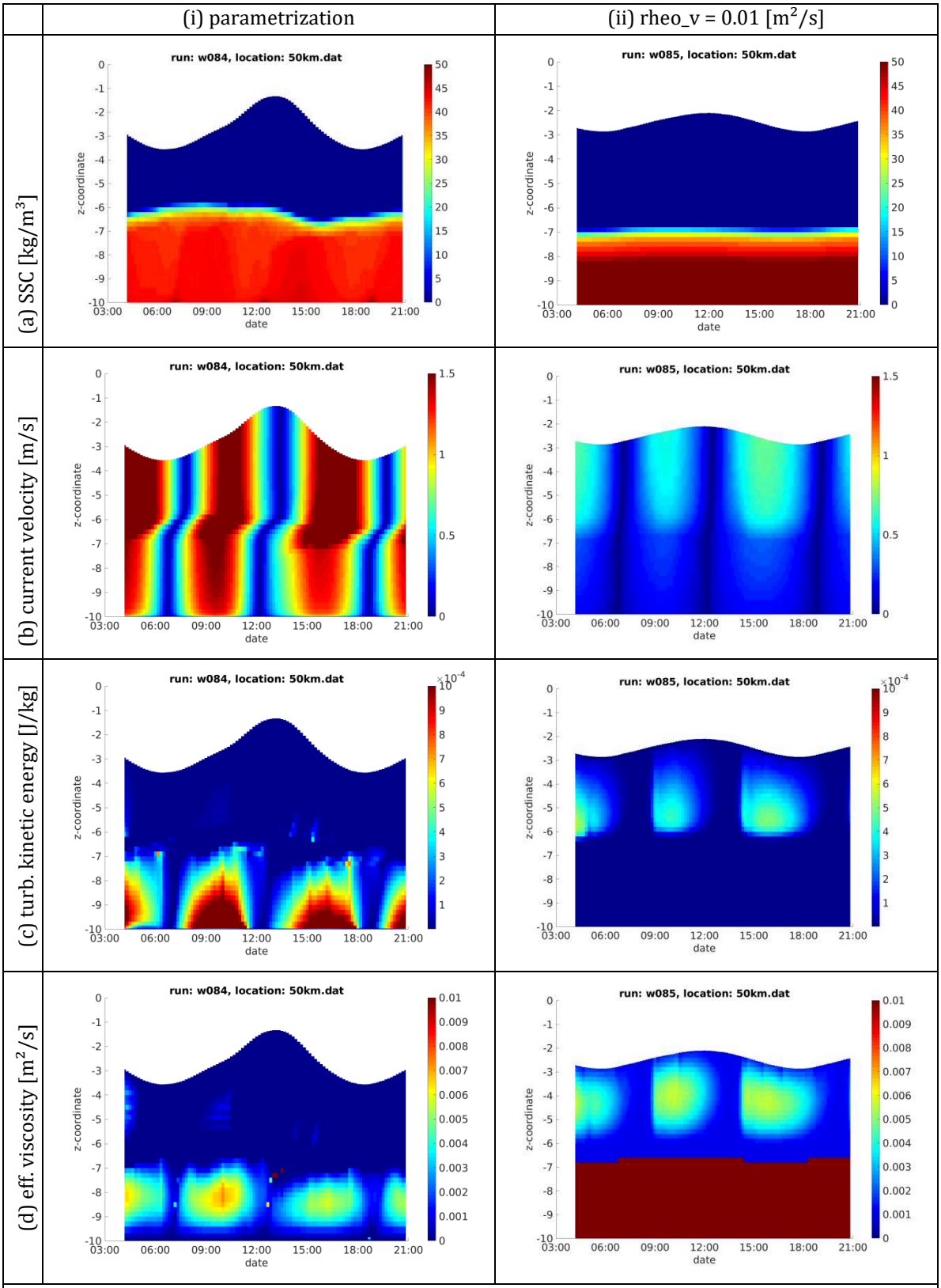

Figure 24: (a) SSC, (b) current velocity, (c) turbulent kinetic energy, and (d) effective viscosity for (i) parametrization and (ii) rheo_v = 0.01 [m²/s].

6.3 Summary and intermediate conclusion

The main objective is to develop and analyze a method describing the interaction of tidal dynamics and fluid mud. Therefore, the extended continuous model set-up was applied and described in this chapter. After an introduction of the general concept, the mathematical descriptions of the most important physical processes for modelling fluid mud dynamics were given.

This includes the following components:

- effective viscosity consisting of a rheological viscosity and a turbulent viscosity
- flocculation and hindered settling
- adapted boundary conditions and new interpretation of k-ω-turbulence model

These components were implemented in a numerical model. For this purpose, modules were newly created or adapted in FORTRAN. The extended continuous model approach combined turbulence and mud rheology. An application could be confirmed with adapted boundary conditions and a new interpretation of k-ω-turbulence model. The extended model set-up was successfully applied for the numerical simulation of a laboratory flume and a schematic estuary. The results were documented in this report.

However, the extended continuous model approach results in new challenges. The new simulation methods require high computing power. Moreover, the formation and dynamics of fluid mud are an interplay of various processes and effects, for which there are still sensitivities of parametrizations and lack of validation data. For these reasons the application to more a nature system such as the Ems estuary was currently not expedient.

Future research is urgently needed. Moreover, further development of the turbulence model is required, e.g. extending the k-ω-model to the buoyancy effect (Umlauf et al. 2003) or the new k-ω model by Wilcox (2008) . The mud-induced periodic stratification can be modelled by a combination of settling velocity, diffusivity, rheological viscosity and turbulence damping. The modelling results are essentially determined by sensitivities, e.g. of the parameterizations for which validation data are missing. A verification of cause-effect links is of fundamental importance. Since it is very difficult to achieve natural conditions in the laboratory, there is a clear demand also for further in-situ observations in the field, e.g. estimating turbulent kinetic energy.

III Historic scenarios of Ems Estuary

Next to the physical and numerical description of the behavior of fluid mud, the development of fluid mud and causes of siltation in estuaries are further aspects, which are not yet fully understood. Therefore, work package 3 of the project includes the simulation of historic scenarios of the Ems Estuary.
The numerical model UnTRIM is applied to historic scenarios of the Ems Estuary. Reasons for the extreme formation of fluid mud and indicators for it are supposed to be identified and the influence of the human impact analyzed.

In order to examine the sediment dynamics leading to the formation of the fluid mud, the extended model set-up developed in work packages 1 and 2 and described in part II of this report should have been applied to these historic scenarios. The sensitivity of parameters and insufficient validation data prevented this, as explained in the previous sections. Therefore, the focus here lies on the investigation of the hydrodynamic conditions in three-dimensional, highly resolved numerical models of the historic conditions during three important periods in the Ems Estuary. The focus on hydrodynamics has the advantage that reliable data for the water level exists also for historic periods, allowing a thorough calibration of the model.
These periods were chosen before (in the 1930s and 40s), during (1980s) and after (2015) some of the major anthropogenic interventions. The development between these periods and the comparison of the hydrodynamic parameters allows us to trace the changes in the estuary that led from a system in equilibrium to a mud-importing system.
Due to the lack of quality of the available data, scenarios were developed, in order to not reproduce one exact year, month or day, but to illustrate the characteristic behavior of the estuary during these periods. Therefore, only little time-series, but mostly analyzed parameters averaged over a full spring-neap cycle during a period with low discharge were investigated.

Before the set-up of the numerical model, a literature research and evaluation of the historic development of the estuary are described in chapter 7 as well as appendix 12. Section 8 contains the description of the scenarios and the method as well as the results of the simulations and a discussion and summary.

7 Historic development of the Ems Estuary

The Ems Estuary is a highly dynamic system, evolving naturally as well as due to human interventions. Some selected aspects of these developments will be mentioned in section 7.1, while section 7.2 contains references to previous studies of the historic development of estuaries.
A comprehensive literature review of the anthropogenic influences on the Ems Estuary is described in Appendix 12.1. Measures that are important for the simulations will also be mentioned in section 8.1.2. In Appendix 12.2 and 12.3 the dredging activities in recent years as well as measurements of the hydrology are described thoroughly.
In Section 8 the effects of some of these measures will be investigated systematically.

7.1 Overview

After the formation of the Dollart, the Leybucht and a meander of Emden in the 14th and 15th century, the major anthropogenic interventions in the Ems Estuary started with the construction of the Geise training wall (German: Geiseleitdamm) from 1870 to 1899 and canalizations (straightening of meanders in the Lower Ems) between the 1890s and 1980s. Further severe interventions were the construction of the Leda barrage in 1954, the construction and expansion of the ports of Delfzijl, Eemshaven and Emden, dike constructions and the activations of the storm surge barrier near Gandersum (Lang 1954; Janssen 1968; Lange 2006; Krebs and Weilbeer 2008; Herrling and Niemeyer 2008c).

Another important aspect of anthropogenic interventions in the Ems Estuary is river engineering, such as deepening, straightening and dredging. Since the beginning of the 20th century, the fairway of the Ems Estuary has been repeatedly deepened. The strongest deepening of the Lower Ems took place between 1981 and 1992, as can be seen in Figure 25. After that, the required depths were mainly obtained by demand dredgings for the transfer of deep-going vessels from Papenburg to the sea (see Figure 71). From 1954 to 1994 dredged material was mainly dumped on agricultural sites on land. Afterwards, the material from the outer Ems and Emder Fairway was dumped on sea dumping sites, instead of taking it out of the system (see Appendix 12.2) (Krebs and Weilbeer 2008; van Maren et al. 2015a). Overall, the dredging volumes increased immensely over the last 70 years, especially in the Lower Ems and with a strong increase between the 1980s and 2000, which can be seen in Appendix 12.2 in Figure 70 and Figure 71.

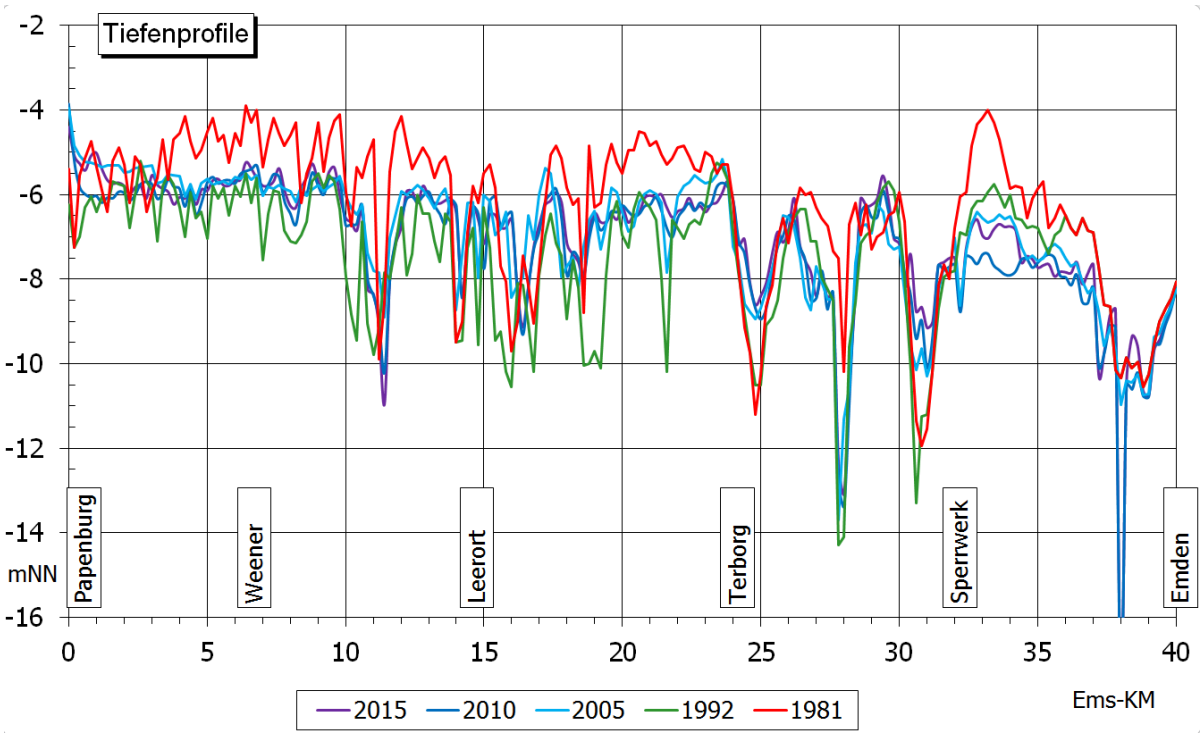

Figure 25: Development of the channel from 1981 - 2015 (BAW).

More details on these and further anthropogenic influences are described in Appendix 12.1 and 12.2.
Further influences defining the characteristics of the estuary are the discharge and sea level. These, as well as measurements of the resulting tidal characteristics, salinity and sediment concentrations and biogeochemical parameters are described in Appendix 12.3.

7.2 Literature on historical investigations of estuaries

Several studies have already been performed investigating the historical development of estuaries, especially the Ems. Some of them are mentioned in the following in chronological order. This list is not intended to be exhaustive but rather tries to give an overview over the many possibilities of investigating historic developments of estuaries.

Herrling and Niemeyer (2008c)
In 2008, the Coastal Research Station of the Lower Saxony Water Management, Coastal Defence and nature Conservation Agency (NLWKN) worked on a project called HARBASINS (Harmonised River Basins Strategies North Sea). One part of that was the "Reconstruction of the historical tidal regime of the Ems-Dollard estuary prior to significant human changes by applying mathematical modeling". (Herrling and Niemeyer 2008c)
Data was mainly taken from nautical charts and cross sections from the years 1923 to 1952 as shown in Figure 26. This collected topography is also used in this project, as described in section 8.2.1.
The results were compared with a state of 2010 in Herrling and Niemeyer (2008a) and are also mentioned in section 8.4.5.

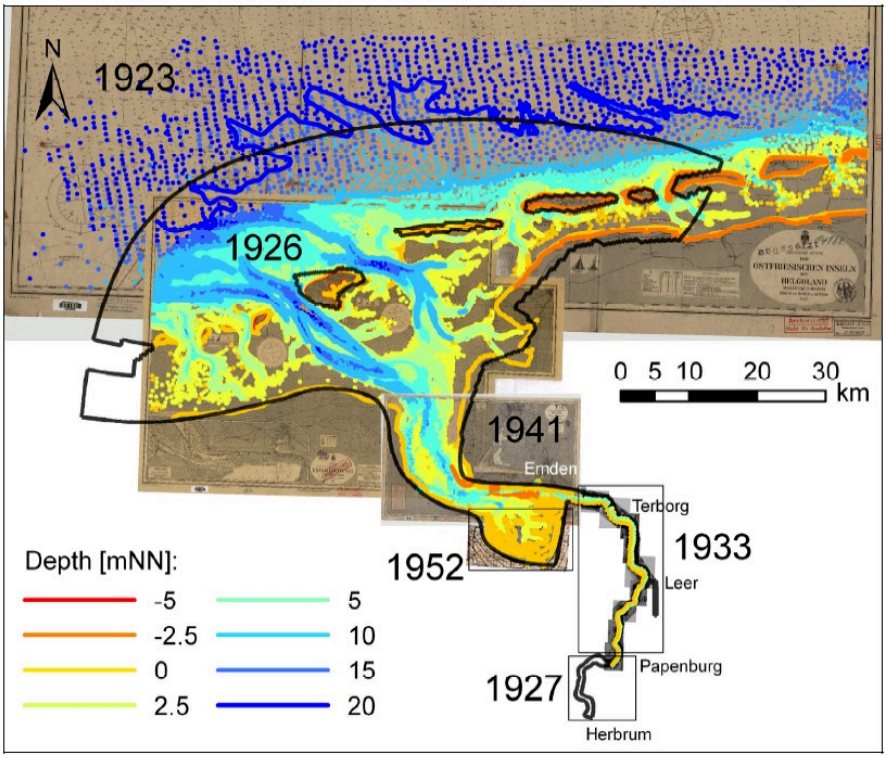

Figure 26: Topographic data between 1923-1952 (Herrling and Niemeyer 2008c)

Chernetsky et al. (2010b)
The authors evaluate the physical mechanisms resulting in the trapping of sediment by sensitivity studies using a 2DV numerical model in the Ems Estuary with scenarios in 1980 and 2005. "The upstream movement of the estuarine turbidity maximum into the freshwater zone in 2005 is mainly the result of changes in tidal asymmetry. Moreover, the difference between the sediment distribution for different grain sizes in the same year can be attributed to changes in the temporal settling lag." (Chernetsky et al. 2010a, p. 1220)

Winterwerp (2010)
Winterwerp (2010) describes the up-river transport of fine sediments in the Ems River by a 1DV model, relating it to an asymmetry in vertical mixing, driven by the tidal asymmetry. The regime shift is characterized according to data from 1990 and predicting a further shift in the future.
SPM data from 1954, 1975 and 2005 is compared, as well as extensive data from a measurement campaign in 1990.

van Maren et al. (2012a; van Maren et al.; 2012c; 2015a; 2015b)
A historic scenario of the Wadden-Sea- and Ems-Dollard-Region (WED model) for 1985 was created from data by the Dutch ministry of Public Works and compared with measurements. Models of the Ems river were built for the years 2005, 1985, 1965 and 1945 (see also Schoemans (2013)), mostly using the maintenance and navigational depths. (van Maren et al. 2012c)
Identical hydrodynamic forcing is used, varying the hydrodynamic roughness. From the 1945 scenario to the one representing 2005, the calibrated Manning coefficient is approximately halved. (van Maren et al. 2012c)
A detailed analysis and comparison of the scenarios with regard to fine sediments can be found in van Maren et al. (2012a).
These models and results are also published in van Maren et al. (2015b).
The impact of channel deepening and dredging on the suspended sediment transport is investigated by van Maren et al. (2015a), finding that deepening is one of the main factors enhancing the up-stream sediment transport.

Winterwerp et al. (2013)
A linear analytical model for the tidal movement in narrow, converging estuaries is applied to the historic development of Elbe, Ems, Loire and Scheldt. It is a conceptual model and not yet validated. (Winterwerp et al. 2013)

Jonge et al. (2014)
Measurements in the Ems estuary are compared between 1954 and 2005, showing an increase in SPM concentrations and a shift of the ETM. Later a semi-analytical model is applied to five time periods between 1965 and 2005. (Jonge et al. 2014)

van Rijn and Grasmeijer (2018)
The authors developed a simplified model for simulating mud transport in tidal conditions in order to "gain quantitative understanding of the effects of channel deepening on mud transport" (van Rijn and Grasmeijer 2018, p. 1481). From this they developed conditions, in which a regime

shift from export to import of mud is possible. These are described and applied to the results obtained in MudEstuary in section 8.4.5. (van Rijn and Grasmeijer 2018)

Grasso and Le Hir (2019)
The development of the estuarine turbidity maximum (ETM) location in the Seine River is explored by analyzing measurements and simulation, investigating the relative contribution of the gravitational circulation and tidal pumping mechanisms on the dynamics of the ETM. They chose three diachronic scenarios from 1960 until 2010, using the same forcing and bottom roughness in all scenarios and analyzed hydrodynamics, salinity, SSC (with focus on the mud class) and ETM location and mass. They connect channel narrowing with the decrease of tidal asymmetry. Tidal amplification according to them results from channel deepening. (Grasso and Le Hir 2019)

Dijkstra et al. (2019a; 2019b)
In Dijkstra et al. (2019b) an idealized width-averaged model of the Ems Estuary for 1965 is calibrated and then applied to the state of 2005. It is used in order to explain the changes in sediment concentrations and relate them to channel deepening. Furthermore, the effect of the resonance of the M4 tide is analyzed. It is found that the M4 tidal component has an important effect on the sediment import. Furthermore, the upstream shift of the ETM could be reproduced.
Dijkstra et al. (2019a) continue the work, analyzing the different regimes for a state with low and for a state with high sediment concentrations. It is found that a shift from one state to the other depends on river discharge and channel depth. From observational data, the regime shift in the Ems Estuary is dated to a time around 1989.

8 Numerical simulations

In order to analyze the development of the Ems estuary, numerical investigations are conducted, using a three-dimensional model and three different scenarios, representing different phases in the development of the estuary. In the following the model, as well as the scenarios, boundary conditions and the calibration procedure are described. In section 8.4 the results are summarized and discussed.

8.1 Data sources

8.1.1 Bathymetry

In order to model historic scenarios, bathymetric data from different sources had to be collected, sorted and selected. The main sources that were used are

- HARBASINS project for the 1930s scenario (Herrling and Niemeyer 2008c)
- Lower Ems profiles from 1981 (WSA, BAW)
- Bathymetry of parts of the Outer Ems 1990 (BAW)
- Bathymetry from Herbrum to Knock from 1992 (BAW)
- Complete bathymetry data from Herbrum to Huibertgat for 2005, 2010, 2015 (DGMW, BAW), The DGMW 2015, interpolated to the grid used here, is shown in Figure 27.

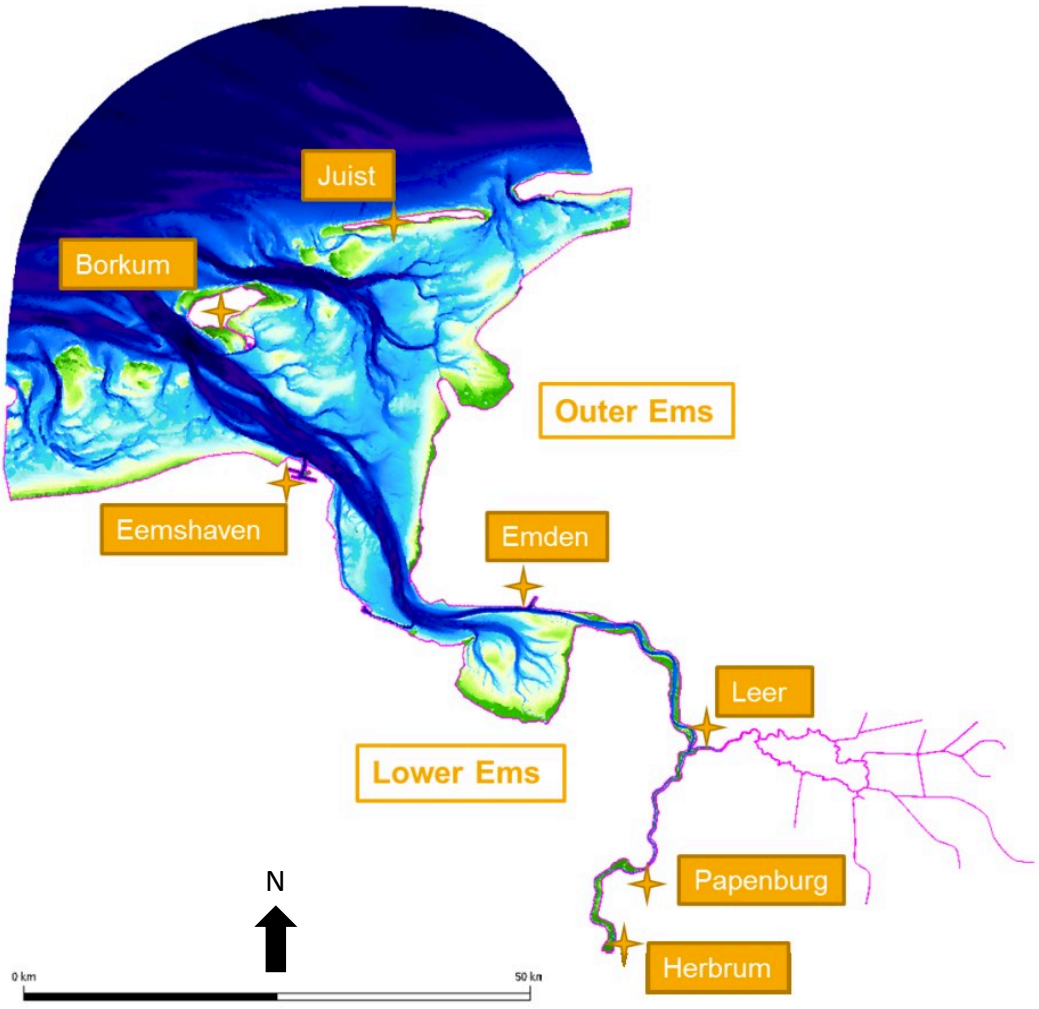

Figure 27: Overview of the Ems Estuary in the h2015 model with important locations.

8.1.2 Hydrological measurements

Unless stated otherwise, the hydrological measurements used for calibration are taken from WISKI, the official data portal by the German federal administration. For the historic periods, mostly high- and low water levels were available, while for 2015 the time series were analyzed by the same methods as the simulation data.

8.2 Historic topography scenarios

From the available data mentioned above, three main topographical scenarios are extracted. These are summarized in Table 3 and further described in the following paragraphs.

Table 3: Short description of historic scenarios

Short Name	Description
h1930s	Data between 1923 – 1952, digitalized by Herrling and Niemeyer (2008c), compared with measurements from 1958
h1980s	h2015 with the lower-Ems-channel of 1981 and outer and lower Ems bathymetric data from 1990 and 1992 (see Figure 31)
h2015	DGMW 2015

For a first impression, the depth along the longitudinal profiles for each scenario is plotted in Figure 28.

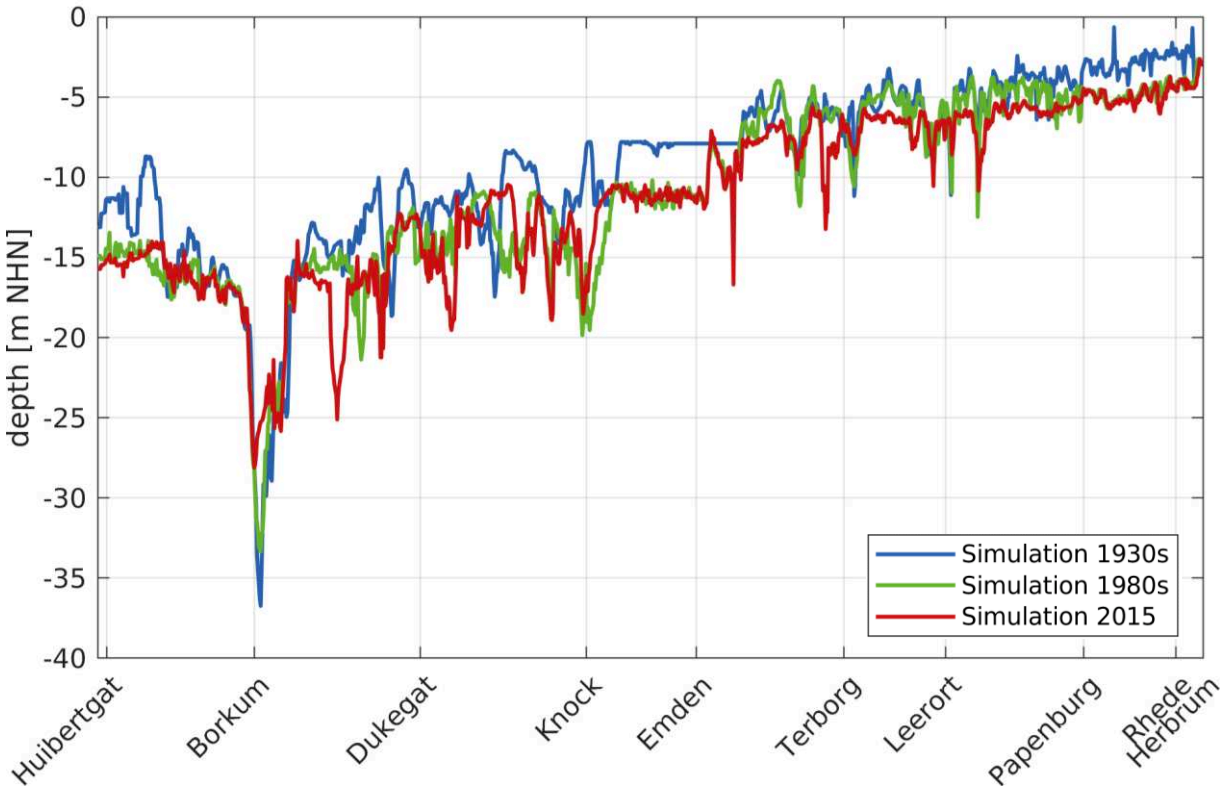

Figure 28: Depth along the longitudinal profile for all scenarios.

8.2.1 1930s

This topography was assembled by Herrling and Niemeyer (2008c), as mentioned in section 7.2. It describes a state of the Ems estuary before some of the major human impacts (see Appendix 12).

8.2.2 From h1930s to h1980s

The following impacts between the 1930's and 1981 were considered by adapting the grid:

1) embankments around the Leybucht (1947-1950)
2) filling of the Polder at Knock (from 1950)

3) construction of the Leda weir (1954)
4) avulsion of a meander at Herbrum due to the construction of winter dykes and construction of a new weir (1954-1965)
5) construction of deep water port at Delfzijl (1968-1973)
6) opening of the port of Eemshaven (1973).

The modifications are marked in Figure 29. The Leda and Jümme system is not shown, since in that area no data is available for the historic scenarios.

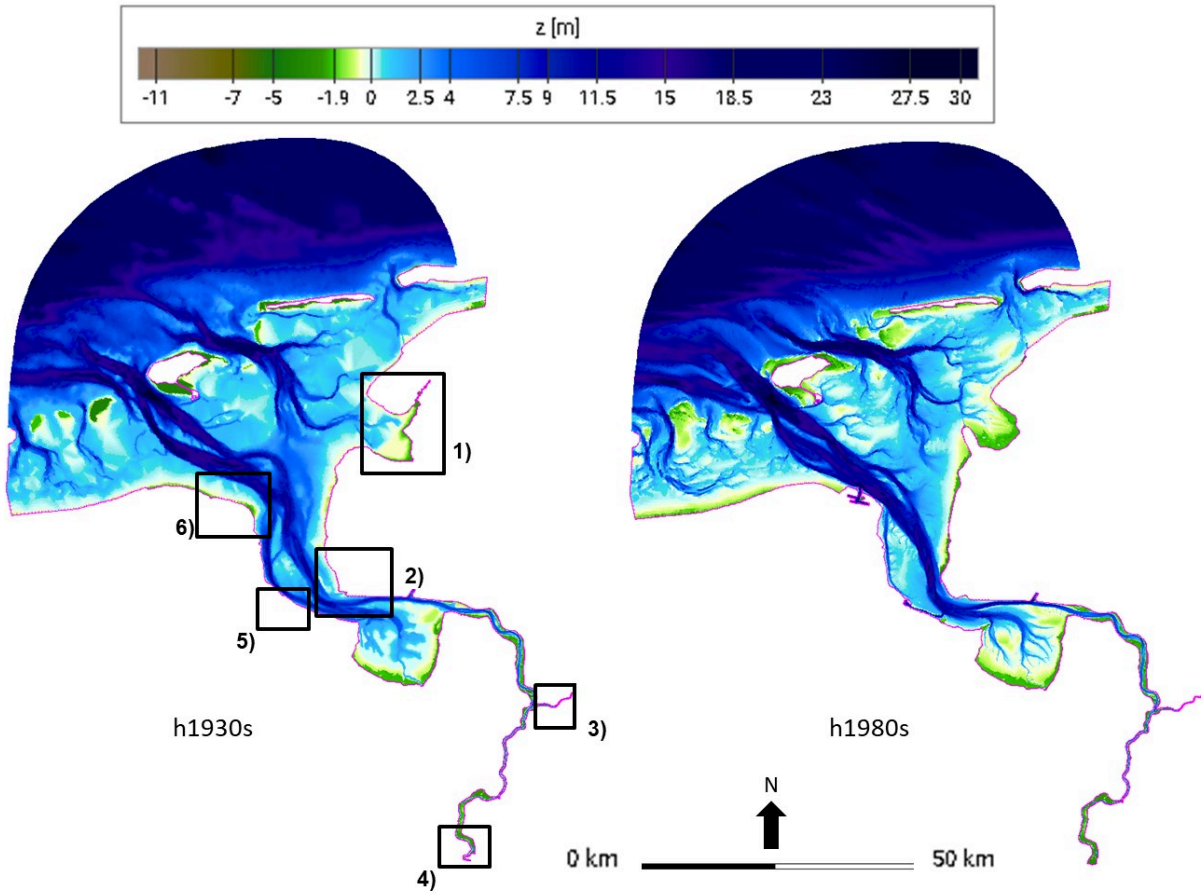

Figure 29: Bathymetries of the Ems estuary for the scenarios h1930s (left) and h2015 (right) with major changes 4) – 8).

8.2.3 h1980s

The depth profiles between Papenburg and Pogum are considered in the topography as is shown in Figure 30 and further data from 1990 and 1992 is added (see Figure 31). As a basis, the topography from 2015 is used, where ever no data from the 1980s and 1990s was available. Between Herbrum and Papenburg the changes between 1981 and 1992 can be neglected. In the Outer Ems and in the Emden/Dollard region, the error made by using only the bathymetry data from 2015 would have been quite high, even though van Maren et al. (2012b) assume a constant depth in the Emder fairway since 1965.

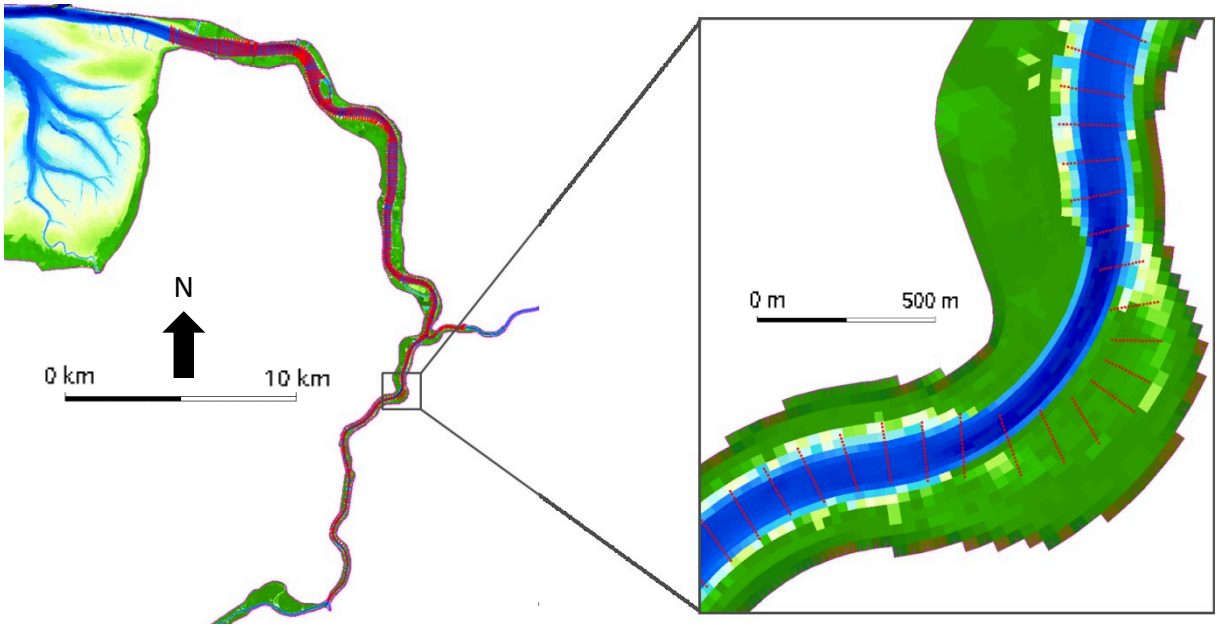

Figure 30: Including profile data from 1981 into 2015 topography.

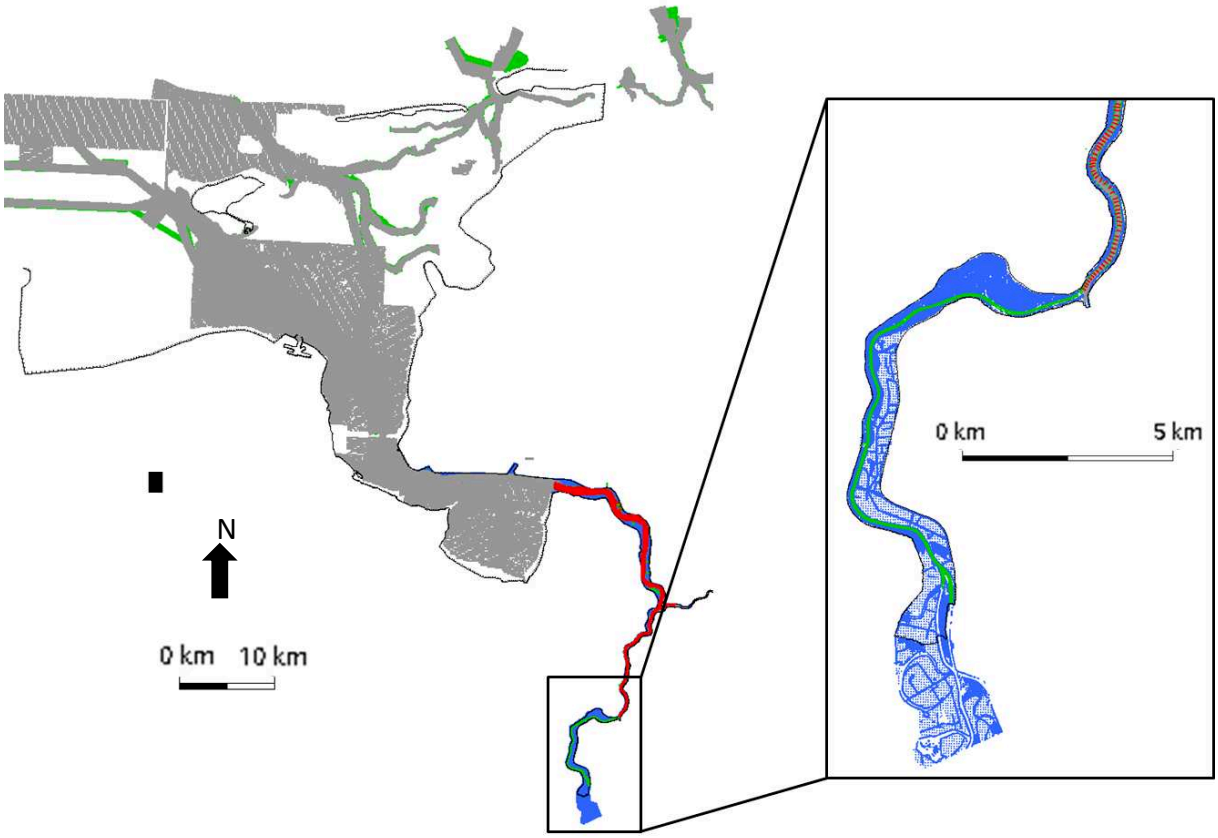

Figure 31: Data sources of bathymetry for Scenario h1981+90+92.
(red: cross sections from 1981, blue and green: data from 1992, grey: data from 1990).

8.2.4 From h1980s to h2015

Besides deepening some major changes from 1981 to 2015, for which the grid had to be adapted, were

7) straightening of the channel at Stapelmoor (1984)
8) straightening of the channel at Weekeborg (1984)
9) construction of the storm surge barrier (1998-2002)

These changes are marked in Figure 32, which shows the differences of the bathymetries of the lower Ems for the two scenarios.

Figure 32 shows the differences from scenario h1980s to h2015. It can be seen, that the channel is in most areas deeper in 2015 than it was 1981. However, some shore areas, especially upstream of the storm surge barrier are shallower, making the channel more narrow. The most prominent changes can be seen in areas where the grid was adapted, namely around Weekeborg, Stapelmoor and the storm surge barrier at Gandersum.

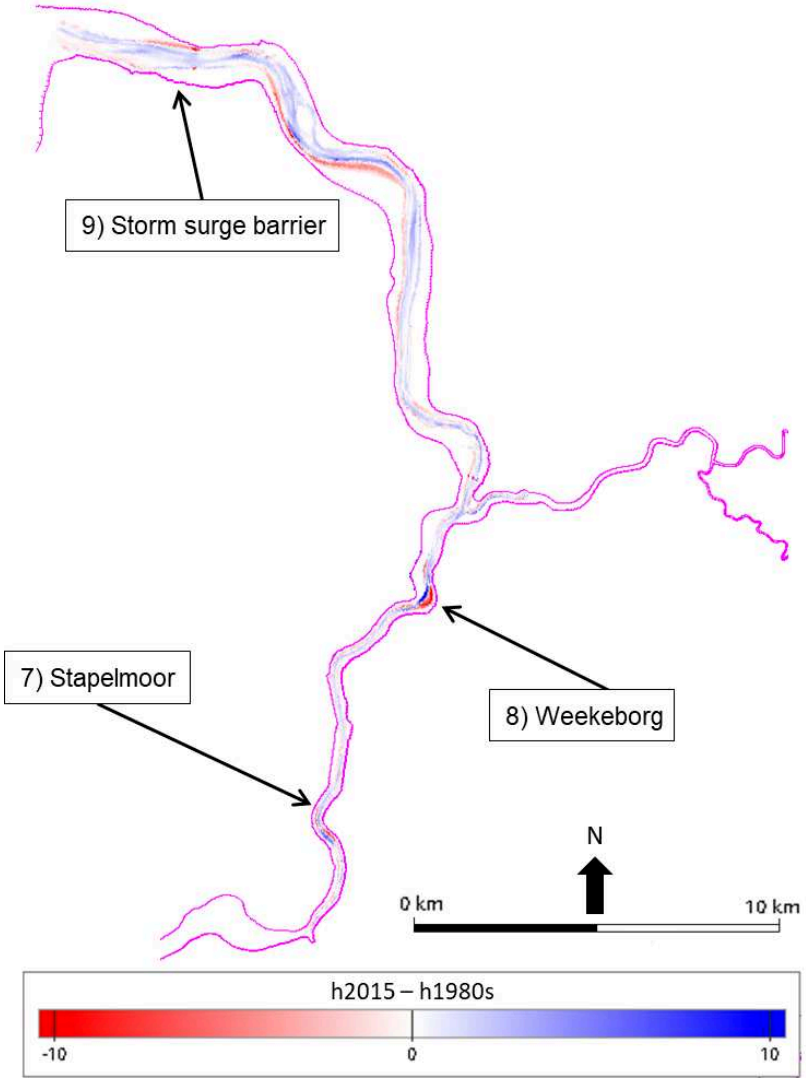

Figure 32: Differences between the grids for the scenarios h2015 and h1980s.

In Figure 33 the differences in topography from scenario h1930s to h2015 are shown. Major differences can be seen in the bight of Watum, which is less pronounced today than in was in the 1930s. Furthermore, the connection between Osterems and Westerems is deeper in the scenario h1930s than in h2015. Here most major differences can be observed in the outer Ems, while between h1980s and h2015 especially the Lower Ems was deepened and straightened (Figure 32).

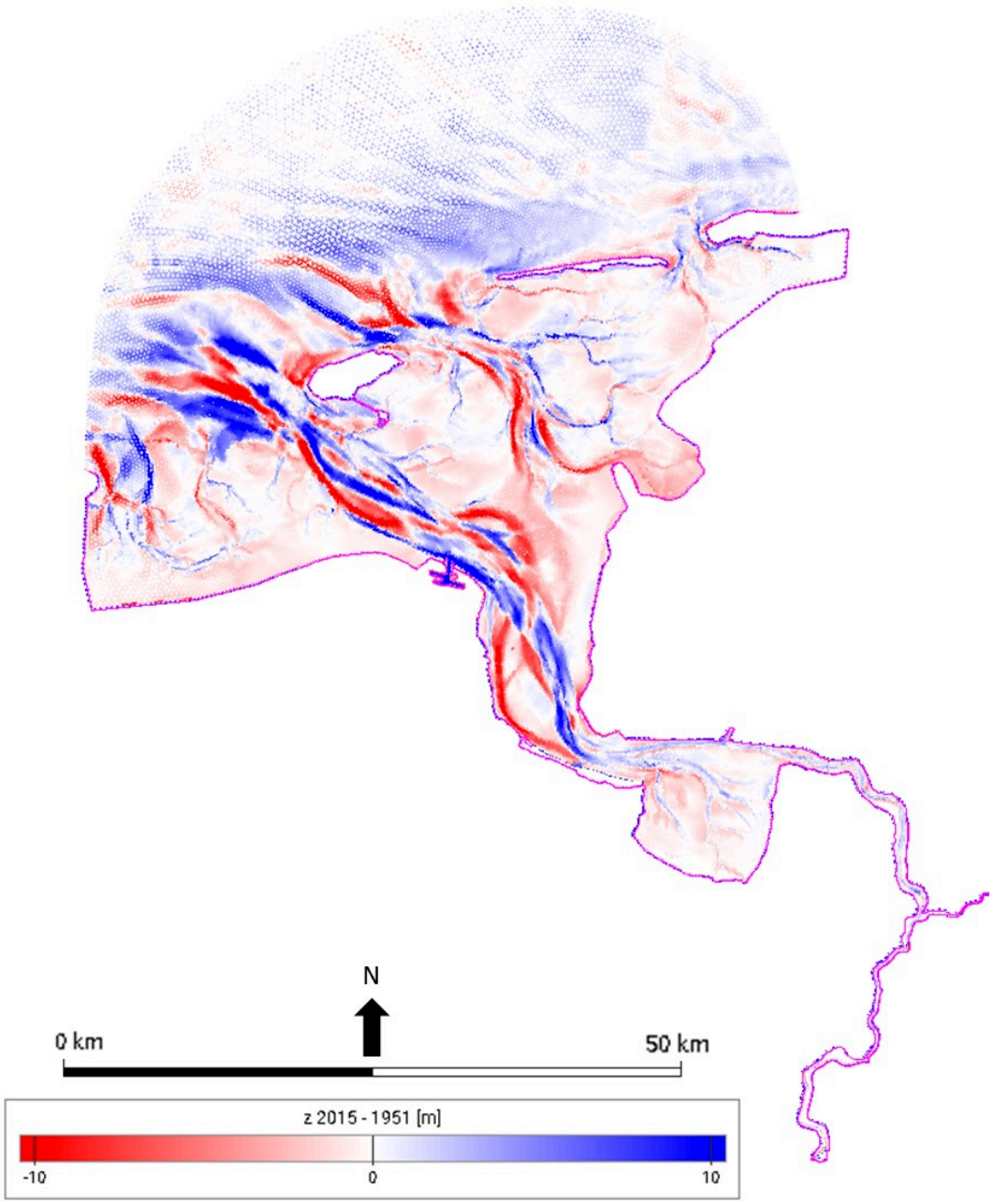

Figure 33: Differences between the grids for the scenarios h2015 and h1930s.

8.2.5 h2015

The scenario h2015 is the current condition used for the comparison and shown in Figure 27. The model is calibrated (mainly by adapting the bottom roughness) using the measurements for water level, flow velocity, salinity and suspended sediment concentration.
Figure 34 shows a Taylor and Target diagram for the water level at different stations in the simulation h2015 compared to measurements. The stations range from the island Borkum in the North Sea to the weir at Herbrum, which is the upstream boundary of the model. It shows, that the standard deviation, root mean square error, correlation and also the bias are small at all stations along the estuary.

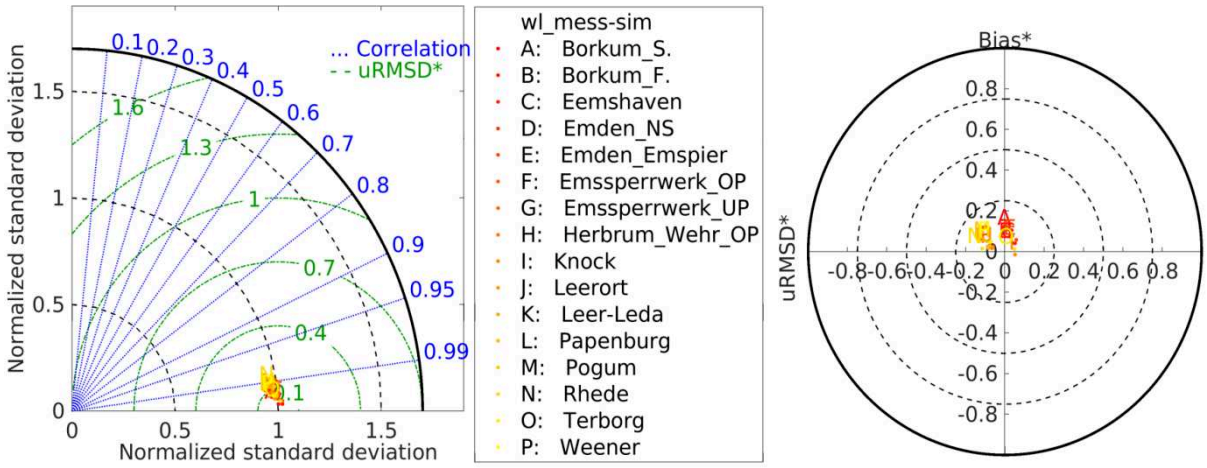

Figure 34: Taylor and Target diagram for the water level at different positions in h2015.

8.3 Method

For the numerical simulations the model UnTRIM was used, as described in chapter 4 and appendix 11.3. Further settings are described in the following.

8.3.1 Grid

For the simulations an unstructured, orthogonal grid with approximately 220.000 elements is used. It contains triangles and quadrangles with an edge length from 10 m (lower Ems river, between Papenburg and Herbrum) up to ~1.000 m (sea boundary). At the side boundaries free slip is defined. The vertical z-layer thickness is 1 m. Some impressions of the h2015 grid are shown in Figure 35.

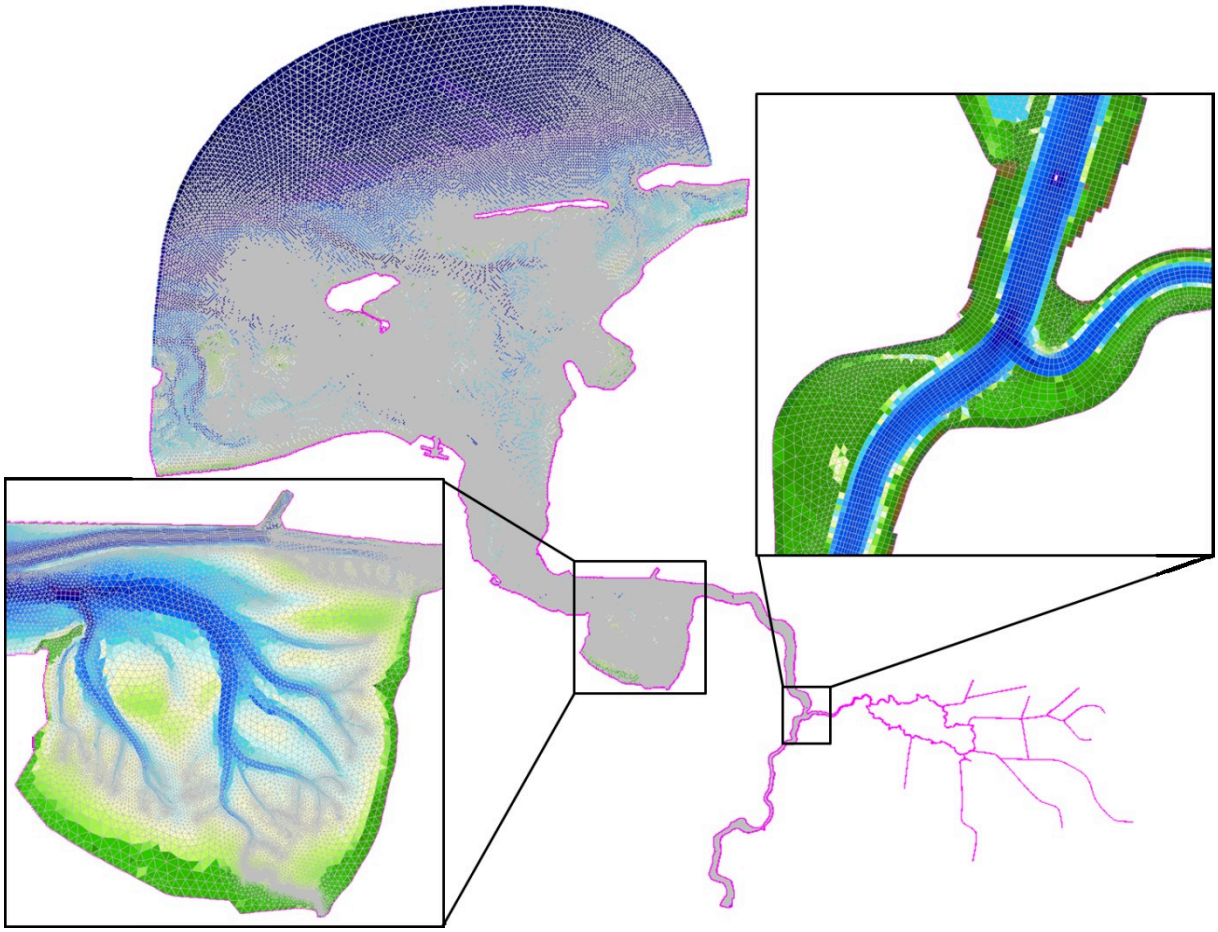

Figure 35: Grid of the h2015 model.

The open sea water level boundary consists of 168 elements. Furthermore, there are inflow boundaries at Westerwoldsche Aa, Herbrum, Leda and Jümme (1-2 elements each). All other boundary edges are no-flow boundaries, shown in pink in Figure 35.

8.3.2 Boundary values and simulation period

When simulating the historic scenarios, all boundary and initial values are taken from h2015, where they are easily accessible and available, but still realistic. This includes boundary values such as the discharge, nodal tide and sea water level as well as initial values such as salt concentration, all derived from measurements and interpolated.

A very important aspect when comparing the simulated results to measurements is the nodal tide which has an effect on the tidal range (see Figure 36) Since the sea boundary condition is taken from 2015 for all scenarios (except for a potential offset due to sea level rise), the phase of the nodal tide should be similar for all scenarios. Therefore the measurements from 1951, which were the earliest with a sufficient quality, could not be chosen. Considering the nodal tide, the decision for the measurement years of 1958, 1981 and 2015 were made.

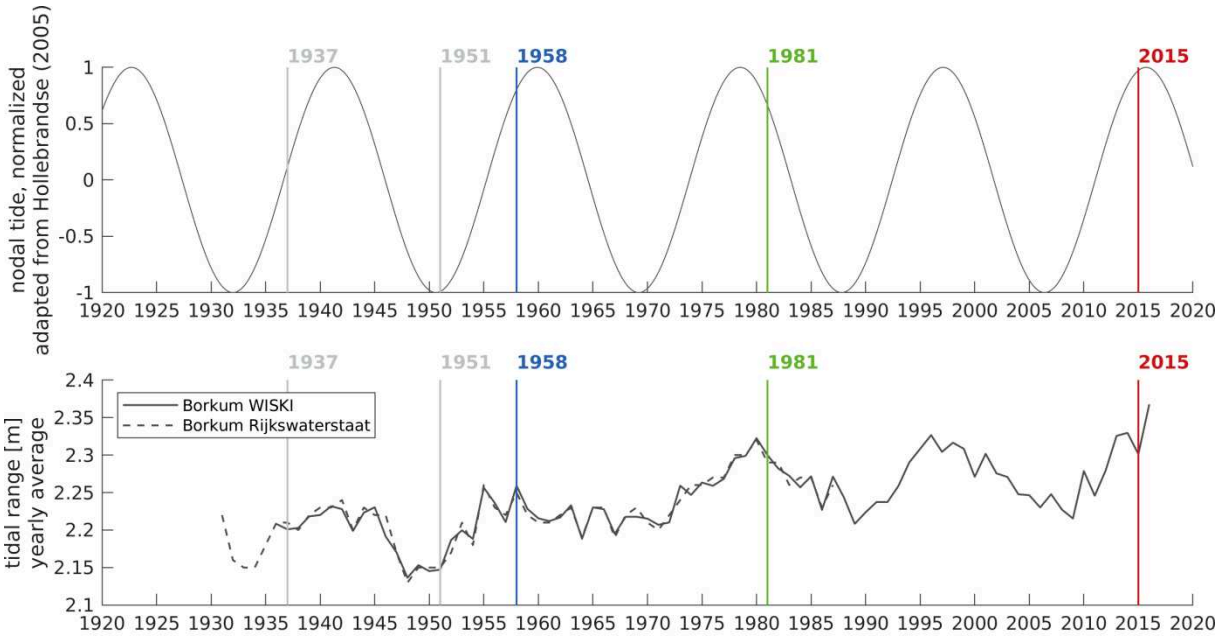

Figure 36: Evaluation of the effect of the nodal tide on the tidal range in the Outer Ems.

A period in summer was chosen, since the development of fluid mud is one of the topics to be discussed and this is visible mainly in the summer period with low river discharges.

According to the discharge data the simulation and analysis periods were chosen. The discharge was supposed to be as constant and similar as possible in all scenarios, primarily in the analysis period, but also in the initialization period. The discharge for different years in June is shown in Figure 37. Therefore, the simulation period was chosen to be 06.06. 8:30 – 29.06. 0:00. The analysis period includes one full spring-neap-cycle (14.06. – 28.06).

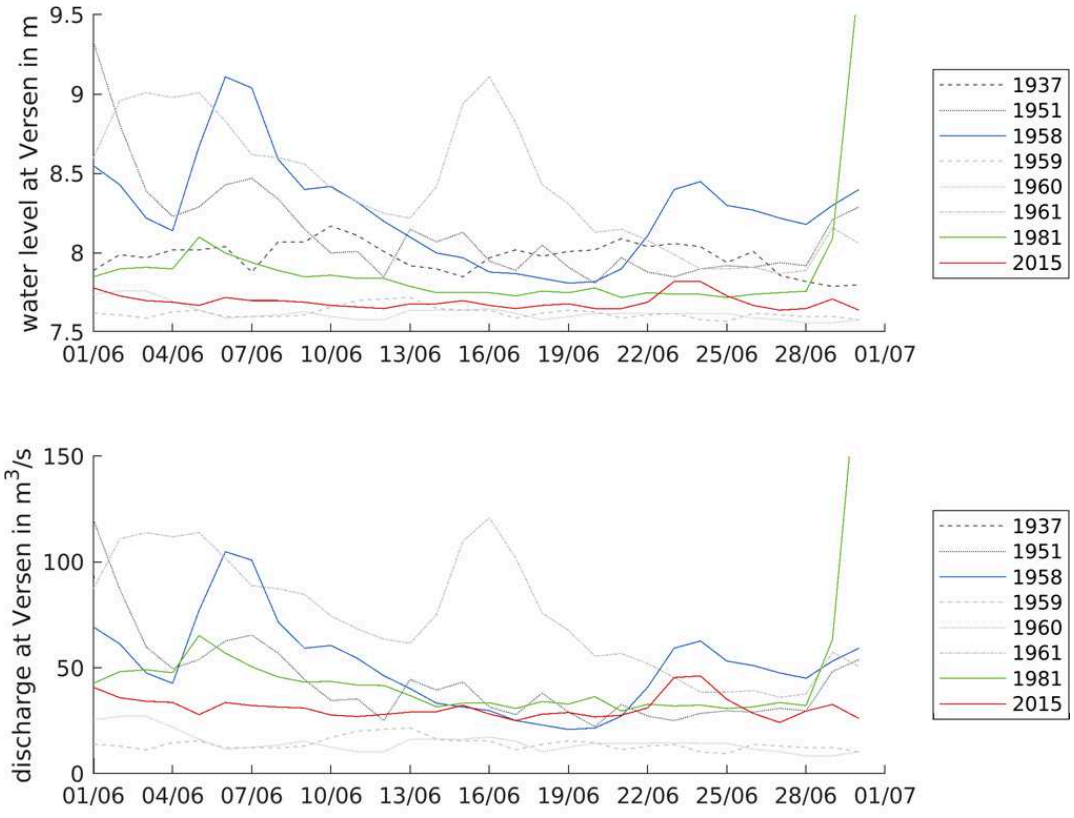

Figure 37: Water level and discharge at Versen for different years in June,

data from (Jahrbuch für die Gewässerkunde des deutschen Reiches 1937; Deutsches Gewässerkundliches Jahrbuch 1951, 1958, 1981, 2015), as well as discharge data from WSA Emden.

As is shown in Figure 37 for the chosen years, the assumption of an identical discharge between June 14th and 28th is quite reasonable. The mean discharge at Versen in the analysis period was 32.6 m^3/s (1981) and 31.2 m^3/s (2015), which is lower than the long term mean discharge for June (1941-2013) of 40.8 m^3/s but reasonably similar and constant in order to allow a comparison. For earlier years no discharge data is available. However, the water level at Versen, also shown in Figure 37, is very similar, allowing the assumption that the discharge has not changed significantly. For scenario h1930s data is available only incompletely and at very few gauges for 1937 and the following years. 1951 was the first year with rather complete measurements of high and low water.

Another important aspect is the sea level. The water level of 2015 at the open sea boundary neglecting sea level rise is not applicable to historic scenarios. In the appendix Figure 76 shows the high and low water at Borkum and Figure 74 the measured yearly average water level at different gauges in the mouth of the estuary, some of them since 1890. These figures show that the assumption of a sea water level from 2015 in a scenario of the 30's/40's includes a relevant error. This has to be kept in mind when evaluating the results. The sea level will be adapted in a separate study (Section 0).

8.3.3 Initial Values

The initial water level is at 0 m NHN (if applicable considering SLR) everywhere in the model region. The starting time of the simulation is chosen so that the boundary water level is close to 0 m NHN in order to prevent a flush wave. The initialization time for the water level is about one day. The initial flow velocity is 0 m/s.

Initial values for the salt concentration are estimated with a distribution based on measurements along the estuary from 32 PSU at the sea boundary to 0.61 PSU at Herbrum. Experiments showed that a few days of simulation are necessary for the salt distribution to be initialized. Thus a period of 8 days is simulated before the analysis period.

8.3.4 Further Settings

Some general model parameters used in all scenarios:

- Calculation time step: 10 seconds
- Latitude for calculation of Coriolis force: 53°N
- Turbulence model: k-ε-Modell (Rodi 1987)
- Turbulent horizontal Viscosity = 0.05 m^2/s
- Bottom roughness: Nikuradse, k_s depending on the scenario (see Table 5).

8.4 Results

In the following, results are shown for each calibration step. First, only the topography is changed, while all other parameters stay the same as in the calibrated h2015 model. After that, the bottom roughness is adapted for the historic scenarios and finally, where necessary, the sea level is changed. The final results are described in section 8.4.4.

8.4.1 Influence of the topography

In a first step, only the topography is modified for the three scenarios. However, the influence on the water level is already obvious, as shown in Figure 38 at the position Leer. The straightened and deepened topography of h2015 leads to a lower low water level, while the high water level stays similar than with historic topographies, causing and increased tidal range. This effect can be observed throughout the estuary. Both, the high water level and low water level, occur earlier in 2015 than in the other scenarios, caused by the straightened channel and higher water depth and the resulting lower geometric roughness. This is a reasonable result in agreement with observations, also observed e.g. by Herrling and Niemeyer (2008b).

In Figure 39 the mean tidal range taken from measurements and from simulations is plotted for all three topographies. As expected, the simulated results for the calibrated scenario h2015 fit rather well. For the two historic scenarios, the qualitative development between simulation and measurement is comparable, but the deviation is still large, since they are not calibrated yet. The tidal range is increased in 2015. The maximum tidal range occurs for h1930s in the outer part of the estuary and decreases upstream. In the scenario h1980s the topography in the lower Ems

upstream of Terborg is lacking sufficient data, thus the location of the maximum tidal range cannot be reproduced only by the topography. However, the influence of the topography alone is remarkable and accounts for a great part of the changes in tidal range.

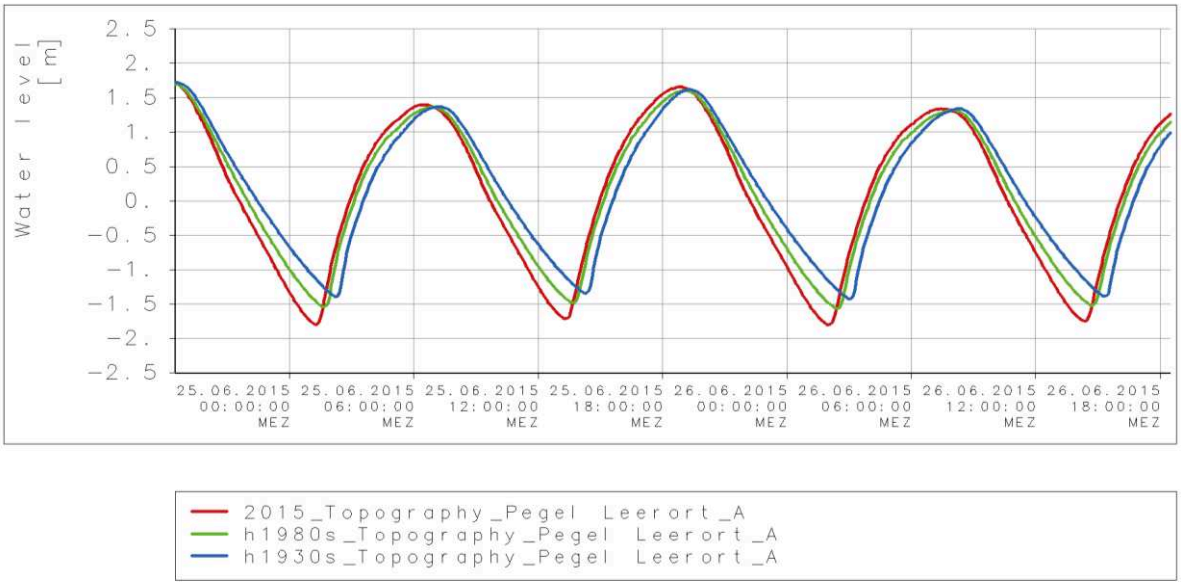

Figure 38: Water level at Leerort for the different topographies of h2015, h1930s and h1980s.

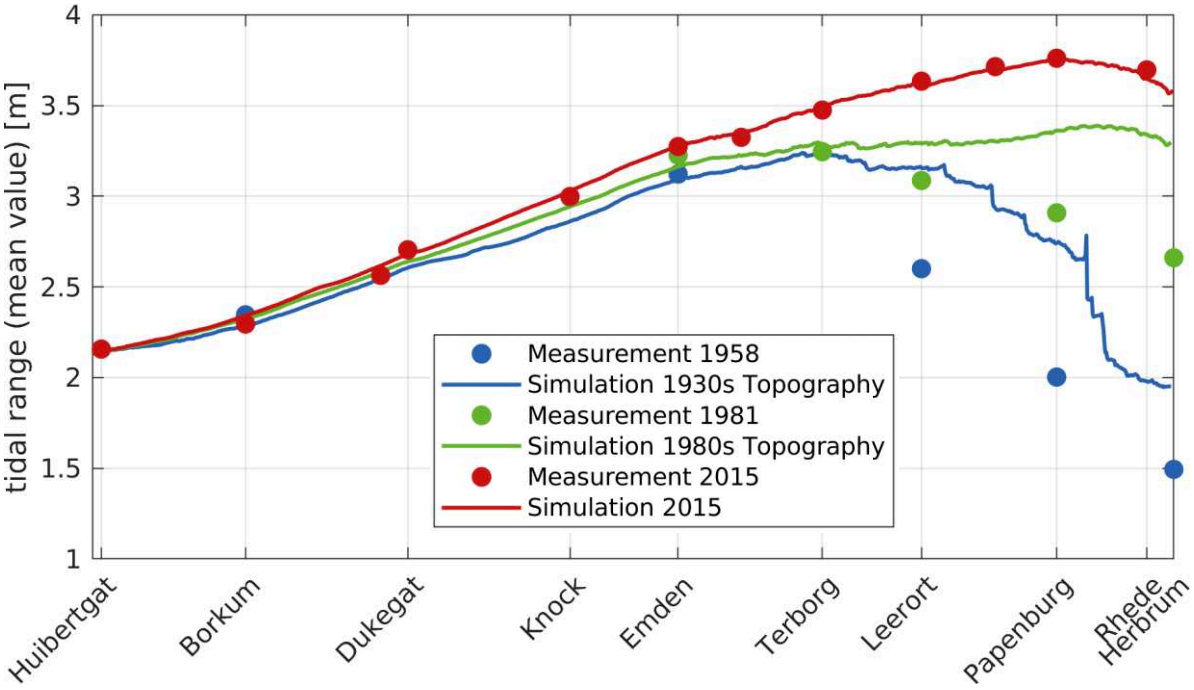

Figure 39: Comparison of tidal range with measurements along the longitudinal profile for different topographies.

8.4.2 Influence of the bottom roughness (fluid mud)

In order to further improve the behavior of the model and investigate the impact of the bottom roughness on the hydrodynamics, the bottom roughness was adjusted for the historic scenarios – first in the Outer Ems and later in the Lower Ems and finally in the Dortmund-Ems-Canal (DEK). This distinction is necessary due to physical features of the area.

The Emden-Dollard region is defined as a transition area, where the roughness decreases linearly between the outer and Lower Ems values.

The order of magnitude of the Nikuradse Factor that should be expected is taken from Herrling and Niemeyer (2008b) and converted from λ into k_s according to LfU (2003). This is documented in Table 4. The final bottom roughness values for all three scenarios are listed in Table 5.

Table 4: Bottom roughness λ by Herrling and Niemeyer (2008b) and converted to k_s according to LfU (2003)

	λ = n	**k_{st} = 1/n**	**k_s in m ≈ 26/(k_{st}^6)**	**k_s in mm**	**Classification**
Outer Ems	0.018	55.56	0.0105	10.5	Medium gravel
	0.026	38.46	0.0954	95.4	Coarse gravel
Dollard	0.012	83.33	0.0009	0.9	Coarse sand
	0.019	52.63	0.0145	14.5	Medium gravel
Lower Ems	0.016	62.50	0.0052	5.2	Fine gravel
	0.026	38.46	0.0954	95.4	Coarse gravel

The four calibration steps concerning bottom roughness shown in the following sections for the scenarios h1930s and h1980s are:

1. Initial set-up with historic topography (as mentioned in section 8.4.1),
2. Calibrated bottom roughness in the Outer Ems (sea boundary until Emden),
3. Calibrated bottom roughness in the Lower Ems (Emden until Papenburg) and
4. Calibrated bottom roughness in the Dortmund-Ems-Canal (Papenburg until Herbrum).

8.4.2.1 Scenario h1930s

The four calibration steps concerning bottom roughness were first applied to the scenario h1930s, shown in Figure 40 for the mean tidal range.

It can be seen that the adaption of bottom roughness in the Outer Ems has an effect on the parameters in the whole estuary, while the bottom roughness in the Lower Ems and DEK mainly affects the hydrodynamics in the area where it is changed.

In order to match the tidal range, a bottom roughness of k_s = 10 mm was selected. The adaption of the sea level, mainly affecting the high and low water levels, will be described in section 0; therefore this is not the final calibration yet.

However, the necessity of these high bottom roughness values (Table 5) in combination with the effect of the topography (Figure 39) confirms the hypothesis by van Maren et al. (2015b), that "the observed tidal amplification is caused by deepening but also by a decrease in bed roughness, with both effects probably being equally important.". This effect is especially visible in the Lower Ems.

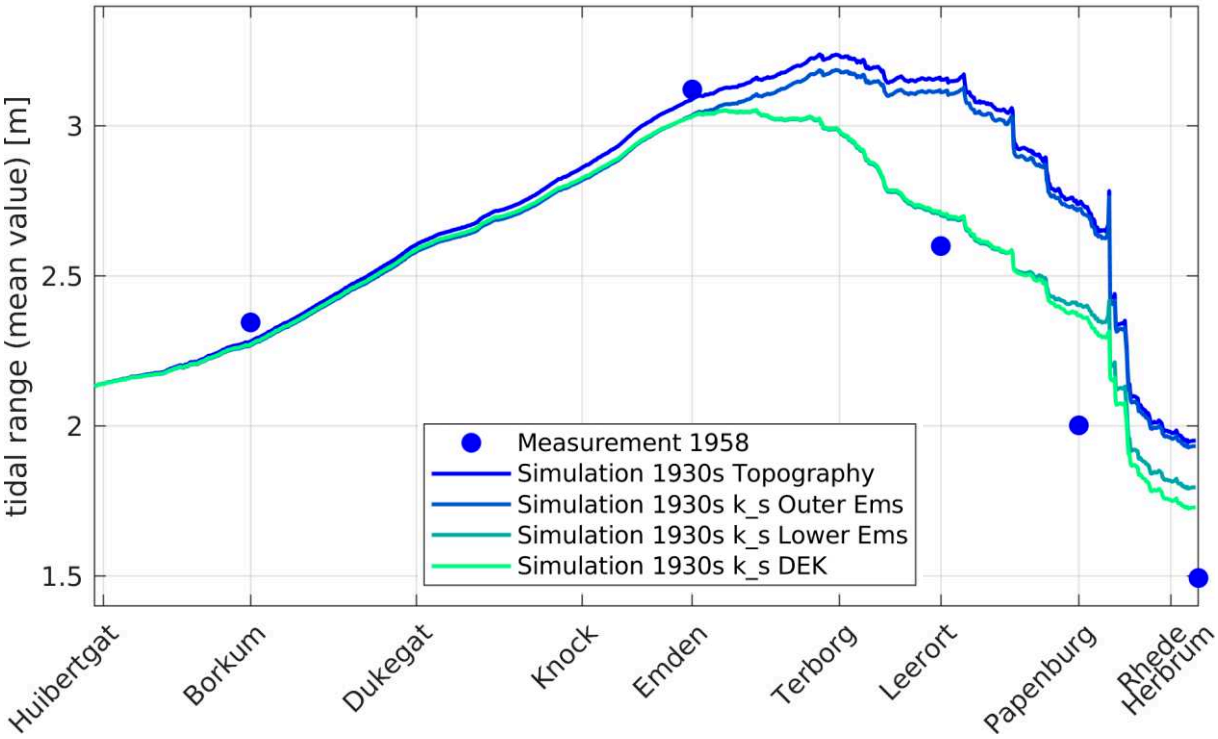

Figure 40: Calibration of bottom roughness in scenario h1930s: mean tidal range.

8.4.2.2 Scenario h1980s

The same calibration of the Outer and Lower Ems bottom roughness is done for scenario h1980s. The tidal range is shown in Figure 41, the mean low water levels in Figure 42 and the flood to ebb duration ratio in Figure 43.

The effect of the changed bottom roughness in the Outer and Lower Ems and DEK is similar to the scenario h1930s. Here, however, the effect on the high water is only minimal, possibly due to a higher water depth compared to h1930s. In h1980s a good agreement with measurements could be achieved only by calibrating the bottom roughness. No sea level change had to be considered, as explained in section 0.

An exceptionally high value for the bottom roughness in the DEK is necessary in this scenario (see Table 5) in order to move the maximum tidal range from the DEK (between Papenburg and

Rhede) to approximately Terborg as seen in measurements. The necessity for this high value may result from a lack of sufficient topographic data in this area. Therefore and since the bottom roughness is such a sensitive calibration parameter especially in these historic simulations, it is much more likely to substitute for aspects not accounted for in the model.

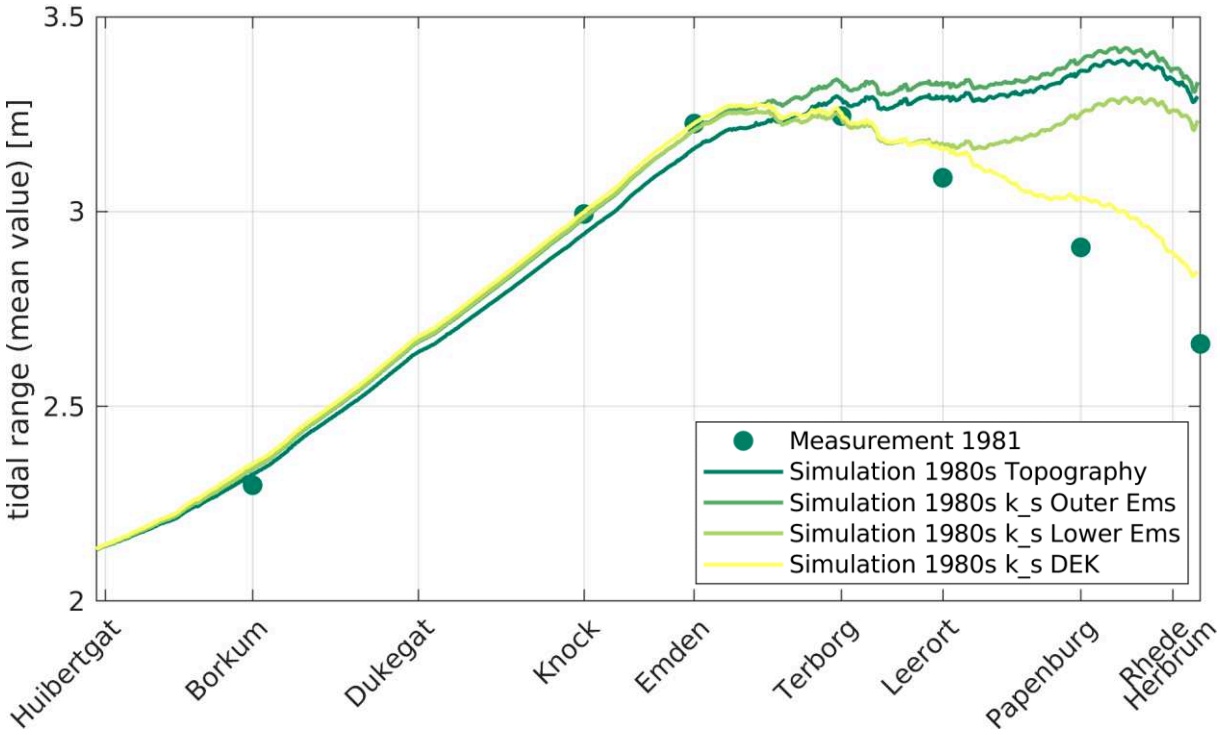

Figure 41: Calibration of bottom roughness in scenario h1980s: mean tidal range.

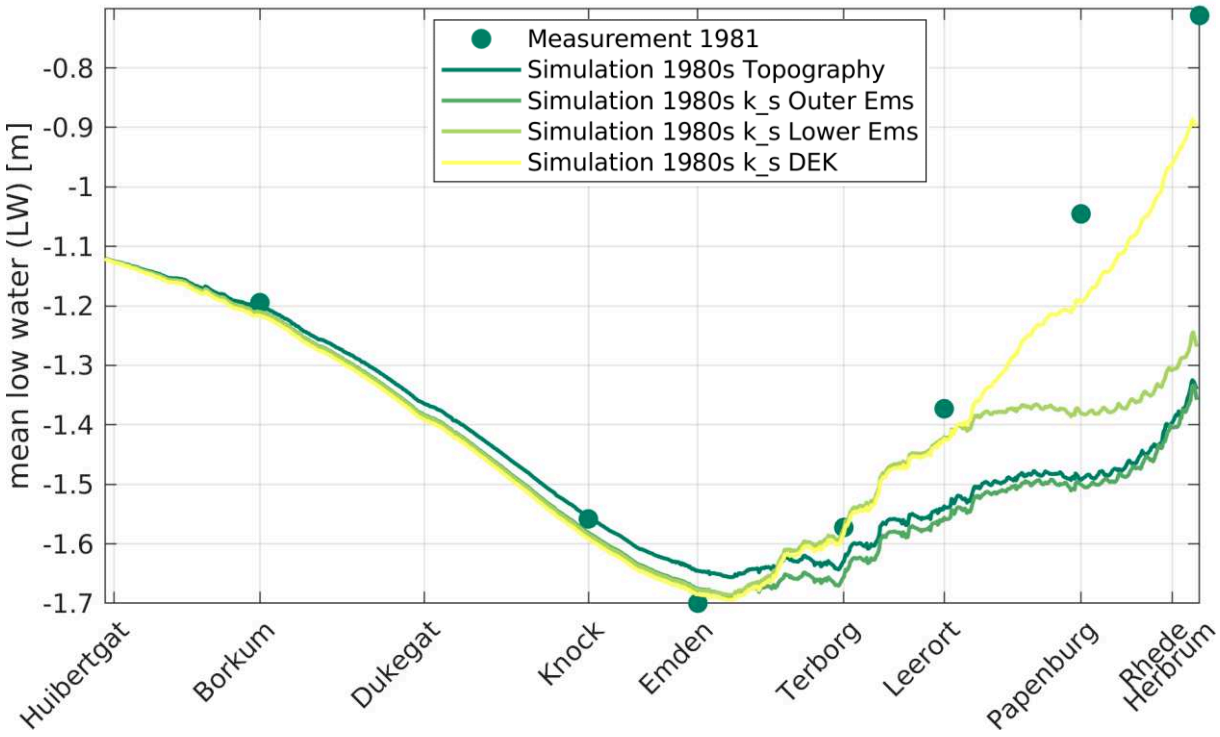

Figure 42: Calibration of bottom roughness in scenario h1981+90+92: mean low water.

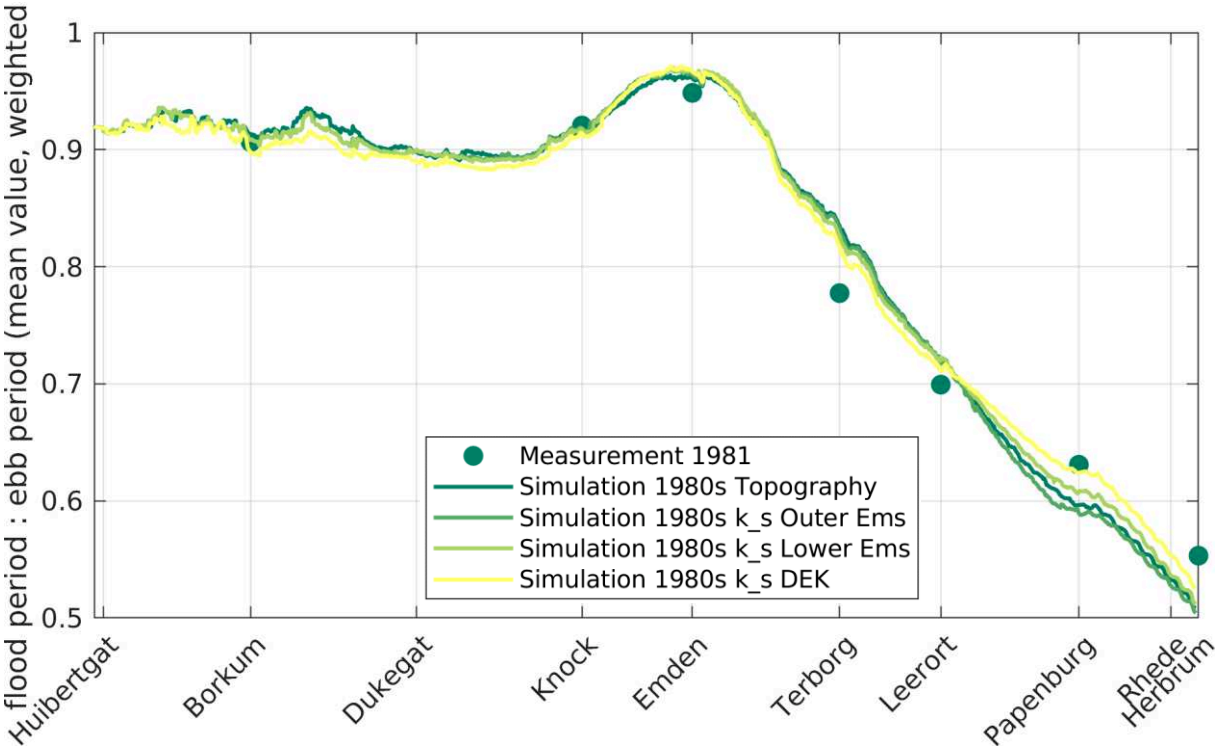

Figure 43: Calibration of bottom roughness in scenario h1980s: mean flood to ebb duration ratio.

Table 5: Calibrated roughness values for Outer and Lower Ems in all three scenarios

k_s [mm]	h2015	h1980s	h1930s
Outer Ems	8	6	10
Dollart (transition area)	8 → 0.126	6 → 1	10
Lower Ems	0.126	1	10
DEK	5	90	10

8.4.3 Influence of the sea level rise

For scenario h1930s it was important to adapt the sea level as compared to 2015, as can be seen in Figure 76. The sea level was lowered by 13 cm along the whole open sea boundary. This value was chosen by the evaluation of literature research and calibration and fits the estimated value taken from Figure 76. The resulting tidal range compared to measurements as well as simulations with the 2015 bottom roughness values and the bottom roughness values calibrated for the h1930s scenario are shown in Figure 44. Only a small improvement can be seen in the tidal range, while, the high and low water levels agree with the measurements much better now (see Figure 45 and Figure 46). The flood to ebb duration ratio (Figure 47) is lower than in measurements, meaning the tidal asymmetry is still too strong in the model.

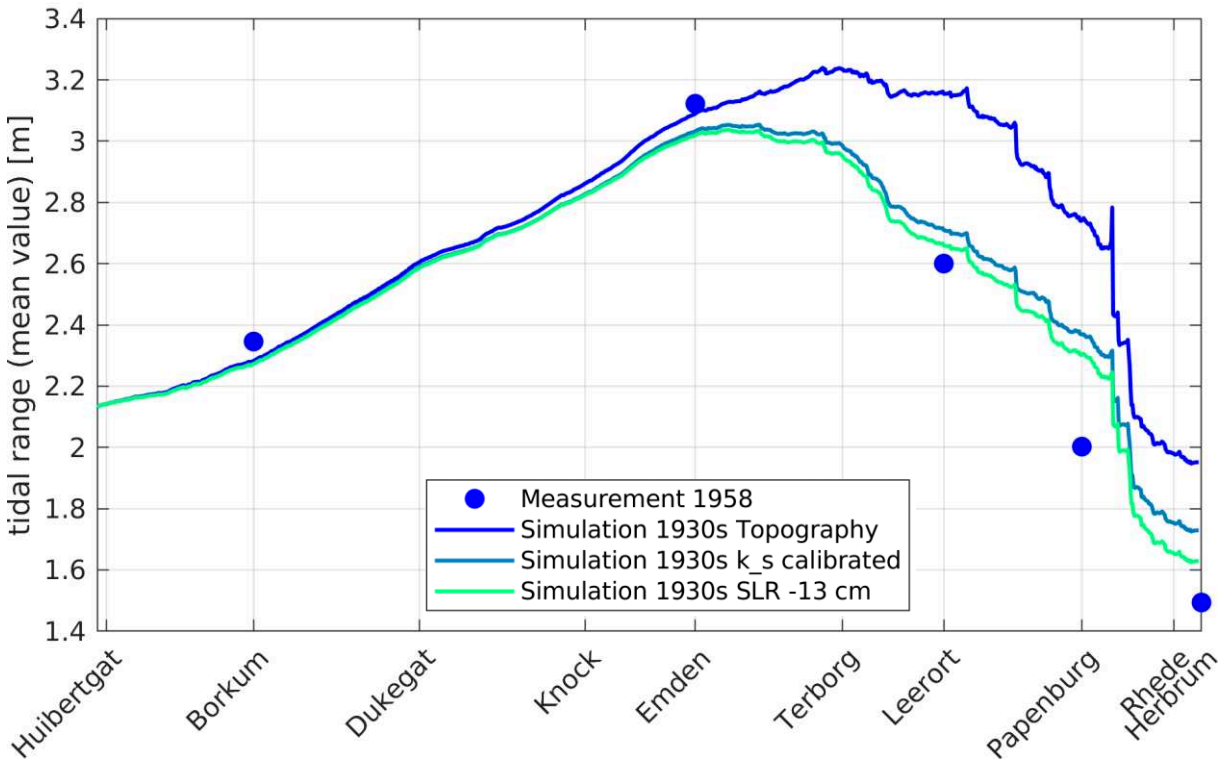

Figure 44: Calibration of scenario h1930s: mean tidal range.

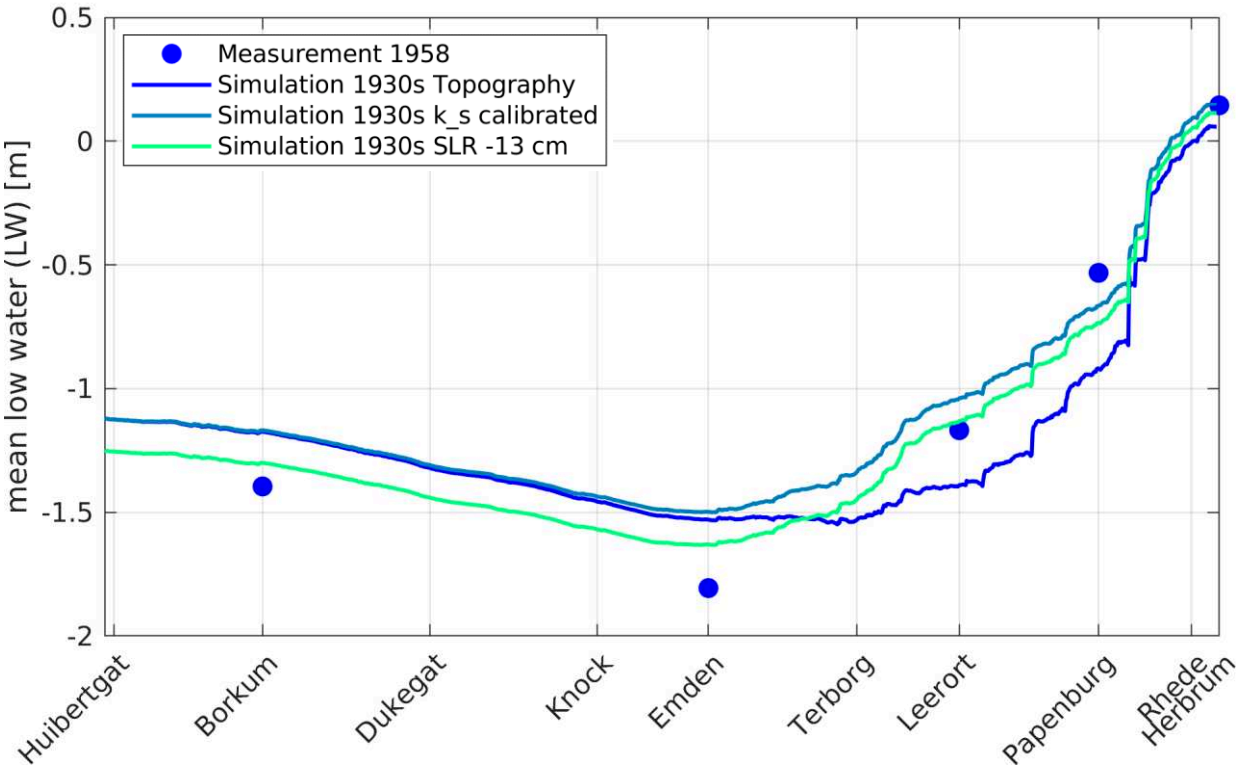

Figure 45: Calibration of scenario h1930s: mean low water level.

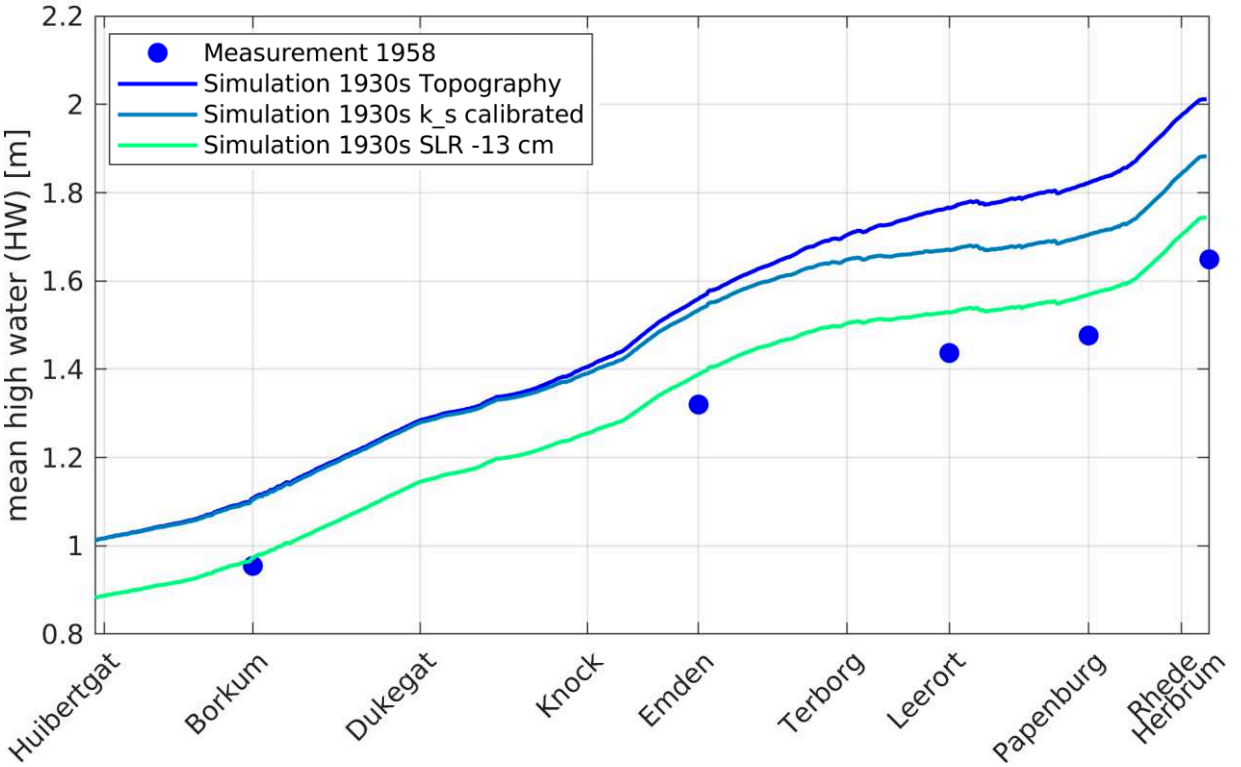

Figure 46: Calibration of scenario h1930s: mean high water level.

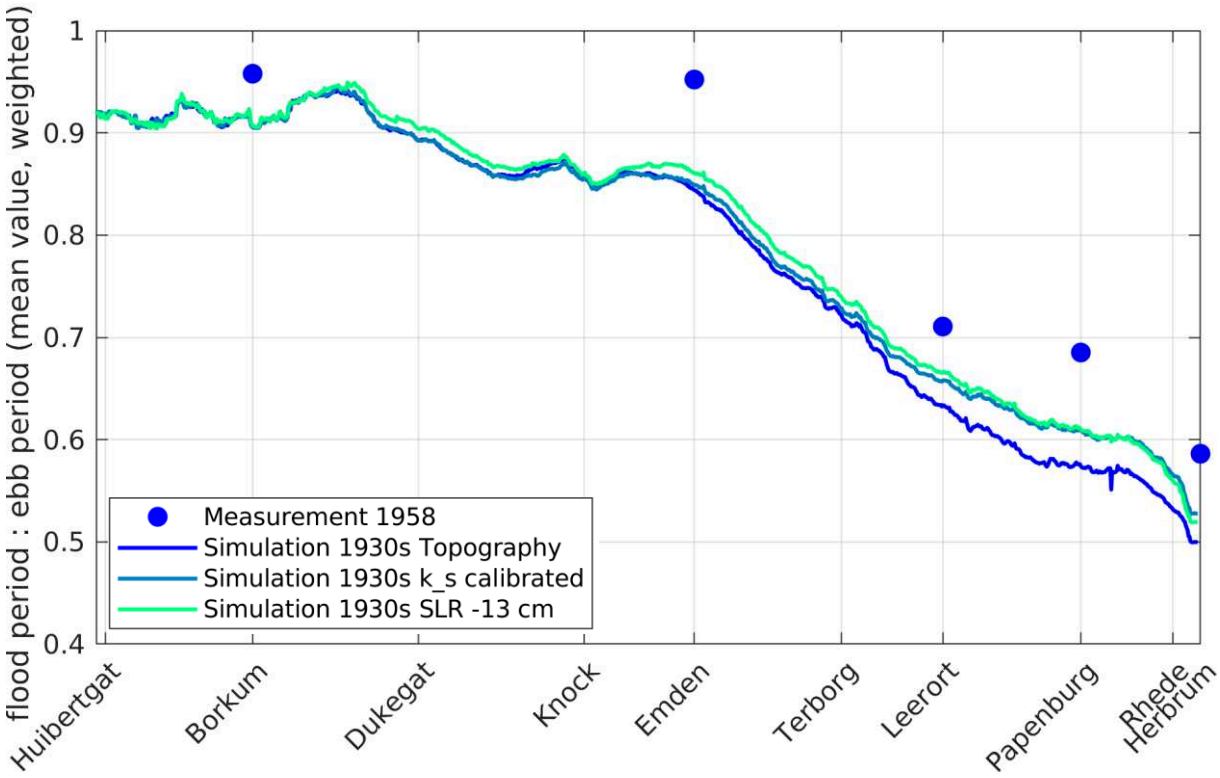

Figure 47: Calibration of scenario h1930s: mean flood to ebb duration ratio.

For h1980s an adaption of the sea level did not improve the results, possibly due to a slightly different nodal tide phase as compared to 2015 (see Figure 36). Since the simulation results already matched the measurements well (see section 8.4.2.2), the sea level was maintained the same as for the 2015 simulations.

8.4.4 Resulting hydrodynamics in historic scenarios

In the previous sections the influence of the main calibration parameters bottom roughness and sea level were described, resulting in scenarios for the three decades compared to measurements of the water level. These set-ups will now be further evaluated and compared with a focus on the water level including the behavior of tidal constituents and flow velocities.

8.4.4.1 Water level

First, the water levels are examined. A time series is shown in Figure 48 for Emden and Papenburg, illustrating the different shapes of tidal waves in the scenarios. In Emden only a small time shift can be seen when comparing the curve for scenario h1930s with the other two. In Papenburg, however, the time and shape of all three scenarios is different. In 2015 the low water is lower and both low and high water occur earlier than in h1980s and h1930s. The high water level is very similar in all three scenarios – in h1930s it is lowered only by the adapted sea level, as can also be seen in Figure 50. This behavior was also observed by Grasso and Le Hir (2019) for the Seine Estuary.

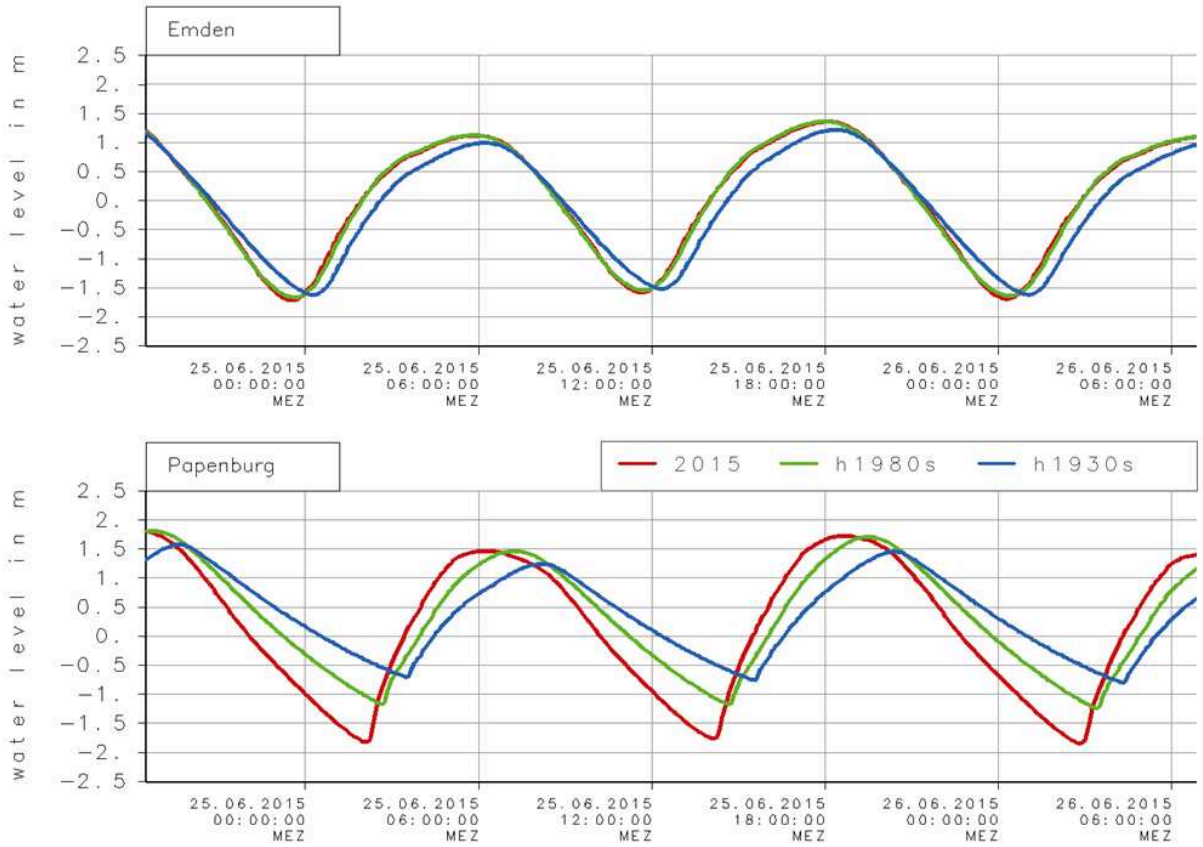

Figure 48: Water level at Emden and Papenburg over time for the three scenarios.

In Figure 49 the before described effect of the low water can be seen. In h1930s a clear minimum low water is observed near Emden, while in 2015 a minimum is much further upstream, approximately near Papenburg.

The high water (Figure 50) is shaped very similarly in all three scenarios; the curve for h1930s is only shifted due to the decreased sea level, as could also be seen in the time series in Figure 48.

Therefore the low water mainly shapes the tidal range along the estuary, as shown in Figure 51.

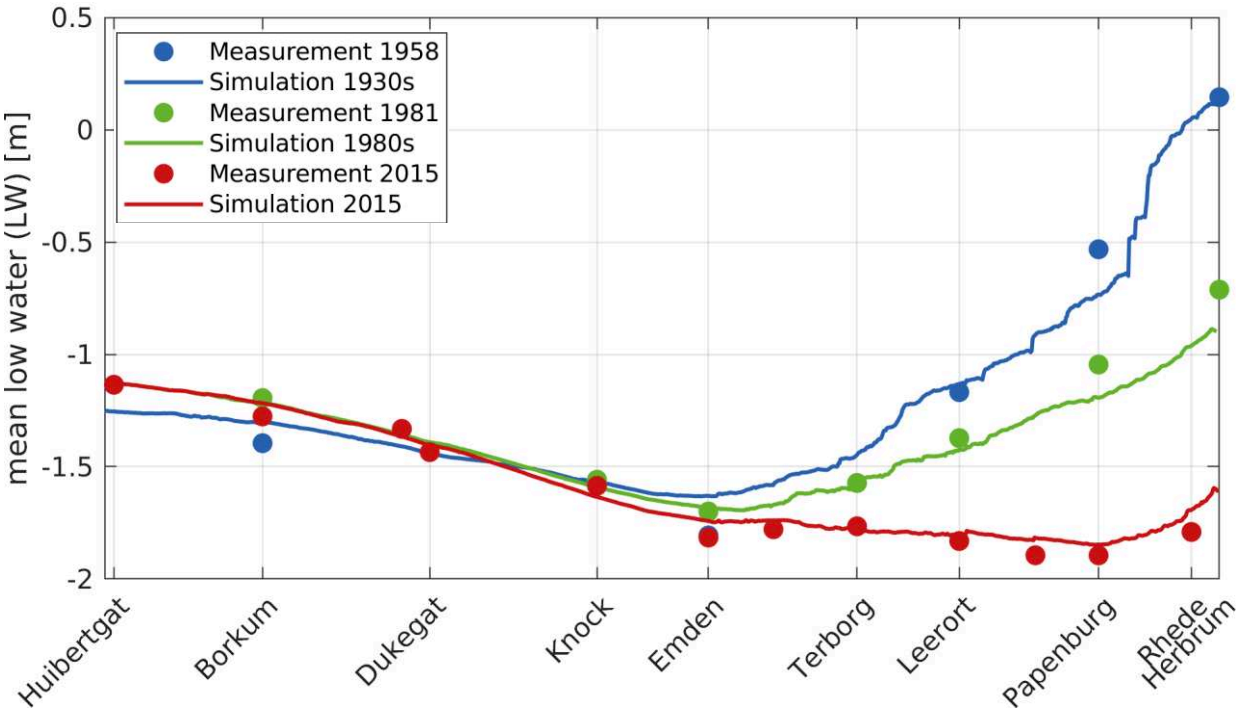

Figure 49: Comparison of mean low water level for all scenarios with measurements.

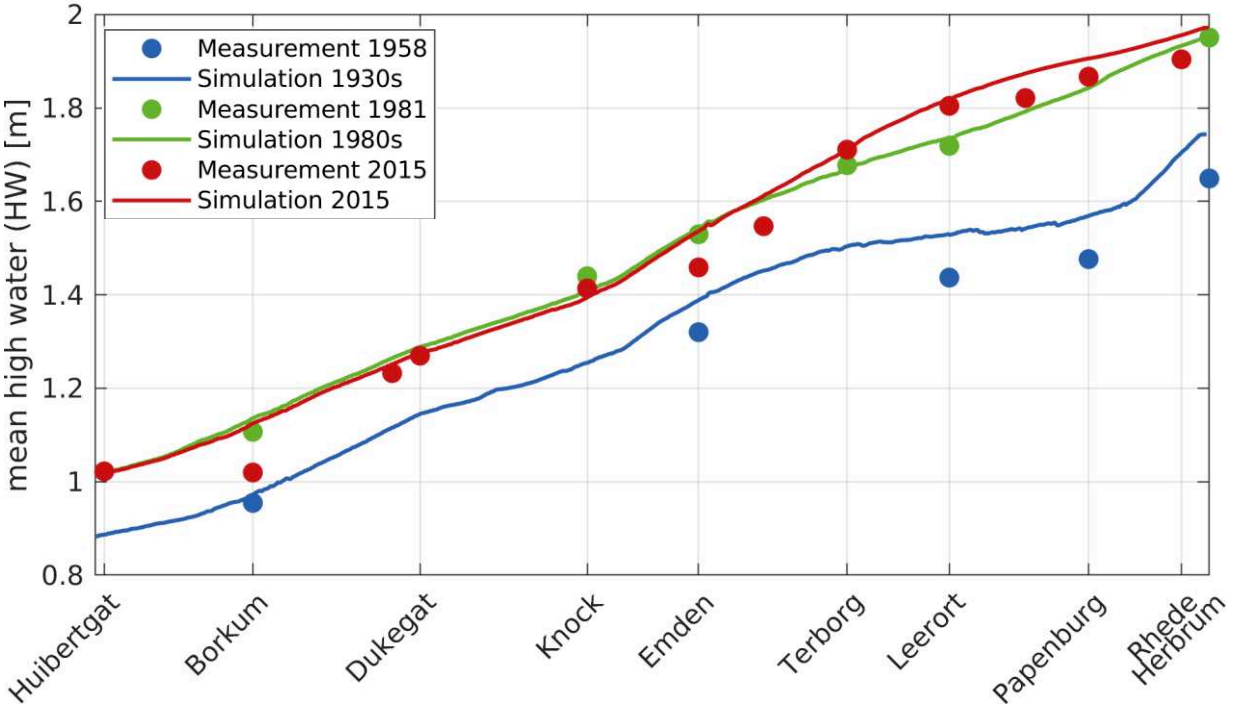

Figure 50: Comparison of mean high water level for all scenarios with measurements.

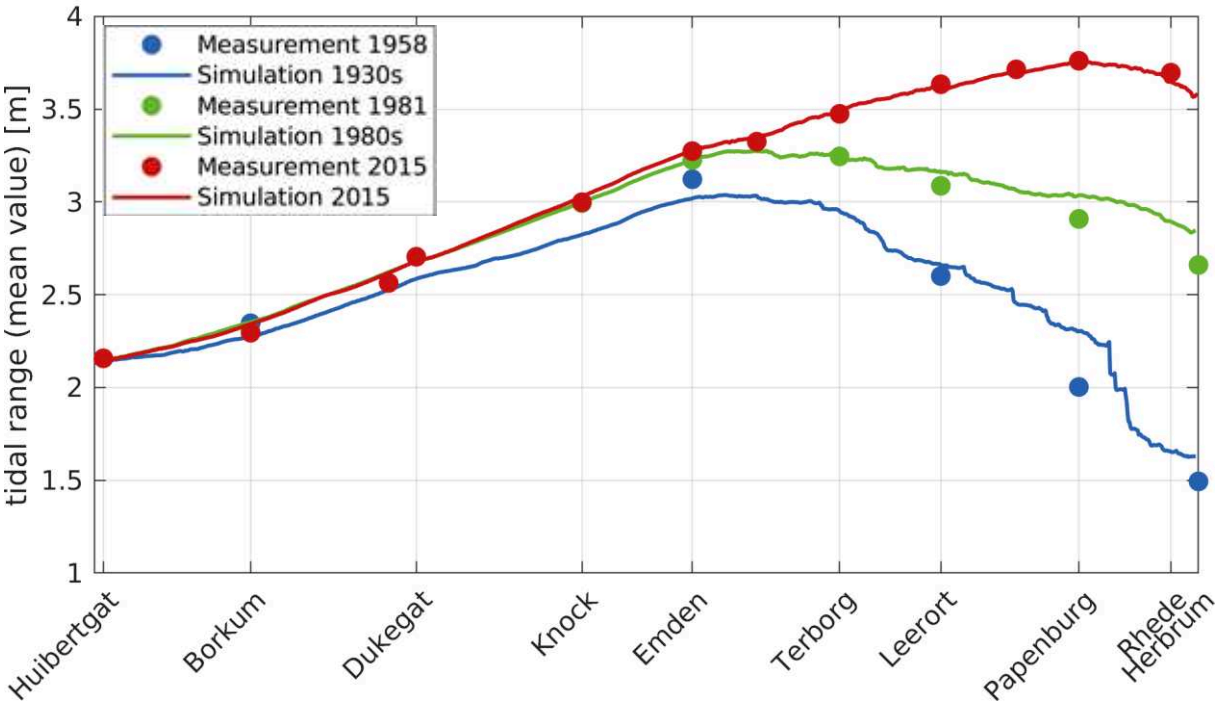

Figure 51: Comparison of mean tidal range for all scenarios with measurements.

In addition, the flood to ebb duration ratio was examined, which is the ratio of the time between high and low water and vice-versa. It is displayed in Figure 52. Values above one imply ebb dominancy, while values below one suggest flood dominancy. For 2015 it shows a strong flood dominancy in the lower Ems, which is still underestimated in the model, and a slight ebb dominancy in the region around Emden. This is in agreement with the measurements, which are also displayed in Figure 52. For the scenarios h1980s and h1930s no ebb dominancy can be seen, neither in the measurements nor in the simulation. However, the flood dominancy in the Lower Ems and DEK is more pronounced in 2015. In the h1930s scenario the flood dominancy is overestimated in the model, according to measurements it has been weaker.

The corresponding flow velocities and flood to ebb current durations will be considered in section 8.4.4.

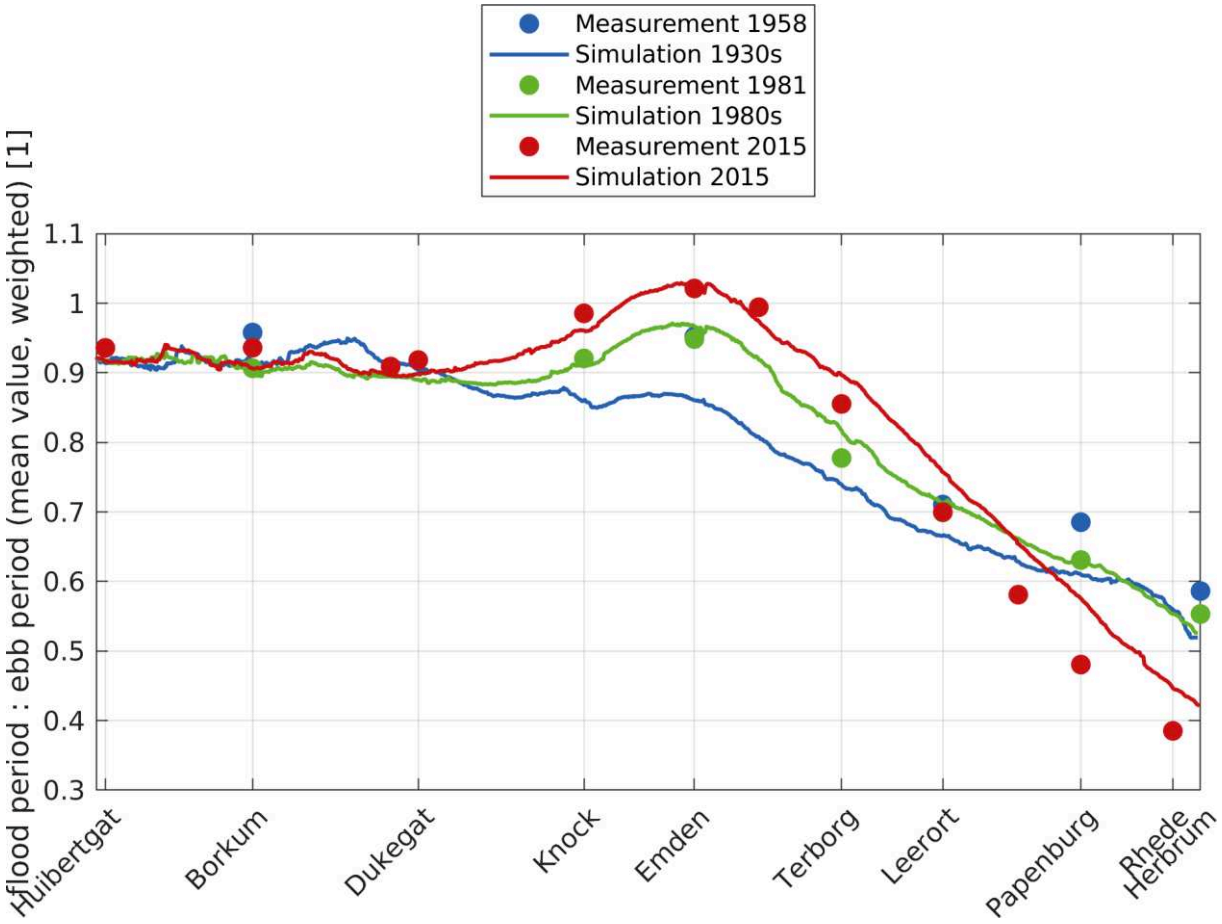

Figure 52: Comparison of flood to ebb duration ratio for all scenarios with measurements.

Figure 53 shows the amplitude and phase of the M2 tide, while Figure 54 contains the same for M4. The phase of the three scenarios along the longitudinal profile can be seen in Figure 55 (M2) and Figure 56 (M4). These two tidal constituents mainly shape the tidal curve in the German Bight. During the development of the Ems Estuary, not only the tidal range but also the amplitudes of the tidal constituents changed. The M2 tide mainly represents the shape of the tidal range. Thus, in scenario h1930s the amplitude rises approximately until Emden and decreases further upstream. In 2015, however, it keeps increasing along the estuary. Furthermore, the amplitude ratio of M4/M2 is much higher in the DEK in h1930s than in 2015, while in h1980s it is even lower than in 2015, which was also observed by van Maren et al. (2015b).
The phase has less variability in h2015 and h1980s than in h1930s, since today the wave travels faster through the estuary. The amplitude and phase of the M4 component shows a similar behavior of a larger variation in amplitude and a smaller variation in phase in h2015. These effects are also observed by Dijkstra et al. (2019b).

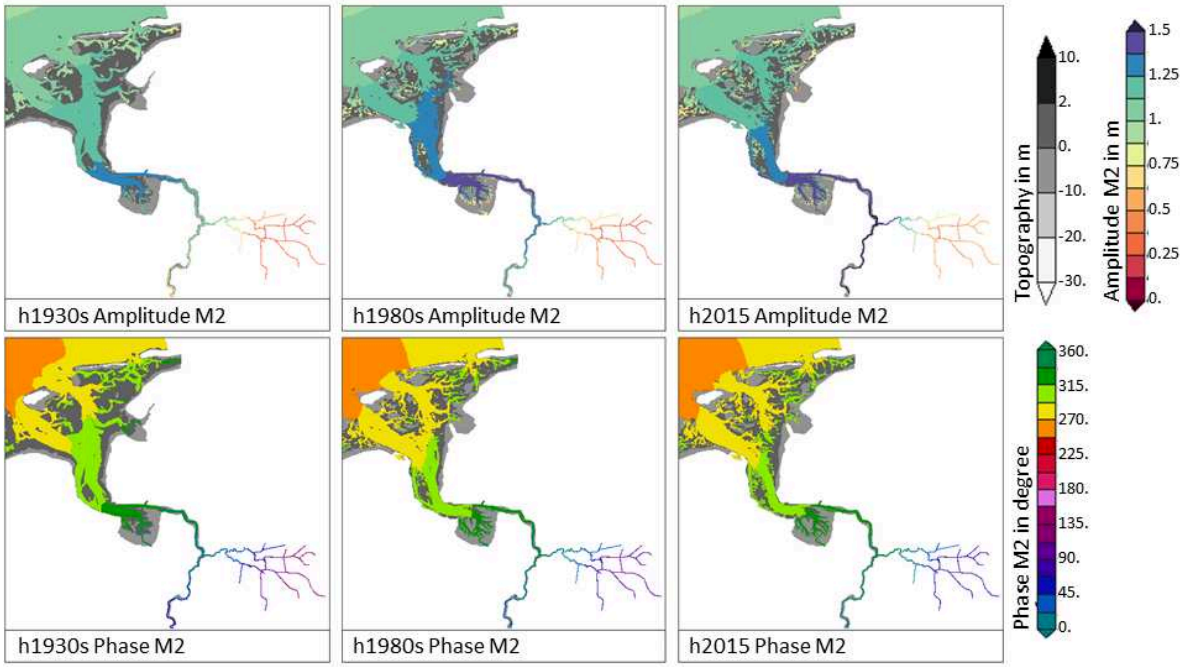

Figure 53: M2 amplitude and phase in all scenarios, top view.

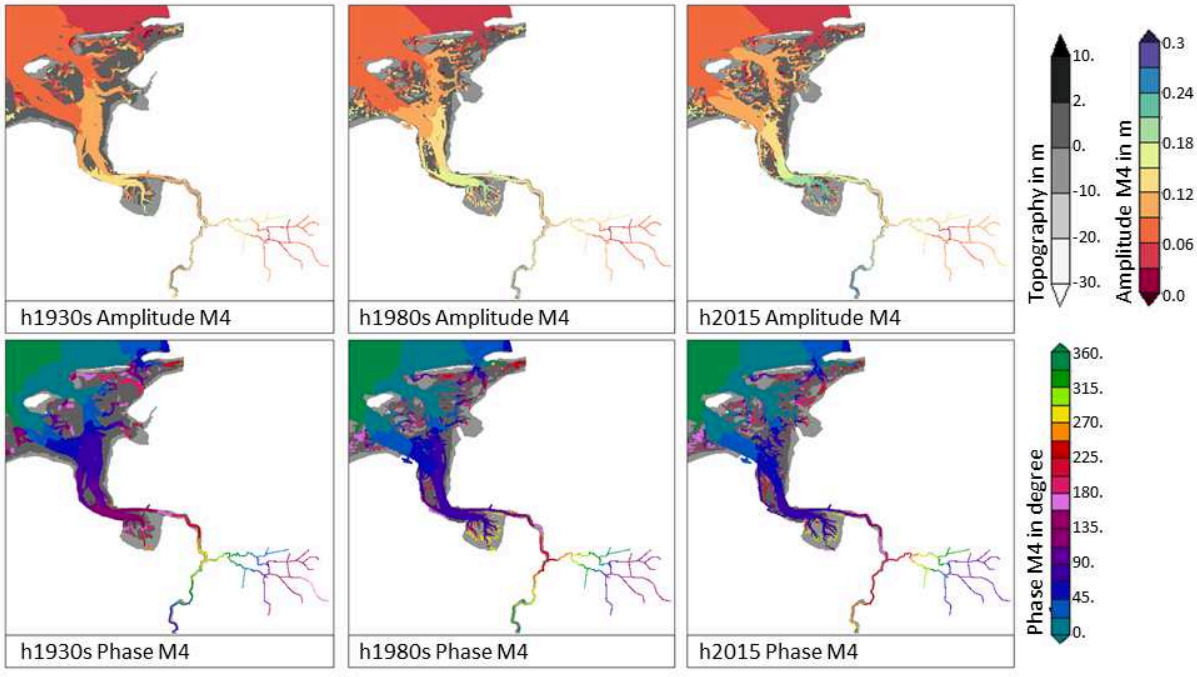

Figure 54: M4 amplitude and phase in all scenarios, top view.

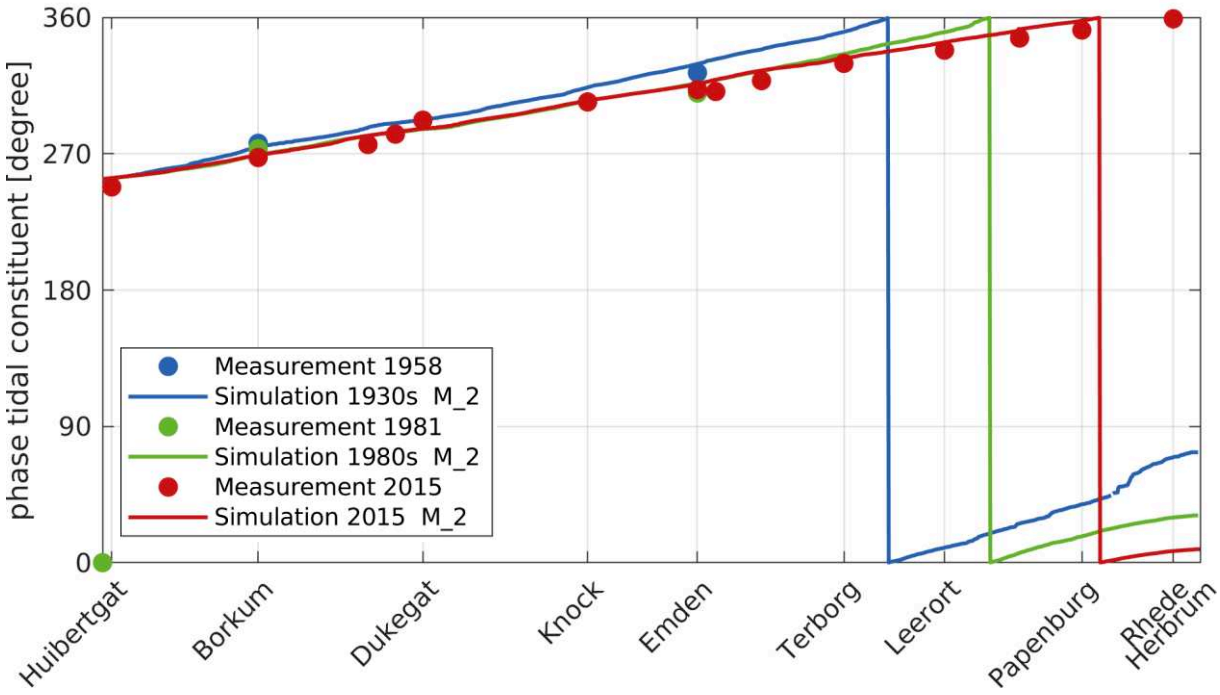

Figure 55: M2 phase for all three scenarios, longitudinal cross-section.

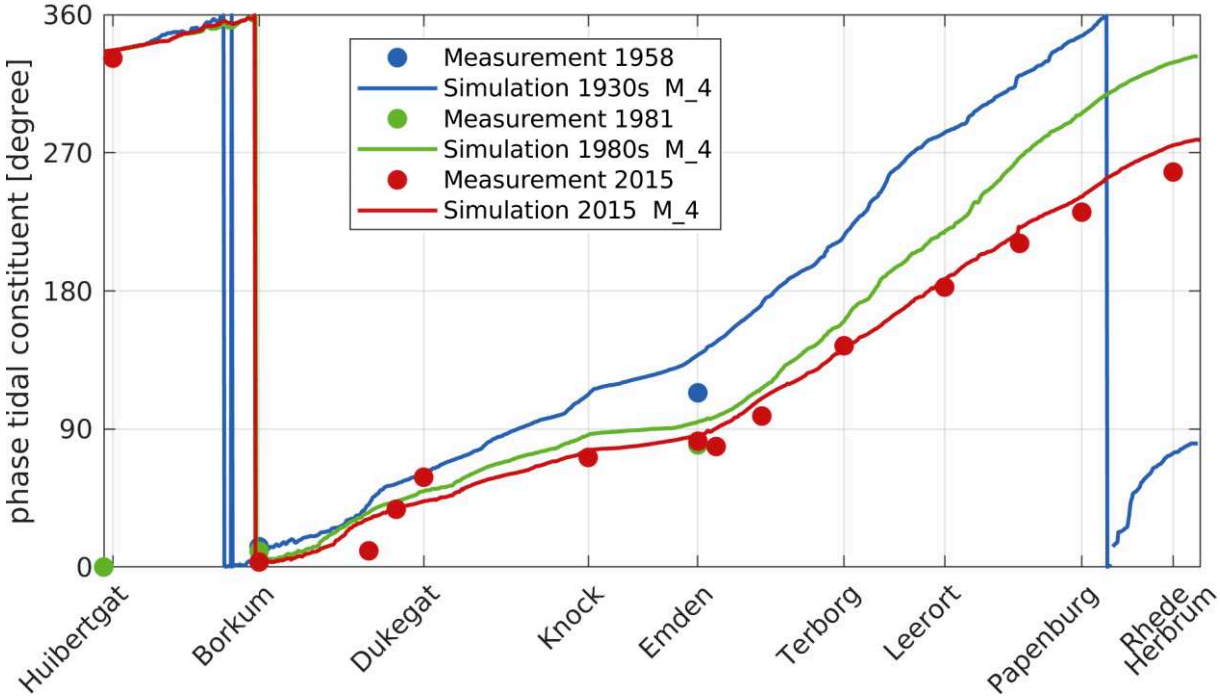

Figure 56: M4 phase for all three scenarios, longitudinal cross-section.

Since the phase in h2015 is very similar all along the Lower Ems and due to the fast propagation of the wave, here the time of high water occurs almost simultaneously between Leerort and Herbrum, which is also represented in measurements. This is shown in Figure 57 and well represented in the model. In the historic scenarios h1930s this effect cannot be observed, while h1980s lies between the two.

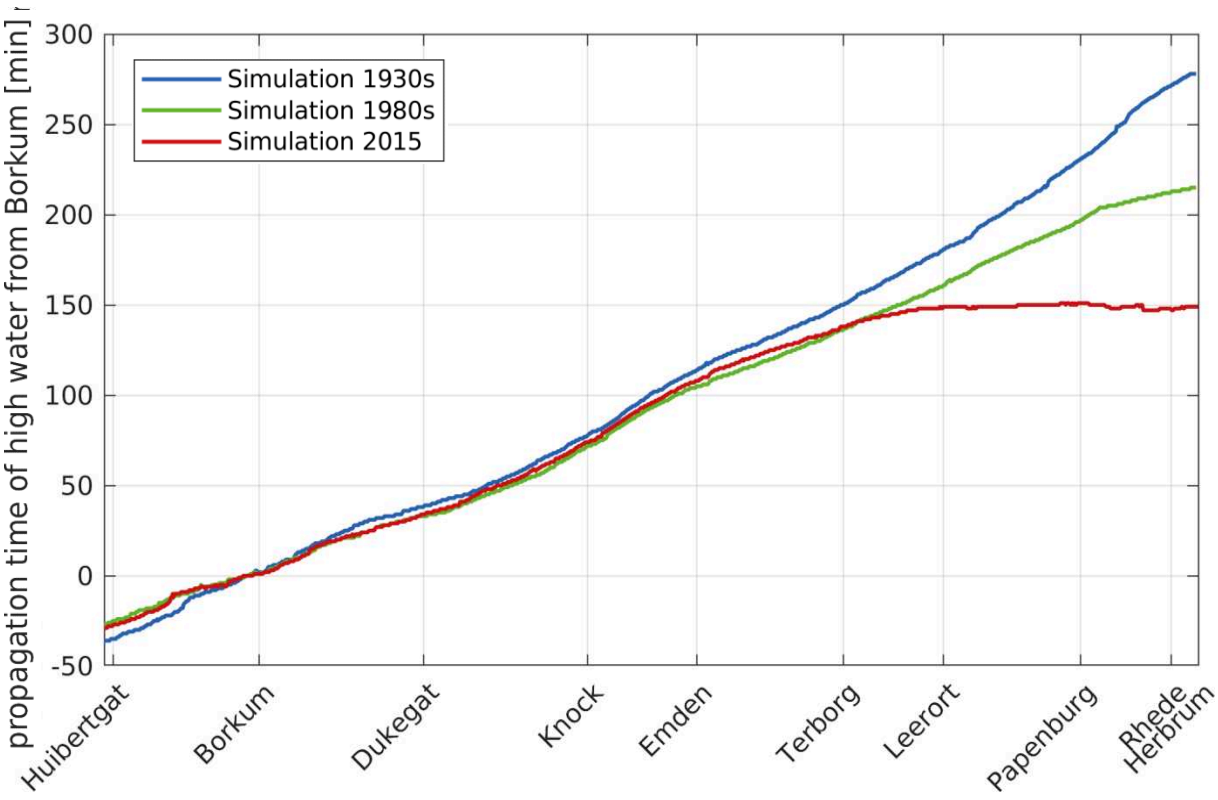

Figure 57: Propagation time of high water for all scenarios

The small difference in the phase shift described by van Maren et al. (2015b) can not quite be reproduced here. Figure 58 shows the phase shift between M4 and M2 for all three scenarios. Especially in the Lower Ems the difference between h1930s and h2015 is up to 45°, which seems to be a larger difference than found by van Maren et al. (2015b). This also explains the effect of the short propagation time of high water described above, due to the formation of a plateau at high water, as described in BAW (2012).

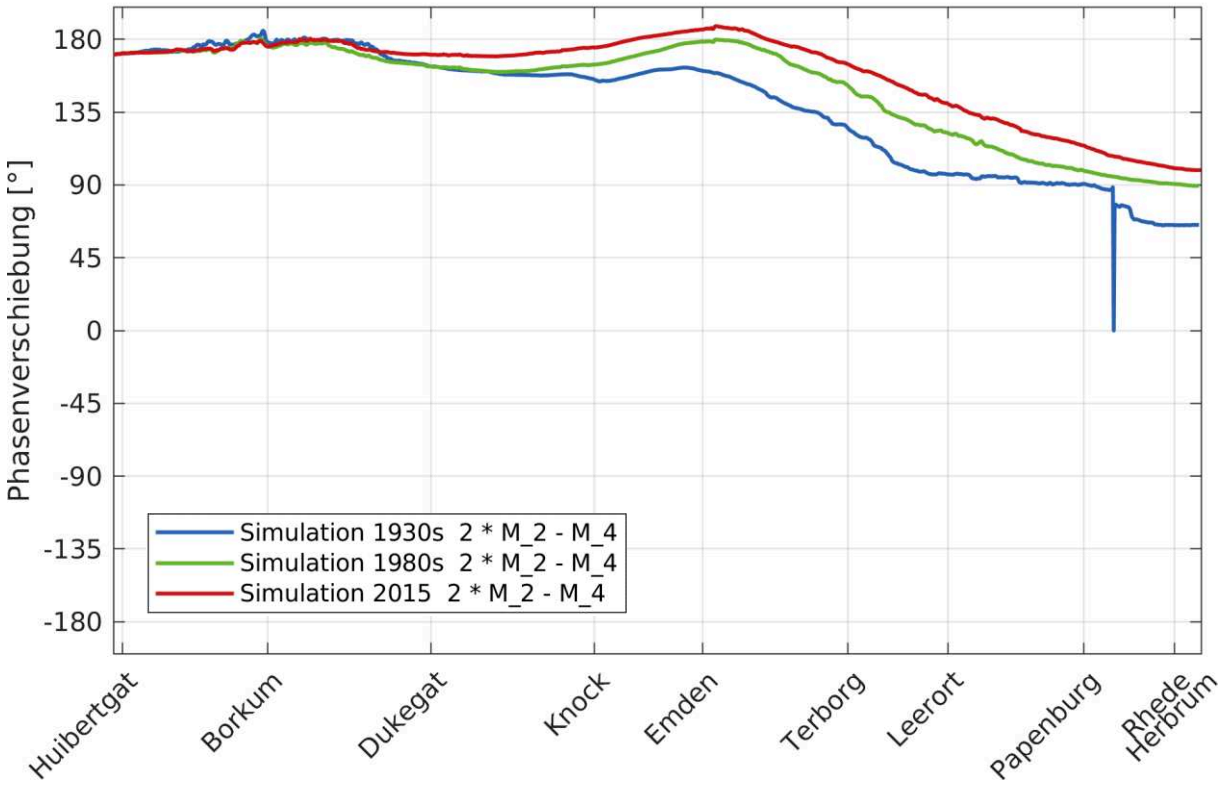

Figure 58: Phase shift of the amplitude between M2 and M4 in all scenarios

8.4.4.2 Flow velocities

Similar to the water level, the flow velocity at Emden does not differ much in the three scenarios, while in Papenburg the differences can be seen well. Figure 59 shows time series at the two locations. In Papenburg, the flow velocities during ebb current have increased until 2015 and even more increased during flood current. Interesting to see is that the ebb current velocity between h1980s and h1930s is very similar, while the flood current velocity has increased from h1930s to h1980s. This can also be seen in the tidal analyses of flood and ebb current velocities in the following figures.

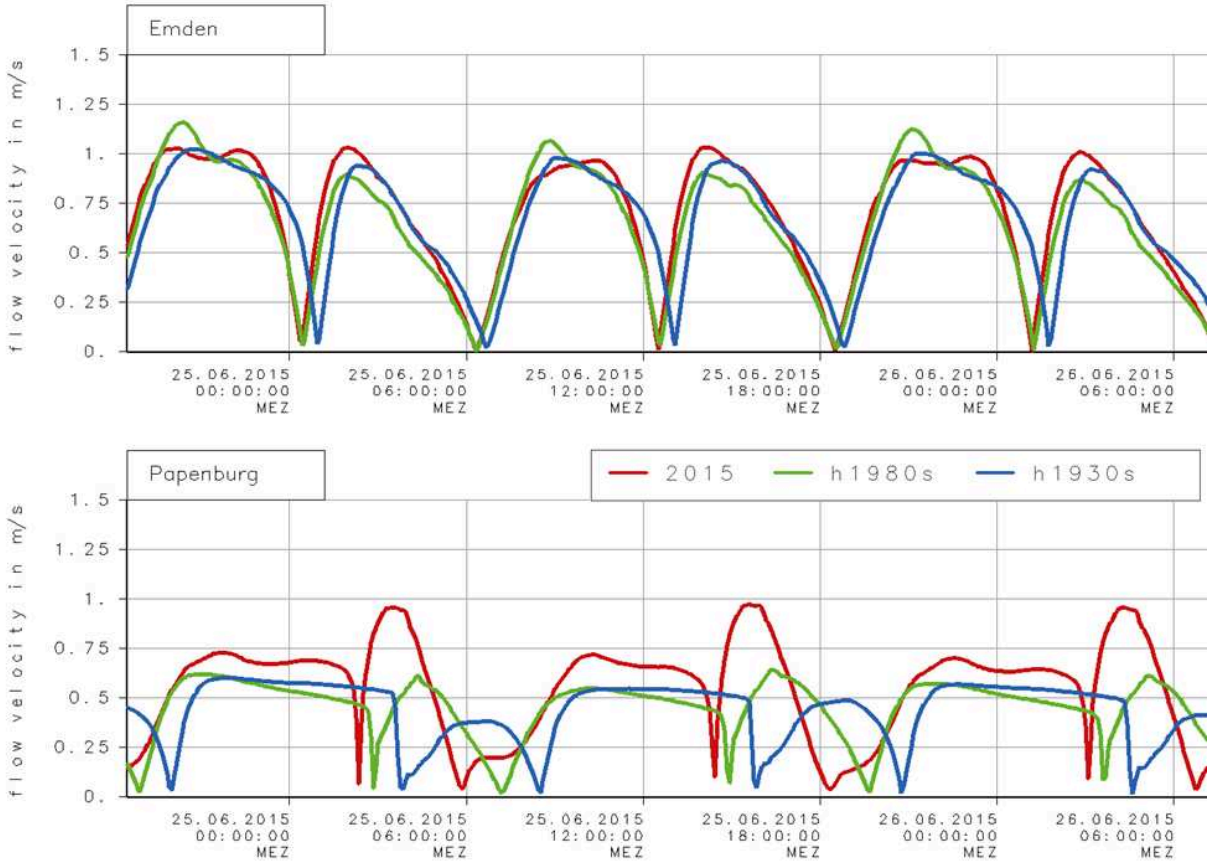

Figure 59: Flow velocity at Emden and Papenburg over time for the three scenarios.

The mean flow velocities do not differ very much between the scenarios. The maximum velocities, however, increase for h2015, especially in the DEK, as shown in Figure 60. The velocities for h2015 agree with measurements. For the historic scenarios, unfortunately no sufficient measurements of the flow velocities are available.

Dijkstra et al. (2019b) found, that while the M2 velocities stayed similar, the M4 velocities increased significantly. This could also be observed in this study.

When analyzing the flood to ebb current duration in Figure 61, it can be seen that the tidal asymmetry has varied in time. For values below one the ebb current duration is longer than the flood current duration and for values higher than one vice-versa. Thus, values below one imply a flood dominancy (higher flood current velocities) and higher than one an ebb dominancy. In h1930s the Ems Estuary is flood dominated everywhere, except for very small region around Dukegat. In 2015, however, a more pronounced ebb dominancy can be seen between Borkum and Emden, nevertheless the flood dominancy in the Lower Ems and DEK is stronger than in h1930s. This increase of flood dominancy upstream of Leerort is also described by Krebs and Weilbeer (2008). A discussion of this parameter can be found in section 8.4.5.

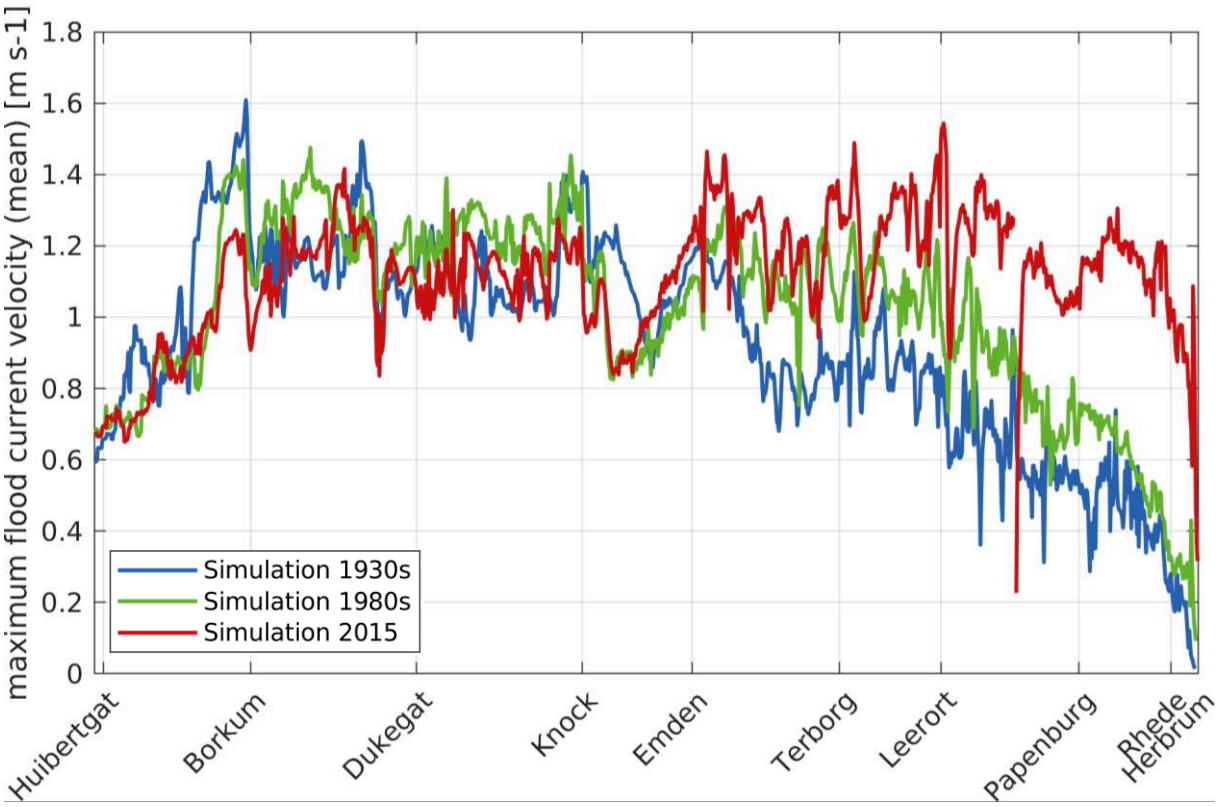

Figure 60: Comparison of maximum flood current velocity for all scenarios.

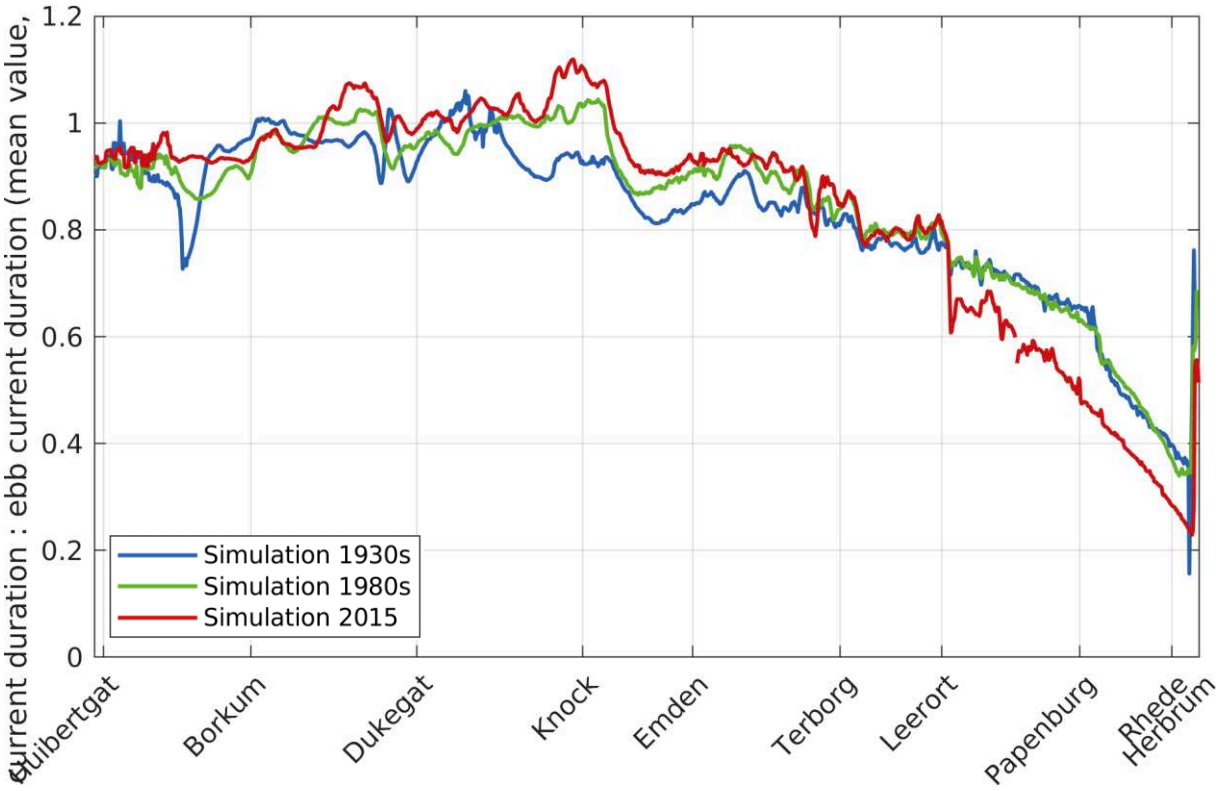

Figure 61: Comparison of flood to ebb current duration for all scenarios.

8.4.4.3 Tidal prism

Within the project, a master thesis was written by Sarah Koch, examining tidal prisms of German estuaries, including historic states of the Ems Estuary. Most analyses in this thesis were done with measurements and in slightly different time slots than the simulations described before. However, the development can be seen. Figure 62 shows the results, including the empirically determined relations between tidal prism and inlet area by O'Brien (1931, 1969) and Dieckmann (1989). In addition to the tidal prisms of the Ems Estuary, further measurements on the pacific coast of the USA (x) by O'Brien (1931) and in the German Bight (*) by Giese (1972) are included.

More details on tidal prisms, the comparison of different calculation procedures and with other German estuaries are described by Sarah Koch (2018).

With respect to the historic development of the Ems Estuary these calculations show that the cross sectional area of the inlet at Dukegat became smaller from 1950 until 2010, even though the fairway was deepened. This results from the shore areas, which became more shallow and narrow, thus decreasing the inlet area. Even though the inlet cross sectional area became smaller, the tidal range increased. This can be explained by shifted tidal phase durations and higher velocities. This development contradicts the empirical correlations of O'Brien (1931) and Dieckmann (1989), who found the lines marked in Figure 62 for estuaries in equilibrium. Furthermore, their correlations are based on the assumption, that flood and ebb phase are of the same length. As described before, this assumption cannot be made for the Ems Estuary and thus the development may be different. However, it leads to the assumption that the tidal prism of the Ems Estuary did not develop naturally and is not in equilibrium.

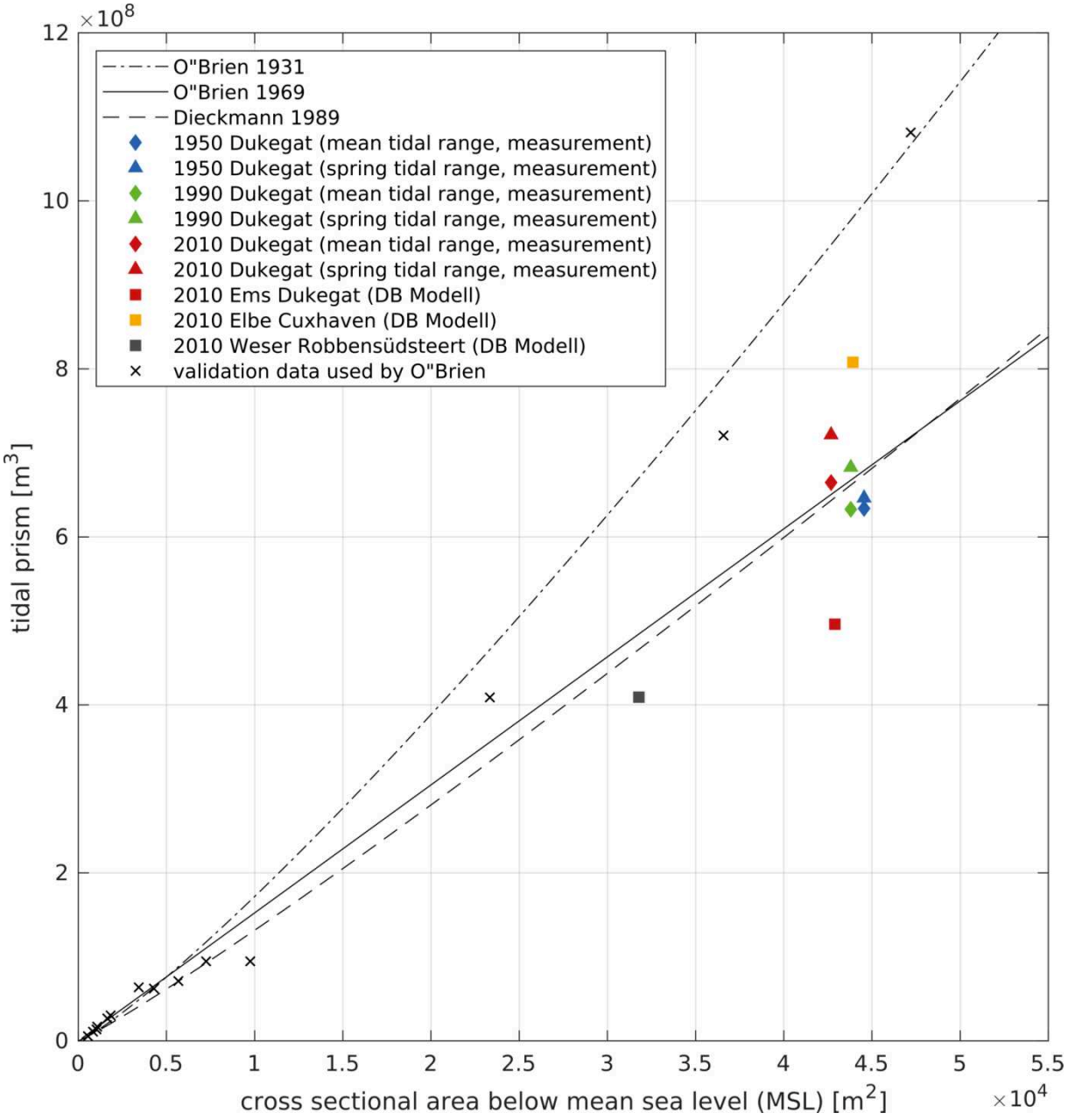

Figure 62: Relation between tidal prisms and inlet cross section areas for different states and locations of the Ems Estuary, figure adapted from Sarah Koch (2018), using data from (O'Brien 1931, 1969; Dieckmann 1989; Giese 1972).

8.4.5 Discussion

In the previous sections the results from the numerical models were described, with focus on the hydrodynamics. Sediment transport in the Ems Estuary, today and in historic scenarios, has e.g. been investigated by van Maren et al. (2015a) and Dijkstra et al. (2019b). Therefore, in this study, the focus lies on a detailed, three-dimensional investigation of the historic development of the hydrodynamics. It can be shown, that the hydrodynamic parameters are able to give indications for sediment transport and mud formation in the estuary.

Interesting to see is the time needed by the high water to propagate from a reference point, in this case Borkum, to any other point in the estuary. This is shown in Figure 57. In h1930s, the high water travels almost linearly in time along the estuary. In 2015, on the other hand, the travel time is constant (about 150 minutes) in a large part of the Lower Ems, upstream of Leerort. This means, that high water occurs at almost the same time between Leerort and Rhede, as explained in section 8.4.4.1. This effect well represents former studies and measurements (BAW 2012). Also the increased tidal amplification mentioned by van Maren et al. (2015b) could be reproduced.

As mentioned in the results, the hydrodynamic overall behavior agrees well with other literature, e.g. Dijkstra et al. (2019b) and Herrling and Niemeyer (2008a).
However, in the case of the flood and ebb current duration, the project HARBASINS by Herrling and Niemeyer (2008a) obtains different results than this study, while other hydrodynamic parameters agree reasonably. In HARBASINS, the flood current duration between Leerort and Herbrum increases form 1937 until 2010, while in this study it decreases (the ebb current duration behaves accordingly). This means, that according to Herrling and Niemeyer (2008a) the flood dominancy in the Lower Ems decreases, while in this study it increases[2]. The explanation by Gerald Herrling (personal communication, 12.09.2018 and 10.01.2019) for the decreased flood dominancy in the Lower Ems is, that due to the high hydraulic roughness in the historic scenario, not much flood current reaches the end of the Estuary and the influence of the freshwater inflow dominates. However, in the present study, the flood current reached the upper boundary of the Estuary in all scenarios. Therefore, the phase shift of the tidal constituents and the increased asymmetry of the tidal wave lead to an increased flood dominancy upstream of Leerort in 2015.

Possible reasons for these different results might be the implementation and use of the turbulent horizontal viscosity in the two models and the modelling of two (HARBASINS) or three (this project) dimensions. Further research is necessary, in order to thoroughly compare the models and results with all available measurement data.

Requirements for a regime shift towards a mud importing system were concluded by van Rijn and Grasmeijer (2018). They could be reproduced in this study:

[2] Flood dominancy here means, that the flood current velocities are higher than the ebb current velocities. Thus, the flood current duration is shorter than the ebb current duration.

1. *Bed after deepening becomes muddy*
   After deepening the topography (1930s until 2015), less roughness is needed in the model to meet the water levels, especially between Emden and Leerort. This is, according to measurements, the region in the Ems Estuary with increased occurrence of fluid mud. By the decreased bottom roughness, the behavior of the system with fluid mud is approximated.
2. *Water depth at mouth is changed to a value larger than the "equilibrium" water depth*
   The relationship between water depth at the mouth and inlet cross section (or discharge) was evaluated using the tidal prism described in section 8.4.4.3. The development leads to the conclusion that the Ems Estuary is not in equilibrium, but that the cross sectional area at the inlet is too small for the tidal prism going through it.
3. *River discharge is relatively low and without large extreme values*
   Especially in summer months, the freshwater discharge of the Ems River is rather low. In combination with the asymmetric tide, river flushing is prevented.
4. *Velocity asymmetry is relatively large*
   Especially in the Lower Ems, the asymmetry of flood and ebb current velocity is large in 2015, as shown in Figure 59. In the historic scenarios, the asymmetry is much smaller.
5. *Long periods with low velocities around neap (large variation of tidal range over neap-spring cycle)*
   Low velocities around neap compared to spring can be observed in the model and in measurements, as well as a large variation of tidal range over a spring-neap cycle, as shown in Figure 77 in Appendix 12.3.3. However, the lowest tidal range in 2015 (from measurements) is still higher than any tidal range in 1958. The variation of the tidal range over neap-spring cycles is larger in 2015 than in 1958.

According to the comparison with the indicators for a regime shift by van Rijn and Grasmeijer (2018), the models can reproduce the states before, during and after the regime shift of the Ems Estuary. The resulting tidal prisms lead to the conclusion, that the alteration of the cross sections result not only in short- but also in long-term developments of the hydrodynamics.

The morphodynamics, however, are not modelled here. They are also significantly influenced by the dredging, which is described in detail in appendix 12.2 . The formation of fluid mud can, therefore, not solely be traced back to the deepening of the fairway. The handling of dredging and the dredged material is also of great importance. The transition from dumping sites on land to dumping sites within the estuary is assumed to also have made the siltation possible by increasing the availability of sediment (Krebs and Weilbeer 2008). Thus, a possible sixth requirement, which could be added to the list above, is the availability of sediment, in addition to the transport capacity created by the hydrodynamics.

8.5 Summary and intermediate conclusion

In this part of the project MudEstuary, historic scenarios of the Ems Estuary were examined. Three topographies were assembled, containing measurements from several years each, especially the earlier ones. The scenarios simulate the 1930s, the 1980s and 2015. Boundary and initial values were taken from 2015, due to a lack of data in the early years. However, they were tested for plausibility in order to match the measurement data used for calibration.

During the study of the historic scenarios, the influence of the topography, bottom roughness and sea level were examined separately. It could be shown that the topography alone has a significant influence on the hydrodynamics in the Ems Estuary. The bottom roughness is especially important in order to reproduce the characteristic behavior in the Lower Ems. The bottom roughness is here especially connected with the formation of fluid mud, since this leads to an extremely decreased roughness effect.

After calibrating the three scenarios with respect to water levels, further hydrodynamic parameters were examined. It can be seen that the velocities in the Lower Ems have increased, especially during flood current, amplifying the flood dominancy, which supports the import of sediment into the estuary. This effect is especially visible during low discharge events, which were considered here.

In future studies sediment dynamics should be included in the simulations and the influence of the turbulent horizontal viscosity should be investigated and calibrated. With the extended modeling procedure described in part II, the conditions leading to the formation of fluid mud can be further investigated and understood.

In order to be able to compare the development of the Ems Estuary with other estuaries, the tidal prism, either according to O'Brien (1931) or calculated from current velocities as described e.g. by Jonge (1992), is a possible parameter. For example historic and current states of the Weser or Elbe Estuaries could be analyzed in a similar way as described in section 8.4.4.3, investigating and comparing the development. Furthermore, the criteria by van Rijn and Grasmeijer (2018) can be used for evaluating the state of an estuary, complemented by the criterion of availability of (fine) sediment.

IV Conclusion

9 Summary

While the focus in "MudEstuary_A" was on experimental laboratory tests on the turbulent behavior of granular suspensions, the focus of "MudEstuary_B" was on the further development of a numerical 3D model and an application to the Ems estuary. The basis of these investigations is a so called “continuous model approach”, which allows a borderless transition from free turbulence to rheological, laminar flow by means of an effective viscosity.

For an efficient conception of the further development of the 3D model, a numerical 1DV model was additionally developed jointly by the project partners in the first year of the project. The continuous model approach was implemented in this model, so that first results could be calculated. Advantages and disadvantages of the approach became immediately visible due to the short computing times of the 1D model. Hence, an efficient optimization could take place before the approach was transferred to the 3D model.

The mathematical descriptions of the most important physical processes for modelling fluid mud dynamics included the following components:

- effective viscosity consisting of a rheological viscosity and a turbulent viscosity
- flocculation and hindered settling
- adapted boundary conditions and new interpretation of k-ω-turbulence model

These components were implemented in a numerical 3D model in the second work package. The focus was especially on the implementation of the new simulation methods associated with the continuous model approach. For this purpose, modules were newly created or adapted in FORTRAN. The extended continuous model approach combined turbulence and mud rheology. An application could be confirmed with adapted boundary conditions and a new interpretation of k-ω-turbulence model. A successful application of the 3D model could be realized for the numerical simulation of the laboratory model and a schematic estuary model. The results were documented in part II of this report.

However, the extended continuous model approach results in new challenges. The new simulation methods require high computing power. Moreover, the formation and dynamics of fluid mud are an interplay of various processes and effects, for which there are still great sensitivities and insufficient validation data. For these reasons an application to a nature system such as the Ems estuary was currently not expedient.

The third work package (part III of this report) focused on identifying the causes of siltation in estuaries. For this purpose numerical simulations with a classical hydrodynamic 3D model were carried out. Extensive historical data on bathymetries and other data were sighted and processed. This scenario analysis of the historical conditions of the Ems estuary provides a valuable contribution to the determination of the causes of the formation and increase of fluid mud.

Three topographies were assembled, containing measurements from several years each, especially the earlier ones. The scenarios simulate the 1930s, the 1980s and 2015. Boundary and initial values were taken from 2015, due to a lack of data in the early years. However, they were tested for plausibility in order to match the measurement data used for calibration.

During the study of the historic scenarios, the influence of the topography, bottom roughness and sea level were examined. It could be shown that the topography alone has a significant influence on the hydrodynamics in the Ems Estuary. The bottom roughness is especially important in order to reproduce the characteristic behavior in the Lower Ems. The bottom roughness is here especially connected with the formation of fluid mud, since this leads to an extremely decreased roughness effect. In addition to topographic conditions, however, the availability of sediment also plays a crucial role in the siltation of an estuary. This aspect is not investigated here.

After calibrating the three scenarios with respect to the water level, further hydrodynamic parameters were examined. It can be seen that the velocities in the Lower Ems have increased, especially during flood current, amplifying the flood dominancy, which supports the import of sediment into the estuary. This effect is especially visible during low discharge events, which were considered here.

10 Prospects

The results of this report lead to a demand for further research within several areas.

Future research is urgently needed concerning model performance, since high (vertical) resolutions are needed for the sufficient representation of fluid mud. Moreover, further development of the turbulence model is required, e.g. extending the k-ω model by the buoyancy effect (Umlauf et al. 2003) or using the new k-ω model by Wilcox (2008). The mud-induced periodic stratification can be modelled by a combination of settling velocity, diffusivity, rheological viscosity and turbulence damping. The modelling results are essentially determined by sensitivities, e.g. of the parameterizations. A verification of cause-effect links is of fundamental importance. Since it is very difficult to achieve natural conditions in the laboratory, there is a clear demand also for further in-situ observations in the field, e.g. estimating turbulent kinetic energy.

In future studies of historic scenarios sediment dynamics should be included in the simulations and the influence of the turbulent horizontal viscosity should be investigated and calibrated. With the extended modeling procedure described in part II, the conditions leading to the formation of fluid mud can be further investigated and understood.
In order to be able to compare the development of the Ems Estuary to other systems, the tidal prism is a good tool. For example historic and current states of the Weser or Elbe Estuaries could be analyzed in a similar way, investigating the development and comparing it to other estuaries. Furthermore, the criteria by van Rijn and Grasmeijer (2018) can be used for evaluating the state of an estuary.

The results of the research project “MudEstuary_B” presented in this report contribute towards a better understanding and representation of fluid mud in numerical models. However, it also became clear, that further research is needed in order to be able to apply these findings to larger model domains and to understand and model the formation of fluid mud.

V References

BAW (2010): Aktionsprogramm des Bundes zur Reduzierung seines Unterhaltungsaufwandes und der Minimierung der Verschlickung der Unterems. Bericht zur vertieften Wirkanalyse. With assistance of Norbert Winkel, Dr. rer. nat. Rollenhagen. BAW, Wasserbau im Küstenbereich, Ästuarsysteme II (K3) (A39550310143).

BAW (2012): Vertiefung der Außenems bis Emden - Gutachten zu den ausbaubedingten Änderungen von Hydrodynamik, Transport und Seegang. Bundesanstalt für Wasserbau - Dienststelle Hamburg (BAW-DH). Wedeler Landstraße 157, 22559 Hamburg (Gutachten, BAW A3955 03 10144).

Becker, Marius; Maushake, Christian; Winter, Christian (2018): Observations of Mud-Induced Periodic Stratification in a Hyperturbid Estuary. In *Geophys. Res. Lett.* 45 (11), pp. 5461–5469. DOI: 10.1029/2018GL077966.

Borgsmüller, Christine; Quick, I.; Bauling, Y. (Eds.) (2016): Application of the hydromorphological assessment framework Valmorph to evaluate the changes in suspended sediment distribution in the Ems estuary. River Sedimentation: Proceedings of the 13th International Symposium on River Sedimentation. Stuttgart, Germany, 19-22 September, 2016.

Burchard, Hans; Schuttelaars, Henk M.; Ralston, David K. (2018): Sediment Trapping in Estuaries. In *Annual Review of Marine Science* 10, pp. 371–395. DOI: 10.1146/annurev-marine-010816-060535.

Casulli, V. (2009): A high-resolution wetting and drying algorithm for free-surface hydrodynamics. In *International Journal for Numerical Methods in Fluids* 60 (4), pp. 391–408. DOI: 10.1002/fld.1896.

Casulli, V.; Cheng, R. T. (1992): Semi-Implicit Finite Difference Methods for Three-Dimensional Shallow Water Flow. In *International Journal for Numerical Methods in Fluids* 15 (6), pp. 629–648. DOI: 10.1002/fld.1650150602.

Casulli, V.; Lang, G. (2004): Mathematical Model UnTRIM. The Federal Waterways Engineering and Research Institute (BAW). Hamburg, Germany (1.0). Available online at http://www.baw.de/downloads/wasserbau/mathematische_verfahren/pdf/Simulationsverfahren_Kueste_validation_document-untrim-2004.pdf.

Casulli, V.; Walters, R. A. (2000): An Unstructured grid, Three-Dimensional Model Based on the Shallow Water Equations. In *International Journal for Numerical Methods in Fluids* 32 (3), pp. 331–348. DOI: 10.1002/(SICI)1097-0363(20000215)32:3<331::AID-FLD941>3.0.CO;2-C.

Casulli, Vincenzo; Stelling, Guus S. (2011): Semi-implicit subgrid modelling of three-dimensional free-surface flows. In *Int. J. Numer. Meth. Fluids* 67 (4), pp. 441–449. DOI: 10.1002/fld.2361.

Chernetsky, A. S.; Schuttelaars, H. M.; Talke, S. A. (2010a): The Effect of Tidal Asymmetry and Temporal Settling Lag on Sediment Trapping in Tidal Estuaries. In *Ocean Dynamics* 60 (5), pp. 1219–1241. DOI: 10.1007/s10236-010-0329-8.

Chernetsky, Alexander S.; Schuttelaars, Henk M.; Talke, Stefan A. (2010b): The effect of tidal asymmetry and temporal settling lag on sediment trapping in tidal estuaries. In *Ocean Dynamics* 60 (5), pp. 1219–1241. DOI: 10.1007/s10236-010-0329-8.

Crapper, M.; Ali, K.H.M. (1997): A Laboratory Study of Cohesive Sediment Transport. In N. Burt, R. Parker, J. Watts (Eds.): Cohesive Sediments: 4th Nearshore and Estuarine Cohesive Sediment Transport Conference INTERCOH '94. Wallingford, UK: J. Wiley and Sons, pp. 197–211.

Deltares (2014): Delft3D-FLOW - Simulation of Multi-Dimensional Hydrodynamic and Transport Phenomena, Including Sediments. User Manual. Deltares (3.15.34158). Available online at https://oss.deltares.nl/documents/183920/185723/Delft3D-FLOW_User_Manual.pdf, checked on 2/28/2017.

Deutsches Gewässerkundliches Jahrbuch (1951): Emsgebiet, Abflußjahr 1951. Edited by Ministerium für Ernährung, Landwirtschaft und Forsten des Landes Nordrhein-Westfalen. Düsseldorf.

Deutsches Gewässerkundliches Jahrbuch (1958): Emsgebiet, Abflußjahr 1958. Edited by Ministerium für Ernährung, Landwirtschaft und Forsten des Landes Nordrhein-Westfalen. Düsseldorf.

Deutsches Gewässerkundliches Jahrbuch (1981): Weser-Emsgebiet, Abflußjahr 1981. Edited by Der Niedersächsische Minister für Ernährung, Landwirtschaft und Forsten - Landesstelle für Gewässerkunde. Hannover.

Deutsches Gewässerkundliches Jahrbuch (2015): Weser- und Emsgebiet 2015. Edited by NLWKN. Niedersächsischer Landesbetrieb für Wasserwirtschaft, Küsten- und Naturschutz. Available online at https://www.nlwkn.niedersachsen.de/download/138059/2015_DGJ_Weser-Ems.pdf.

Dieckmann, Reinhard (1989): Morphologische Strukturen im Weserästuar. In *Deutsche Gewässerkundliche Mitteilungen* 3, pp. 104–112.

Dijkstra, Yoeri M.; Schuttelaars, Henk M.; Schramkowski, George P. (2019a): A regime shift from low to high sediment concentrations in a tide-dominated estuary. In *Geographical Research Letters* 46 (8). DOI: 10.1029/2019GL082302.

Dijkstra, Yoeri M.; Schuttelaars, Henk M.; Schramkowski, George P.; Brouwer, Ronald L. (2019b): Modeling the transition to high sediment concentrations as a response to channel deepening in the Ems River Estuary. In *Journal of Geophysical Research: Oceans* (124:1-17). DOI: 10.1029/2018JC014367.

Eckholdt, Martin; Braun, Hans-Georg; Rohde, Hans; Rümelin, Burkart; Strähler, Walter; Uhlemann, Hans-Joachim (1998): Flüsse und Kanäle. Die Geschichte der deutschen Wasserstraßen. Hamburg: DSV-Verlag GmbH.

Engels, Andreas (2015): Salinity in the Lower Ems River - description of recent developments. NLWKN Aurich. Ems-Scheldt Workshop. Delmenhorst (13.02.2015), 2015.

Engels, Andreas (2017): Soleeinleitungen in der Ems. E-Mail-Verkehr 07.11.-18.12.2017 to Julia Benndorf, 2017.

Franzius, Otto (1986): Suspended Sediment Problems in the Brackish Transition of the Tidal Ems River. Northwest Water and Navigation Authorities, Aurich. In *Bulletin of P.I.A.N.C.* 1986 (53), pp. 37–62.

FTZ (2016): Planung Großschiffsliegeplatz Emden. Wasserbauliche Systemanalyse Los 6.2. With assistance of Katharina Niederndorfer, Gerd Bruss, Roberto Mayerle. Edited by FTZ Westküste.

G. Klaassen (2018): Rysumer Nacken/Knock. Edited by Ostfriesland-Entdecken.de. Available online at https://ostfriesland-entdecken.de/land/rysumer-nacken/.

Gewässerkundliches Jahrbuch (2014): DGJ Weser-Emsgebiet 2014. Edited by NLWKN BSt. Hannover-Hildesheim. Available online at https://www.nlwkn.niedersachsen.de/wasserwirtschaft/publikationen/gewaesserkundliche_monatsberichte/deutsches_gewaesserkundliches_jahrbuch/deutsches-gewaesserkundliches-jahrbuch-weser--und-emsgebiet-43607.html.

Giese, Egon (1972): Fahrwasserumbildungen in der Unter-und Außenelbe. In *Mitteilungsblatt der Bundesanstalt für Wasserbau* (32), pp. 89–108.

Grabau, Jürgen (2004): Grundinstandsetzung der Schleusen an der DEK-Nordstrecke. oder Beitrag über die Projektarbeit in der WSV. In Wasser- und Schifffahrtsdirektion Nordwest (Ed.): Zwischen Weser und Ems, vol. 38, pp. 15–27. Available online at http://www.wsd-nordwest.wsv.de/pdf/Heft_38.pdf, checked on 1/18/2018.

Grasso, F.; Le Hir, Pierre (2019): Influence of morphological changes on suspended sediment dynamics in a macrotidal estuary: diachronic analysis in the Seine Estuary (France) from 1960 to 2010. In *Ocean Dynamics* 69, pp. 83–100. DOI: 10.1007/s10236-018-1233-x.

Groningen Seaports (2015): De Eemshaven.

Hensen, Walter (1954): Modellversuche für die untere Ems. Franzius Institut der Technischen Hochschule Hannover. Hannover (Mitteilungen der Hannoverschen Versuchsanstalt für Grundbau und Wasserbau).

Herrling, Gerald; Niemeyer, Hanz Dieter (2008a): Comparison of the Hydrodynamic Regime of 1937 and 2005 in the Ems-Dollard Estuary by Applying Mathematical Modeling. Lower Saxony Water Management, Coastal Defence and Nature Conservation Agency, Coastal Research Station. Available online at http://www.nlwkn.niedersachsen.de/wasserwirtschaft/nordseekueste/fsk/kuesteningenieurwesen/kuesteningenieurwesen-106527.html.

Herrling, Gerald; Niemeyer, Hanz Dieter (2008b): Comparison of the Hydrodynamic Regime of 1937 and 2005 in the Ems-Dollard Estuary by Applying Mathematical Modeling. Lower Saxony Water Management, Coastal Defence and Nature Conservation Agency, Coastal Research Station. Available online at http://www.nlwkn.niedersachsen.de/wasserwirtschaft/nordseekueste/fsk/kuesteningenieurwesen/kuesteningenieurwesen-106527.html.

Herrling, Gerald; Niemeyer, Hanz Dieter (2008c): Reconstruction of the historical tidal regime of the Ems-Dollard estuary prior to significant human changes by applying mathematical modeling. Edited by Niedersächsischer Landesbetrieb für Wasserwirtschaft, Küsten- und Naturschutz

(NLWKN). Available online at http://www.nlwkn.niedersachsen.de/wasserwirtschaft/nordseekueste/fsk/kuesteningenieurwesen/kuesteningenieurwesen-106527.html.

Jahrbuch für die Gewässerkunde des deutschen Reiches (1937): Weser-Emsgebiet, Abflußjahr 1937. Edited by Landesanstalt für Gewässerkunde und Hauptnivellements. Berlin.

Janssen, Theodor (1968): Das Elend des Emsfahrwassers und seine Beseitigung. Verlag Ostfriesische Landschaft, Aurich.

Jensen, Jürgen; Mudersbach, Christoph; Blasi, Christoph (2003): Hydrological Changes in Tidal Estuaries Due to Natural and Anthropogenic Effects. Proceedings of the 6. International MEDCOAST 2003-Conference. Ravenna, Italy.

Jonge, V. N. de (1992): Tidal flow and residual flow in the Ems estuary. In *Estuarine, Coastal and Shelf Science* 34 (1), pp. 1–22. DOI: 10.1016/S0272-7714(05)80123-4.

Jonge, Victor N. de; Schuttelaars, Henk M.; van Beusekom, Justus E.E.; Talke, Stefan A.; Swart, Huib E. de (2014): The influence of channel deepening on estuarine turbidity levels and dynamics, as exemplified by the Ems estuary. In *Estuarine, Coastal and Shelf Science* 139, pp. 46–59. DOI: 10.1016/j.ecss.2013.12.030.

Knoch, D.; Malcherek, A. (2011): A Numerical Model for Simulation of Fluid Mud with Different Rheological Behaviors. In *Ocean Dynamics* 61 (2), pp. 245–256. DOI: 10.1007/s10236-010-0327-x.

Krause, N.; Hoogland, J. R. (1995): Emsmündung - Eemsmonding. Grenzüberschreitende Zusammenarbeit in der Emsmündung. Edited by Ständige Deutsch-Niederländische Emskommission.

Krebs, Martin (2015): Seasonal effects on ssc for the lower Ems. Ems-Scheldt Workshop. Delmenhorst, 2015.

Krebs, Martin; Weilbeer, Holger (2008): Ems-Dollart Estuary. In *Die Küste* (74), pp. 252–264.

Lang, A. W. (1954): Untersuchung zum Gestaltungswandel des Emsmündungstrichters. von der Mitte des 16. Jahrhunderts bis zum Beginn des 20. Jahrhunderts. Wasser- und Schifffahrtsamt Emden, Abteilung Emsmessung.

Lange, Jürgen (2006): Ausbau der Unterems. Eine Chronik der Maßnahmen seit 1984 mit einer Bewertung der Umweltfolgen. Edited by WWF Deutschland. Frankfurt am Main.

Launder, B. E.; Spalding, D. B. (1974): The numerical computation of turbulent flows. In *Computer Methods in Applied Mechanics and Engineering* 3 (2), pp. 269–289. DOI: 10.1016/0045-7825(74)90029-2.

Le Hir, P.; Bassoullet, P.; Jestin, H. (2001): Application of the continuous modeling concept to simulate high-concentration suspended sediment in a macrotidal estuary. In W. H. McAnally, A. J Mehta (Eds.): Coastal and Estuarine Fine Sediment Processes, vol. 3: Elsevier Science (Proceedings in Marine Science), pp. 229–247.

LfU (2003): Hydraulik naturnaher Fließgewässer. Teil 3 - Rauheits- und Widerstandsbeiwerte für Fließgewässer in Baden-Württemberg. Edited by Landesanstalt für Umweltschutz Baden-Württemberg, Referat 41. Karlsruhe.

Malcherek, Andreas; Cha, H. (2011): Zur Rheologie von Flüssigschlicken: Experimentelle Untersuchungen und theoretische Ansätze - Projektbericht. University of the German Armed Forces, Institute of Hydro Science. Munich, Germany (Heft 111).

McAnally, W. H.; Friedrichs, C.; Hamilton, D.; Hayter, E.; Shrestha, P.; Rodriguez, H. et al. (2007): Management of Fluid Mud in Estuaries, Bays, and Lakes. I: Present State of Understanding on Character and Behavior. In *Journal of Hydraulic Engineering* 133 (1), pp. 9–22. DOI: 10.1061/(ASCE)0733-9429(2007)133:1(9).

Menter, F. R. (1994): Two-equation eddy-viscosity turbulence models for engineering applications. In *AIAA Journal* 32 (8), pp. 1598–1605. DOI: 10.2514/3.12149.

O'Brien, M. P. (1931): Estuary Tidal Prisms Related to Entrance Areas. In *Civil Engineer* 1 (8), pp. 738–739.

O'Brien, M. P. (1969): Equilibrium flow areas of inlets on sandy coasts. In *Journal of the Waterways and Harbours division*, pp. 43–52.

Richardson, J. F.; Zaki, W. N. (1954): Sedimentation and Fluidisation: Part 1. In *Transactions of the Institute of Chemical Engineers* 32, pp. 35–53.

Rodi, W. (1987): Examples of calculation methods for flow and mixing in stratified fluids. In *Journal of Geophysical Research: Oceans* 92 (C5), pp. 5305–5328. DOI: 10.1029/JC092iC05p05305.

Roland, Aron; Ferrarin, Christian; Bellafiore, Debora; Zhang, Yinglong Joseph; Dutour Sikric, Mathieu; Zanke, U.; Umgiesser, G. (2012): Über Strömungsmodelle auf unstrukturierten Gitternetzen zur Simulation der Dynamik von Flüssigschlick. In *Die Küste* 79, pp. 53–81.

Sarah Koch (2018): Berechnung und Analyse der Tideprismen in deutschen Ästuaren mit besonderem Fokus auf die Ems. Masterarbeit, Braunschweig, Hamburg. Leichtweiß Institut für Wasserbau; Bundesanstalt für Wasserbau.

Schoemans, Marjolijn (2013): Tidal changes in the Lower Ems (1945-2005): reconstructing the effects of channel deepening and bottom roughness. BSc thesis. Utrecht University, Utrecht. Faculty of Geosciences; Department of Physical Geography. Available online at https://www.waddenacademie.nl/fileadmin/inhoud/pdf/06-wadweten/Scripties/Scriptie_MSchoemans.pdf, checked on 4/23/2018.

Schrottke, K. (Ed.) (2006): Dynamik fluider Schlicke im Weser und Ems Ästuar - Untersuchungen und Analysen zum Prozessverständnis. BAW/BfG-Kolloquium Nov.2006.

Schubert, Kurt (1970): Ems und Jade. In *Die Küste* 1970 (19), pp. 29–67.

Talke, Stefan A.; de Swart, Huib E. (2006): Hydrodynamics and Morphology in the Ems/Dollard Estuary. Review of Models, Measurements, Scientific Literature, and the Effects of Changing Conditions. University of Utrecht. Utrecht (IMAU Report, R 06-01).

Toorman, E. A.; Bruens, A. W.; Kranenburg, C.; Winterwerp, J. C. (2002): Interaction of Suspended Cohesive Sediment and Turbulence. In J.C. Winterwerp, C. Kranenburg (Eds.): Fine Sediment Dynamics in the Marine Environment, vol. 5. Amsterdam, San Diego, Oxford, London: Elsevier Science (Proceedings in Marine Science), pp. 7–23.

Toorman, Erik A. (2000): Parameterization of Turbulence Damping in Sediment-laden Flow. MAST3 - COSINUS. Departement Laboratoire National Hydraulique Et Environment (HYD/ET/ 00/COSINUS/3).

Uliczka, Klemens (1997): Sturmflutsperrwerk Ems bei Gandersum. Salzgehalts- und Schwebstoffverhältnisse in der Unterems. Bundesanstalt für Wasserbau (BAW). Hamburg.

Umlauf, L.; Burchard, H.; Hutter, K. (2003): Extending the k–ω turbulence model towards oceanic applications. In *Ocean Modelling* 5 (3), pp. 195–218. DOI: 10.1016/S1463-5003(02)00039-2.

Umlauf, Lars; Burchard, Hans (2005): Second-order turbulence closure models for geophysical boundary layers. A review of recent work. In *Continental Shelf Research* 25 (7-8), pp. 795–827. DOI: 10.1016/j.csr.2004.08.004.

van Kessel, Thijs; Winterwerp, Han; van Prooijen, Bram; van Ledden, Mathijs; Borst, Wil (2011): Modelling the seasonal dynamics of SPM with a simple algorithm for the buffering of fines in a sandy seabed. In *Continental Shelf Research* 31 (10), S124-S134. DOI: 10.1016/j.csr.2010.04.008.

van Maren, Bas; Stolte, Willem; Sittoni, Luca; Vroom, Julia; Arentz, Loana (2012a): Mud dynamics in the Ems Estuary (7), phase 2. Model analysis, final report. In Deltares (Ed.): MudDynamics.

van Maren, Bas; Vroom, Julia; Vijverberg, Thomas; Schoemans, Marjolijn; van Rooijen, Arnold (2012b): Mud dynamics in the Ems-Dollard (4), phase 2. Set up hydrodynamic models, final report. In Deltares (Ed.): MudDynamics.

van Maren, Bas; Vroom, Julia; Vijverberg, Thomas; Schoemans, Marjolijn; van Rooijen, Arnold (2012c): Mud dynamics in the Ems-Dollard (4), phase 2. Set up hydrodynamic models, final report. In Deltares (Ed.): MudDynamics.

van Maren, Dirk S.; van Kessel, Thijs; Cronin, Katherine; Sittoni, Luca (2015a): The impact of channel deepening and dredging on estuarine sediment concentration. In *Continental Shelf Research* 95, pp. 1–14. DOI: 10.1016/j.csr.2014.12.010.

van Maren, Dirk S.; Winterwerp, Johan C.; Vroom, Julia (2015b): Fine sediment transport into the hyper-turbid lower Ems River: the role of channel deepening and sediment-induced drag reduction. In *Ocean Dynamics* 65 (4), pp. 589–605. DOI: 10.1007/s10236-015-0821-2.

van Rijn, L. C. (1993): Principles of Sediment Transport in Rivers, Estuaries and Coastal Seas. Amsterdam, The Netherlands: Aqua Publications.

van Rijn, Leo; Grasmeijer, Bart (2018): Effect of channel deepening on tidal flow and sediment transport. Part II: Muddy channels. In *Ocean Dynamics* 73 (3), p. 587. DOI: 10.1007/s10236-018-1205-1.

van Rijn, Leo C. (2007): Unified View of Sediment Transport by Currents and Waves. II: Suspended Transport. In *Journal of Hydraulic Engineering* 133 (6), pp. 668–689.

Viollet, P. L. (1988): On the Numerical Modelling of Stratified Flows. In : Physical Processes in Estuaries: Springer-Verlag, pp. 257–277.

Warner, J. C.; Sherwood, C. R.; Arango, H. G.; Signell, R. P. (2005): Performance of four turbulence closure models implemented using a generic length scale method. In *Ocean Modelling* 8, pp. 81–113.

Wasser- und Schifffahrtsamt Emden (1995): Unterems: Baggermengen aus der Ems. Bundesanstalt für Wasserbau (BAW). Tabelle.

Wasser- und Schifffahrtsamt Emden (2015): Unterhaltungsbaggerungen in der Unter- und Außenems. Wasser- und Schifffahrtsamt Emden. Available online at https://www.wsv.de/wsa-emd/wasserstrassen/Baggerei/Unterhaltungsbaggerungen/index.html, checked on 8/9/2017.

Wasser- und Schifffahrtsamt Meppen: Schleusen. Wasser- und Schifffahrtsamt Meppen. Available online at http://www.wsa-meppen.de/wir_ueber_uns/amt_u_aussenstellen/sachbereich_2/schleusen_wehre_tore/schleusen/, checked on 1/19/2018.

Wehr, Denise (2012): An Isopycnal Numerical Model for the Simulation of Fluid Mud Dynamics. Dissertation. Universität der Bundeswehr München, Neubiberg. Fakultät für Bauingenieurwesen und Umweltwissenschaften.

Whitehouse, R.; Soulsby, R.; Roberts, W.; Mitchener, H. (2000): Dynamics of Estuarine Muds. London, UK: Thomas Telford Ltd (HR Wallingford).

Wilcox, D. C. (1993): Turbulence Modeling for CFD. 1st. Palm Drive, CA, USA: DCW Industries.

Wilcox, David C. (2008): Formulation of the k-w Turbulence Model Revisited. In *AIAA Journal* 46 (11), pp. 2823–2838. DOI: 10.2514/1.36541.

Wildvang, Dodo (1937): Der Einbruch der Nordsee in das Mündungsgebiet der Ems. Edited by Naturwissenschaftlicher Verein zu Bremen (Reihe B 30.1/2, 33-53).

Winkel, Norbert (2017): Sedimentbaggerungen in der Ems. persönliches Gespräch to Julia Benndorf. Hamburg, 2017.

Winterwerp, J. C. (1999): On the Dynamics of High-Concentrated Mud Suspensions. Delft University of Technology, Delft, The Netherlands. Available online at http://repository.tudelft.nl/view/ir/uuid:0b503064-91ad-48de-8174-761c315f8132/.

Winterwerp, J. C. (2002): On the Flocculation and Settling Velocity of Estuarine Mud. In *Continental Shelf Research* 22 (9), pp. 1339–1360. DOI: 10.1016/S0278-4343(02)00010-9.

Winterwerp, J. C.; Wang, Z. B.; van Kester, J.A.T.M.; Verweij, J. F. (2002): Far-field Impact of Water Injection dredging in the Crouch River. In *Proceedings of the ICE - Water and Maritime Engineering* 154 (4), pp. 285–296. DOI: 10.1680/wame.2002.154.4.285.

Winterwerp, Johan C. (2010): Fine sediment transport by tidal asymmetry in the high-concentrated Ems River. Indications for a regime shift in response to channel deepening. In *Ocean Dynamics* 61 (2-3), pp. 203–215. DOI: 10.1007/s10236-010-0332-0.

Winterwerp, Johan C.; Wang, Zheng Bing; van Braeckel, Alexander; van Holland, Gijsbert; Kösters, Frank (2013): Man-induced regime shifts in small estuaries? II: a comparison of rivers. In *Ocean Dynamics* 63 (11-12), pp. 1293–1306. DOI: 10.1007/s10236-013-0663-8.

Wurpts, Andreas (2017): Development of a fluid mud module for the hydromorphodynamic regime of the Ems estuary. FSK NLWKN. Gandersum, 9/25/2017.

Bundesanstalt für Wasserbau
Hamburg, März 2020

VI Appendix

11 Mathematical description

Fluid mud suspensions represent non-Newtonian fluids with variable rheological viscosity in contrast to Newtonian fluids such as water with constant viscosity. As consequences for non-Newtonian fluids, the solution algorithm of hydrodynamic numerical models has to be adopted or suitable approximations are required. In order to allow the application of conventional hydrodynamic models using Navier-Stokes equations for the simulation of fluid mud dynamics, the following approximations are necessary:

- approximation of the internal stress tensor of momentum equation
- approximation of the deformation rate tensor of the rheological viscosity

In this appendix, brief descriptions of these required approximations are given. As source for these approximations it is referred to Wehr (2012).

In section 11.1 the **internal stress tensor** of the momentum equation is described for

- general motion,
- Newtonian fluids,
- non-Newtonian fluids, and
- the approximation of fluid mud.

In section 11.2 the **rheological viscosity** is defined for

- simple 1D shear,
- general 3D shear, and
- the approximation of fluid mud.

The model UnTRIM is applied as a hydrodynamic model for coastal areas and estuaries. The following question is discussed: What changes need to be made in order to consider fluid mud dynamics by an implementation of a rheological viscosity in UnTRIM?

Therefore, in section 11.3 for the model **UnTRIM**

- the general governing equations are given, and
- the changes and challenges in consideration of a rheological viscosity are discussed.

11.1 Internal Stress Tensor

11.1.1 Cauchy's equation of motion & general internal stress tensor

Cauchy's equation of motion describes the momentum transport in any continuum. The equation is given in index notation in equation (30), in vector notation in equation (31), and fully written in equations (32)-(34).

index notation

$$\frac{\partial u_i}{\partial t} = -\frac{1}{\rho}\frac{\partial p}{\partial x_i} + \frac{1}{\rho}\frac{\partial \tau_{ji}}{\partial x_j} + f_i \qquad \textbf{(30)}$$

u	[m/s]	velocity
τ_{ji}		stress tensor
p		pressure
f		external force

vector notation

$$\frac{D\boldsymbol{u}}{Dt} = -\frac{1}{\rho} grad\ p + \frac{1}{\rho} div\ \boldsymbol{\tau} + \boldsymbol{f} \qquad \textbf{(31)}$$

fully written

$$\frac{\partial u}{\partial t} + u\frac{\partial u}{\partial x} + v\frac{\partial u}{\partial y} + w\frac{\partial u}{\partial z} = -\frac{1}{\rho}\frac{\partial p}{\partial x} + \frac{1}{\rho}\left(\frac{\tau_{xx}}{\partial x} + \frac{\tau_{yx}}{\partial y} + \frac{\tau_{zx}}{\partial z}\right) + f_x \qquad \textbf{(32)}$$

$$\frac{\partial v}{\partial t} + u\frac{\partial v}{\partial x} + v\frac{\partial v}{\partial y} + w\frac{\partial v}{\partial z} = -\frac{1}{\rho}\frac{\partial p}{\partial y} + \frac{1}{\rho}\left(\frac{\tau_{xy}}{\partial x} + \frac{\tau_{yy}}{\partial y} + \frac{\tau_{zy}}{\partial z}\right) + f_y \qquad \textbf{(33)}$$

$$\frac{\partial w}{\partial t} + u\frac{\partial w}{\partial x} + v\frac{\partial w}{\partial y} + w\frac{\partial w}{\partial z} = -\frac{1}{\rho}\frac{\partial p}{\partial z} + \frac{1}{\rho}\left(\frac{\tau_{xz}}{\partial x} + \frac{\tau_{yz}}{\partial y} + \frac{\tau_{zz}}{\partial z}\right) + f_z \qquad \textbf{(34)}$$

The terms of internal viscous stresses are the second terms of the left side of Cauchy's equation. Hence, the **general expression of the internal stress tensor** is given by equation (35):

$$\frac{1}{\rho} div\ \boldsymbol{\tau} = \frac{1}{\rho} div \begin{bmatrix} \tau_{xx} & \tau_{xy} & \tau_{xz} \\ \tau_{yx} & \tau_{yy} & \tau_{yz} \\ \tau_{zx} & \tau_{zy} & \tau_{zz} \end{bmatrix} \qquad \textbf{(35)}$$

The stress tensor can be specified through constitutive relation of characteristic fluid properties. By expressing the stress tensor in terms of viscosity and fluid velocity, and assuming constant density and viscosity, the Cauchy momentum equation will lead to the Navier-Stokes equation. In the following section the differences of the internal stress tensor of Newtonian and non-Newtonian fluids are discussed.

11.1.2 Internal stress tensor of Newtonian fluid

The i**nternal stress tensor of a Newtonian incompressible fluid** is given by equation (36):

$$\frac{\mu}{\rho} div(\nabla u + \nabla u^T) = \frac{\mu}{\rho}\begin{bmatrix} 2\frac{\partial}{\partial x}\left(\frac{\partial u}{\partial x}\right) + \frac{\partial}{\partial y}\left(\frac{\partial u}{\partial y} + \frac{\partial v}{\partial x}\right) + \frac{\partial}{\partial z}\left(\frac{\partial u}{\partial z} + \frac{\partial w}{\partial x}\right) \\ \frac{\partial}{\partial x}\left(\frac{\partial u}{\partial y} + \frac{\partial v}{\partial x}\right) + 2\frac{\partial}{\partial y}\left(\frac{\partial v}{\partial y}\right) + \frac{\partial}{\partial z}\left(\frac{\partial v}{\partial z} + \frac{\partial w}{\partial y}\right) \\ \frac{\partial}{\partial x}\left(\frac{\partial u}{\partial z} + \frac{\partial w}{\partial x}\right) + \frac{\partial}{\partial y}\left(\frac{\partial v}{\partial z} + \frac{\partial w}{\partial y}\right) + 2\frac{\partial}{\partial z}\left(\frac{\partial w}{\partial z}\right) \end{bmatrix} \quad \textbf{(36)}$$

A reconstruction and application of the continuity equations leads to equation (37):

$$\frac{1}{\rho} div\, \boldsymbol{\tau} = \frac{\mu}{\rho}\begin{bmatrix} \frac{\partial^2 u}{\partial x^2} + \frac{\partial^2 u}{\partial y^2} + \frac{\partial^2 u}{\partial z^2} \\ \frac{\partial^2 v}{\partial x^2} + \frac{\partial^2 v}{\partial y^2} + \frac{\partial^2 v}{\partial z^2} \\ \frac{\partial^2 w}{\partial x^2} + \frac{\partial^2 w}{\partial y^2} + \frac{\partial^2 w}{\partial z^2} \end{bmatrix} \quad \textbf{(37)}$$

This is a decoupled system of the x,y,z-components of the viscous stress terms, i.e. x-components of the stress term consist only of derivatives of the x-velocity; y-components and z-components of derivatives of the y-velocity and z-velocity, respectively. The Newtonian stress tensor contains only linear terms $\frac{\mu}{\rho}\frac{\partial^2 u_i}{\partial x_i^2}$. The 3D stress tensor of Newtonian fluids represents a parabolic diffusion equation with constant viscosity (diffusive) coefficient $\frac{\mu}{\rho}$.

11.1.3 Internal stress tensor of Non-Newtonian fluid

The i**nternal stress tensor of a non-Newtonian fluid** is given by equation (37):

$$div(\nu \mathbf{D}) = \begin{bmatrix} \frac{\partial}{\partial x}\left(\nu\left(\frac{\partial u}{\partial x} + \frac{\partial u}{\partial x}\right)\right) + \frac{\partial}{\partial y}\left(\nu\left(\frac{\partial u}{\partial y} + \frac{\partial v}{\partial x}\right)\right) + \frac{\partial}{\partial z}\left(\nu\left(\frac{\partial u}{\partial z} + \frac{\partial w}{\partial x}\right)\right) \\ \frac{\partial}{\partial x}\left(\nu\left(\frac{\partial u}{\partial y} + \frac{\partial v}{\partial x}\right)\right) + \frac{\partial}{\partial y}\left(\nu\left(\frac{\partial v}{\partial y} + \frac{\partial v}{\partial y}\right)\right) + \frac{\partial}{\partial z}\left(\nu\left(\frac{\partial v}{\partial z} + \frac{\partial w}{\partial y}\right)\right) \\ \frac{\partial}{\partial x}\left(\nu\left(\frac{\partial u}{\partial z} + \frac{\partial w}{\partial x}\right)\right) + \frac{\partial}{\partial y}\left(\nu\left(\frac{\partial v}{\partial z} + \frac{\partial w}{\partial y}\right)\right) + \frac{\partial}{\partial z}\left(\nu\left(\frac{\partial w}{\partial z} + \frac{\partial w}{\partial z}\right)\right) \end{bmatrix} \quad \textbf{(38)}$$

In contrast to Newtonian fluids the viscosity is not constant but variable. The variable kinematic viscosity is a function of space x, time t, density ρ which corresponds to the suspended sediment concentration and shear rate. Therefore, the derivation of the viscosity has to be considered and an application of the continuity equation (see eq. (35) for Newtonian fluids) is not possible. The non-Newtonian stress tensor contains also non-linear terms $\frac{\partial}{\partial x_i}\left(\nu\frac{\partial u_i}{\partial x_j}\right)$, where ν is a non-

negative function of the derivatives $\frac{\partial u_i}{\partial x_i}$. The extra stress tensor cannot be expressed as a linear, isotropic function of the components of the velocity gradient. The stress terms of the directions x,y,z are strongly coupled by the mixed derivatives (e.g. $\frac{\partial u_i}{\partial x_i \partial x_j}$) and by the presence of all three components of the velocity vector.

The 3D stress tensor of non-Newtonian fluids represents a hyperbolic diffusion equation. As a consequence, the solution system of the stress tensors differs from Newtonian and non-Newtonian fluids. The solution algorithm of the numerical model has to be changed significantly.

11.1.4 Internal stress tensor of fluid mud

Fluid mud can be characterized as a non-Newtonian fluid with a rheological viscosity. In order to allow the application of conventional hydrodynamic models using Navier-Stokes equations for the simulation of fluid mud dynamics, an approximation of the internal stress tensor is necessary.

An **approximation for the internal stress tensor of high-concentrated mud suspensions** was developed by Wehr (2012, pp. 37–39). For this purpose, a dimensional analysis was performed and the significant internal stresses were identified. The results of the analysis of the most important characteristics and processes of fluid mud dynamics are summarized in the following paragraph:

- The rheological viscosity is independent from the direction of loading. A material can be sheared in one or more directions. As long as the absolute value of the shear rate vector or tensor remains the same, then the viscous response will be the same.
- The dominated movement of a fluid mud layer takes place in horizontal direction and not in vertical direction.
- The dominated variation of velocity takes place in vertical direction and not in horizontal direction.
- The characteristic horizontal length of a fluid mud layer (several hundred meters) is bigger than the characteristic vertical length of a fluid mud layer (decimeters or meters).

In summary, in the viscous stress term the horizontal derivatives in z-direction ($\frac{\partial^2 u}{\partial z^2}$ and $\frac{\partial^2 v}{\partial z^2}$) have the greatest influence on the fluid mud dynamics. The vertical derivatives in x-and y-direction ($\frac{\partial^2 w}{\partial x^2}$ and $\frac{\partial^2 w}{\partial y^2}$) have the least influence on the fluid mud behaviour.

As a result, the non-linear terms were neglected and the following terms of the internal stress tensor were considered:

$$\frac{\partial}{\partial x}\left(\nu\frac{\partial u}{\partial x}\right)+\frac{\partial}{\partial y}\left(\nu\frac{\partial u}{\partial y}\right)+\frac{\partial}{\partial z}\left(\nu\frac{\partial u}{\partial z}\right) \quad \textbf{(39)}$$

$$\frac{\partial}{\partial x}\left(\nu\frac{\partial v}{\partial x}\right)+\frac{\partial}{\partial y}\left(\nu\frac{\partial v}{\partial y}\right)+\frac{\partial}{\partial z}\left(\nu\frac{\partial v}{\partial z}\right) \quad \textbf{(40)}$$

$$\frac{\partial}{\partial x}\left(\nu\frac{\partial w}{\partial x}\right)+\frac{\partial}{\partial y}\left(\nu\frac{\partial w}{\partial y}\right)+\frac{\partial}{\partial z}\left(\nu\frac{\partial w}{\partial z}\right) \quad \textbf{(41)}$$

This approximation allows the application of conventional hydrodynamic models using Navier-Stokes equations.

11.2 Rheological viscosity

The non-Newtonian flow behavior is described by the rheological viscosity:

$$\nu_r = \mu_r/\rho \quad \textbf{(42)}$$

ν_r	m^2/s	kinetic rheological viscosity
μ_r	kg/(ms)	dynamic rheological viscosity
ρ	kg/m^3	density

For the isopycnal fluid mud model with (x, y, ρ)-coordinate system developed by Wehr (2012) the rheological viscosity is determined for each single isopycnal layer.
The horizontal and vertical viscosity components are functions of the rheological viscosity ν_r and turbulent viscosity ν_t. The interaction of the two viscosity components is not known and is part of the research within the project "MudEstuary". As approximation, it is assumed that the horizontal and vertical viscosities are the sum of the rheological and turbulent viscosities:

$$\nu^h = \nu_r + \nu_t^h \; and \; \nu^v = \nu_r + \nu_t^v \quad \textbf{(43)}$$

ν^h, ν^v	m^2/s	horizontal/vertical viscosity
ν_t^h, ν_t^v	m^2/s	horizontal/vertical turbulent viscosity

It has to be ensured that the horizontal and vertical viscosities are non-negative as the viscosity terms will otherwise have an accelerating effect on the advective terms.
The rheological viscosity is determined by constitutive formulations, i.e. a function of space x, time t, density ρ which corresponds to the suspended sediment concentration and shear rate intensity.

11.2.1 General 1D

For simple shear (e.g. laminar Couette flow in x-direction) the rheological viscosity is defined as the ratio of the shear stress and shear rate:

$$\mu_r = \frac{|\tau_{xz}|}{|\dot{\gamma}_{xz}|} \tag{44}$$

μ_r	kg/(ms)	dynamic rheological viscosity
τ_{xz}		shear stress
$\dot{\gamma}_{xz}$		shear rate

where the shear rate component $\dot{\gamma}_{xz}$ is equal to $\frac{\partial u}{\partial z}$ and all quantities are scalar values.

11.2.2 General 3D

In 3D the shear stress and shear rate are described by a tensor:

$$\mu_r = \frac{\boldsymbol{\tau}}{\boldsymbol{D}} \tag{45}$$

11.2.3 Fluid mud 3D: approximation of deformation rate tensor

In order to allow the application of conventional hydrodynamic models using Navier-Stokes equations for the simulation of fluid mud dynamics, an approximation of the deformation rate tensor of the rheological viscosity is necessary.

An approximation of the deformation rate tensor for mud suspensions was developed by Wehr (2012) and the results are summarized in the following paragraph.
As a general tensor formulation for non-Newtonian fluids, the viscosity can be defined by a function of the second invariant of the deformation rate tensor (neglecting the first and third invariant). The second invariant deformation rate tensor is a function of the velocity gradients:

$$\begin{aligned} II_D = & -2\left(\left(\frac{\partial u}{\partial x}\right)^2 + \left(\frac{\partial v}{\partial y}\right)^2 + \left(\frac{\partial w}{\partial z}\right)^2\right) \\ & -\left(\frac{\partial u}{\partial y} + \frac{\partial v}{\partial x}\right)^2 - \left(\frac{\partial u}{\partial z} + \frac{\partial w}{\partial x}\right)^2 - \left(\frac{\partial v}{\partial z} + \frac{\partial w}{\partial y}\right)^2 \end{aligned} \tag{46}$$

Considering different rheological constitutive laws the rheological viscosity can be described as

$$\mu_r(II_D) = \frac{\tau_y}{\sqrt{|II_D|}} + 2\mu_B \tag{47}$$

for a Bingham fluid

$$\mu_r(II_D) = \frac{\tau_y}{\sqrt{|II_D|}} + K\sqrt{|II_D|}^{(b-1)} \tag{48}$$

for a generalized Newtonian power-law fluid

$$\mu_r(II_D) = \frac{\tau_y}{\sqrt{|II_D|}} + 2^b K\sqrt{|II_D|}^{(b-1)} \tag{49}$$

for a Herschel-Bulkley fluid

$$\mu_r(II_D) = \frac{\tau_y}{\sqrt{|II_D|}} + 2\mu_\infty + \frac{\Delta\mu}{\frac{c_{break}}{c_{aggr}}\sqrt{|II_D|} + 1} \tag{50}$$

for a Worrall-Tuliani fluid

τ_y	yield stress
μ_B	Bingham viscosity
K	empirical parameter (consistency coefficient)
b	empirical parameter (flow index)
μ_∞	viscosity at total broken structure
$\Delta\mu$	
c_{break}	empirical parameter (break-up of aggregates)
c_{aggr}	empirical parameter

The approximation of the Worrall-Tuliani approach for rivers or estuaries is described by Wehr (2012, p. 52): For the Worrall-Tuliani approach the second invariant is part of the denominator. The term $\sqrt{|II_D|}$ describes the intensity of the shear rate independent from the direction of action. The flow regime of a river or estuary is dominated by vertical gradients of horizontal velocity. The vertical velocity gradients are significantly greater than the horizontal velocity gradients. Furthermore, the horizontal derivatives of the horizontal velocity components are very small. Hence, a sufficient approximation for $|II_D|$ is obtained by neglecting derivatives of the vertical velocity and the horizontal derivatives of the horizontal velocity:

$$II_D = -\left[\left(\frac{\partial u}{\partial z}\right)^2 - \left(\frac{\partial v}{\partial z}\right)^2\right] \tag{51}$$

As a result, the rheological viscosity of the Worrall-Tuliani fluid for 3D flow is defined by:

$$\mu_r(II_D) = \frac{\tau_y}{\sqrt{\left|\left(\frac{\partial u}{\partial z}\right)^2 + \left(\frac{\partial v}{\partial z}\right)^2\right|}} + 2\mu_\infty + \frac{\Delta\mu}{\frac{c_{break}}{c_{aggr}}\sqrt{\left|\left(\frac{\partial u}{\partial z}\right)^2 + \left(\frac{\partial v}{\partial z}\right)^2\right|} + 1} \tag{52}$$

Where II_D should be non-negative and non-zero:

$$II_D \leq D_{limit}; D_{limit} = 1 \cdot 10^{-6}$$

A list of **assumptions and approximations** that have been introduced into the formulation of the rheological viscosity of the Worrall-Tuliani fluid for 3D flow:

1. neglecting the first invariant of the deformation rate tensor
2. neglecting the third invariant of the deformation rate tensor
3. neglecting parts of the second invariant of the deformation rate tensor, i.e. derivatives of the vertical velocity and the horizontal derivatives of the horizontal velocity

If the rheological behavior of the fluid mud becomes similar to a plastic solid, e.g. consolidated mud, these assumptions and approximations may no longer be valid.

The rheological viscosity is a function of space x, time t, density ρ which corresponds to the suspended sediment concentration and shear rate intensity $|\mathrm{II}_D|$. The rheological viscosity has no vectorised components and its horizontal and vertical values are equal. (It has to be ensured that the horizontal and vertical viscosities are non-negative as the viscosity terms will otherwise have an accelerating effect on the advective terms.)

11.3 UnTRIM

11.3.1 General governing equations

The numerical method UnTRIM was developed by Prof. Vincenzo Casulli (Trento University, Italy). UnTRIM is a semi-implicit finite difference (-volume) model based on the three-dimensional shallow water equations as well as on the three-dimensional transport equation for salt, heat, dissolved matter and suspended sediments. In contrast to conventional finite difference methods UnTRIM is able to operate on an unstructured orthogonal grid. It solves the Reynolds-averaged Navier-Stokes equations (RANS) in a Cartesian (x, y, z)-coordinate system. For detailed references of the mathematical model it is referred to Casulli and Walters (2000). For the validation document and a general introduction to UnTRIM it is referred to Casulli and Lang (2004). The following summary and description of the governing equations is based on Casulli and Lang (2004).

As shown before, the non-Newtonian fluid behavior of fluid mud can be approximated by

- the most important internal stress components of the momentum equation (see section 11.1), and
- the rheological viscosity with the most important components of the deformation rate tensor (see section 11.2).

With these approximations, the general solution algorithm of conventional hydrodynamic models using Navier-Stokes equations is still applicable.

If these approximations for the non-Newtonian fluid behavior are considered in UnTRIM,

- the internal stress terms of horizontal viscosity of the momentum equations (eq. **(53)** - **(55)**) need to be modified, and
- the calculation of the vertical and horizontal viscosity would change to the sum of turbulent viscosity and rheological viscosity (eq. **(43)**).

These changes are highlighted in the following section.

Momentum Equations

$$\frac{\partial u}{\partial t} + u\frac{\partial u}{\partial x} + v\frac{\partial u}{\partial y} + w\frac{\partial u}{\partial z} - fv = -\frac{\partial p}{\partial x} + \frac{\partial}{\partial x}\left(\nu^h \frac{\partial u}{\partial x}\right) + \frac{\partial}{\partial y}\left(\nu^h \frac{\partial u}{\partial y}\right) + \frac{\partial}{\partial z}\left(\nu^v \frac{\partial u}{\partial z}\right) \quad \textbf{(53)}$$

$$\frac{\partial v}{\partial t} + u\frac{\partial v}{\partial x} + v\frac{\partial v}{\partial y} + w\frac{\partial v}{\partial z} + f = -\frac{\partial p}{\partial y} + \frac{\partial}{\partial x}\left(\nu^h \frac{\partial v}{\partial x}\right) + \frac{\partial}{\partial y}\left(\nu^h \frac{\partial v}{\partial y}\right) + \frac{\partial}{\partial z}\left(\nu^v \frac{\partial v}{\partial z}\right) \quad \textbf{(54)}$$

$$\frac{\partial w}{\partial t} + u\frac{\partial w}{\partial x} + v\frac{\partial w}{\partial y} + w\frac{\partial w}{\partial z} = -\frac{\partial p}{\partial z} + \frac{\partial}{\partial x}\left(\nu^h \frac{\partial w}{\partial x}\right) + \frac{\partial}{\partial y}\left(\nu^h \frac{\partial w}{\partial y}\right) + \frac{\partial}{\partial z}\left(\nu^v \frac{\partial w}{\partial z}\right) \quad \textbf{(55)}$$

Continuity Equation

$$\frac{\partial u}{\partial x} + \frac{\partial v}{\partial y} + \frac{\partial w}{\partial z} = 0 \quad \textbf{(56)}$$

Free-surface equation by integrating equation **(56)** over depth and using a kinematic condition at the free surface (Casulli and Cheng 1992):

$$\frac{\partial \eta}{\partial t} + \frac{\partial}{\partial x}\left[\int_{-h}^{\eta} u dz\right] + \frac{\partial}{\partial y}\left[\int_{-h}^{\eta} v dz\right] = 0 \quad \textbf{(57)}$$

Radiation boundary condition at open boundaries:

$$\frac{\partial \eta}{\partial t} + \frac{\partial}{\partial x}\left[\int_{-h}^{\eta} u dz\right] + \frac{\partial}{\partial y}\left[\int_{-h}^{\eta} v dz\right] = \frac{\eta^* - \eta}{\tau_r} \quad \textbf{(58)}$$

η^*	specified water level
τ_r	Problem-specific relaxation time

Transport Equation

The diffusivity of the transport equation is connected to the turbulent viscosity by the turbulent Schmidt number (valid for very small particles):

$$\sigma_t = \frac{\nu_t}{\kappa_t} \cong 1 \rightarrow \nu_t \cong \kappa_t \tag{59}$$

For a first assumption the rheological viscosity will not be considered for the diffusivity in the transport equation, i.e. equation (59) is not changed. As a reason the following quote is given:
"The effect of increasing turbulence or increasing rheological viscosity is the same of the Navier-Stokes equation, i.e. damping of the current velocity. However, with regard to the diffusion of suspended particles, the level of mixing is increased by turbulence but reduced by an increase of rheological viscosity." (Wehr 2012, p. 52)

$$\frac{\partial C}{\partial t} + \frac{\partial (uC)}{\partial x} + \frac{\partial (vC)}{\partial y} + \frac{\partial [(w - w^s)C]}{\partial z} = \frac{\partial}{\partial x}\left(K^h \frac{\partial C}{\partial x}\right) + \frac{\partial}{\partial y}\left(K^h \frac{\partial C}{\partial y}\right) + \frac{\partial}{\partial z}\left(K^v \frac{\partial C}{\partial z}\right) \tag{60}$$

Related water density

$$\rho = \rho(C) \tag{61}$$

Pressure components

$$p(x,y,z,t) = p_a(x,y,t) + g[\eta(x,y,t) - z] + g\int_z^\eta \frac{\rho - \rho_0}{\rho_0} d\zeta + q(x,y,z,t) \tag{62}$$

Momentum Equations

$$\frac{\partial u}{\partial t} - fv = -\frac{\partial p_a}{\partial x} - g\frac{\partial \eta}{\partial x} - g\frac{\partial}{\partial x}\left[\int_z^\eta \frac{\rho - \rho_0}{\rho_0} d\zeta\right] - \frac{\partial q}{\partial x} + \frac{\partial}{\partial x}\left(\nu^h \frac{\partial u}{\partial x}\right) + \frac{\partial}{\partial y}\left(\nu^h \frac{\partial u}{\partial y}\right) + \frac{\partial}{\partial z}\left(\nu^v \frac{\partial u}{\partial z}\right) \tag{63}$$

$$\frac{\partial v}{\partial t} + fu = -\frac{\partial p_a}{\partial y} - g\frac{\partial \eta}{\partial y} - g\frac{\partial}{\partial y}\left[\int_z^\eta \frac{\rho - \rho_0}{\rho_0} d\zeta\right] - \frac{\partial q}{\partial y} + \frac{\partial}{\partial x}\left(\nu^h \frac{\partial v}{\partial x}\right) + \frac{\partial}{\partial y}\left(\nu^h \frac{\partial v}{\partial y}\right) + \frac{\partial}{\partial z}\left(\nu^v \frac{\partial v}{\partial z}\right) \tag{64}$$

$$\frac{\partial w}{\partial t} = -\frac{\partial q}{\partial z} + \frac{\partial}{\partial x}\left(\nu^h \frac{\partial w}{\partial x}\right) + \frac{\partial}{\partial y}\left(\nu^h \frac{\partial w}{\partial y}\right) + \frac{\partial}{\partial z}\left(\nu^v \frac{\partial w}{\partial z}\right) \tag{65}$$

For hydrostatic approximation equation **(65)** is neglected and $q = 0$ is assumed.

Boundary Conditions

Momentum Equations

free surface (wind stresses)

$$\nu^v \frac{\partial u}{\partial z} = \gamma_T(u_a - u)\ ,\ \nu^v \frac{\partial v}{\partial z} = \gamma_T(v_a - v)\ , at\ z = \eta \tag{66}$$

sediment-water interface (bottom friction)

$$\gamma_B = r_B\sqrt{u^2 + v^2} \tag{67}$$

Transport Equation

free surface

$$\kappa^v \frac{\partial C}{\partial z} - (w - w^s)C = \alpha_T + \beta_T(C_T - C), at\ z = \eta \tag{68}$$

sediment-water interface

$$-\kappa^v \frac{\partial C}{\partial z} + (w - w^s)C = \alpha_B + \beta_B(B - C), at\ z = -h \tag{69}$$

A list of **assumptions and approximations** that have been introduced into the formulation of the conceptual model UnTRIM (Casulli and Lang 2004, p. 17):

1. continuous medium assumption,
2. incompressibility approximation,
3. Reynolds-averaged Navier-Stokes equations (RANS),
4. Boussinesq approximation,
5. eddy-viscosity concept,
6. Coriolis parameter,
7. parameterization of bottom friction,
8. parameterization of wind friction, and
9. no fluid-sediment interaction.

11.4 Concentration, solid content, bulk density

concentration c_S [kg/m^3], solid content Φ_S[-], bulk density ρ_B [kg/m^3](Wehr 2012, S. 7)

$$c_S = \rho_S\,\Phi_S \rightarrow \Phi_S = \frac{c_S}{\rho_S}$$

$$\rho_B = \rho_W + \left(1 - \frac{\rho_W}{\rho_S}\right) c_S = \Phi_S\rho_S + (1 - \Phi_S)\rho_W = \Phi_S(\rho_S - \rho_W) + \rho_W$$

12 Historic development of the Ems Estuary

12.1 Anthropogenic influences in the history of the Ems Estuary

The main anthropogenic influences in the Ems estuary can be found in the second half of the 20th century. However, also earlier interventions should be considered. In the following, some important ones will be mentioned.

12.1.1 Before the 19th century

In Wildvang (1937) a very early state of the Ems is described, possibly around year 0, before the "invasion of the North Sea", where the mouth of the estuary and the wadden sea was formed (Janssen 1968; Wildvang 1937). This is shown in Figure 63.

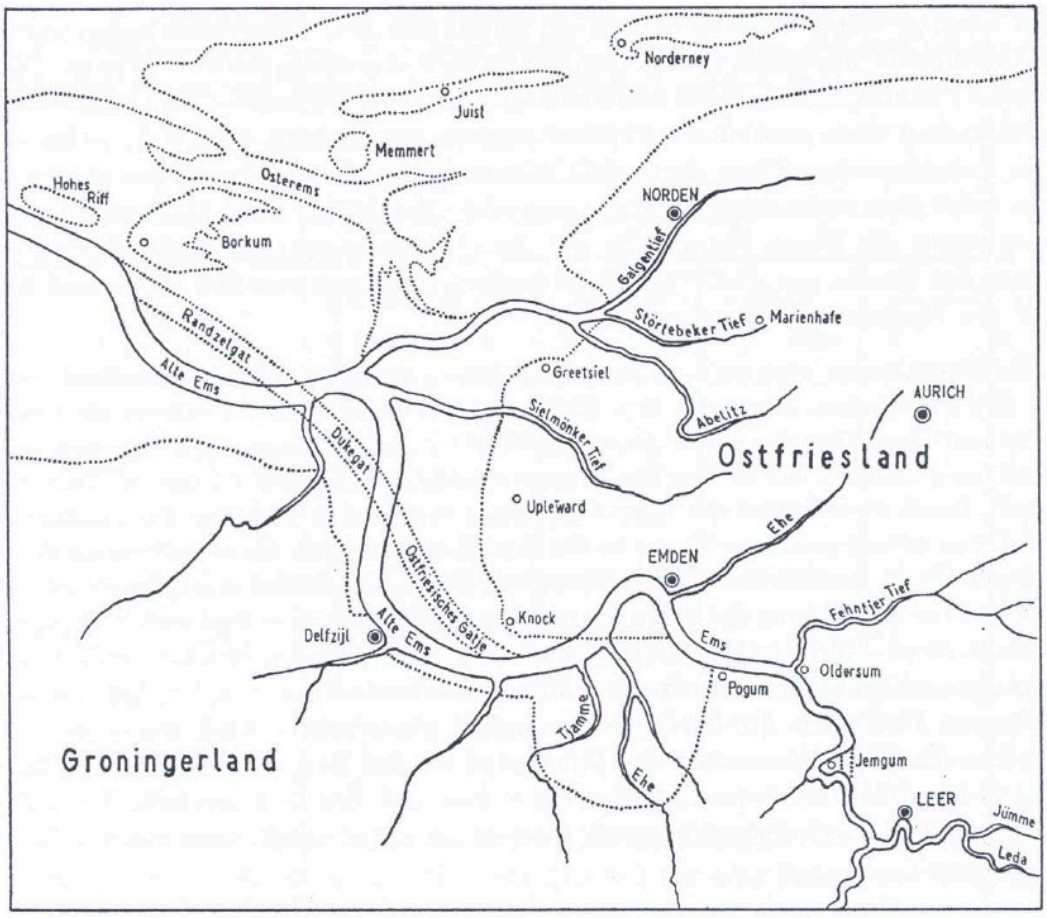

Figure 63: The mouth of the Ems before the "invasion of the North Sea", dotted line: extent in 1937 (Wildvang 1937).

In the 10th or 11th century the first settlements with a harbor infrastructure developed in the area of Emden. The Dollard, a bay south of Emden, possibly developed due to the Marcellus flood in 1362 and reached its largest area after a heavy storm tide in 1509. Already in the 15th century dykes were built for reclamation of the land around the Dollard. The development of the Dollard area is shown in Figure 64 (Krebs and Weilbeer 2008; Schubert 1970).

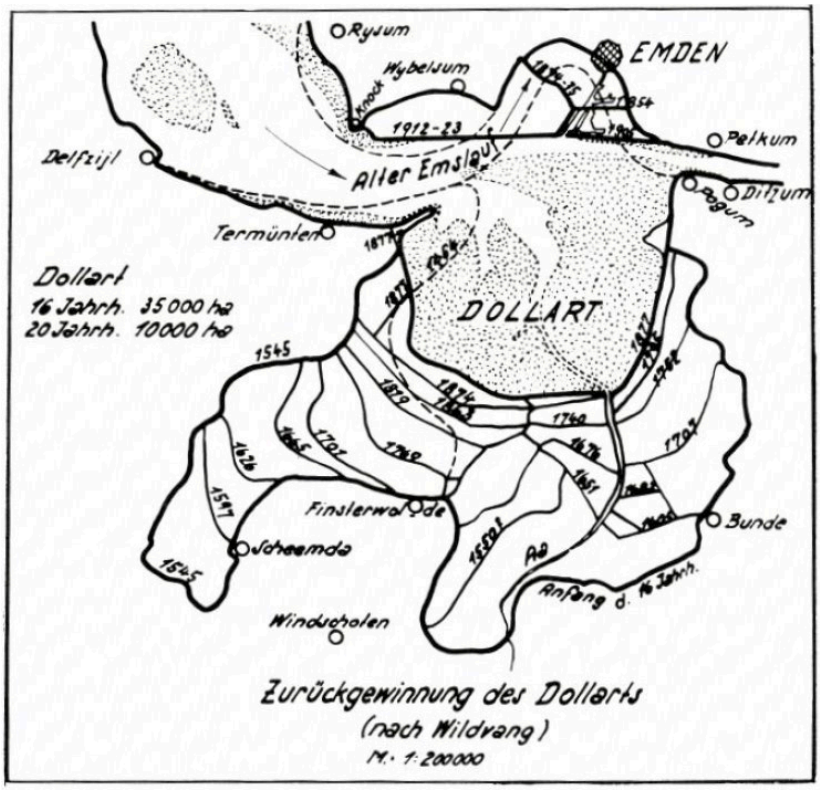

Figure 64: Development of the Dollard (Schubert 1970).

The Leybucht (near Norden, see Figure 65) developed around the same time due to storm tides in 1374 and 1378. The island Nessersand was also formed by the storm tide of 1509, creating an avulsion of the meander at Emden (see Figure 63 and "Alter Emslauf" in Figure 64). Figure 65 shows the state of the Outer Ems estuary in 1580 (Krebs and Weilbeer 2008).

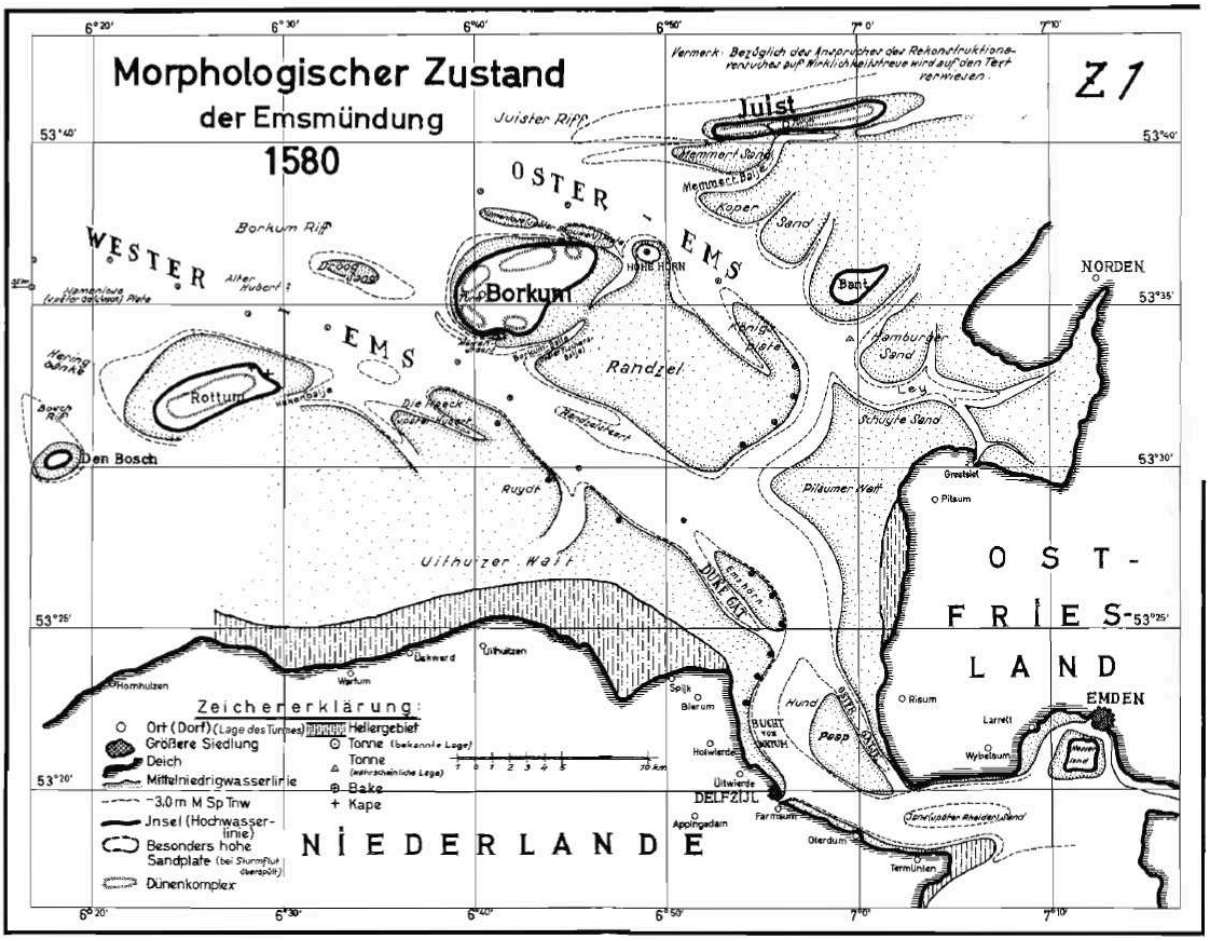

Figure 65: Morphological state of the Outer Ems in 1580 (Lang 1954).

12.1.2 19th century

In 1860 the lower Ems began to be canalized and from 1870 to 1899 the Geiseleitdamm (Geise training wall) was constructed (Krebs and Weilbeer 2008; Schubert 1970; Herrling and Niemeyer 2008c).

Between 1892 and 1899 two meanders in the lower Ems at Tunxdorf and Rhede were avulsed, further straightening the river (Figure 66). The first weir in Herbrum (Figure 67, "Altes Wehr") was finished in 1899 in the course of the construction of the Dortmund-Ems-canal between Dortmund and Papenburg.

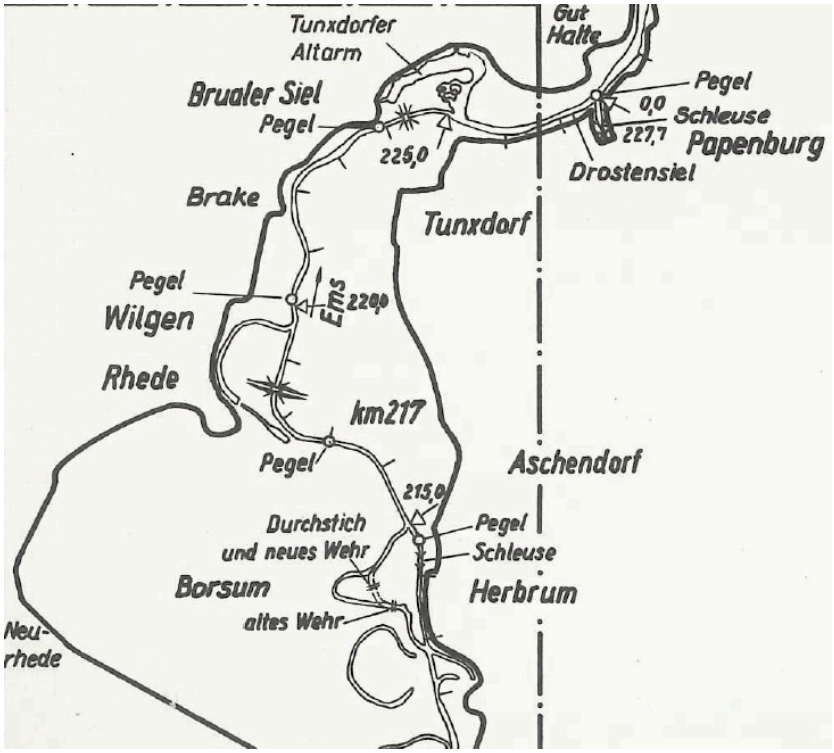

Figure 66: The lower Ems between Papenburg and Herbrum in 1954 (Hensen 1954).

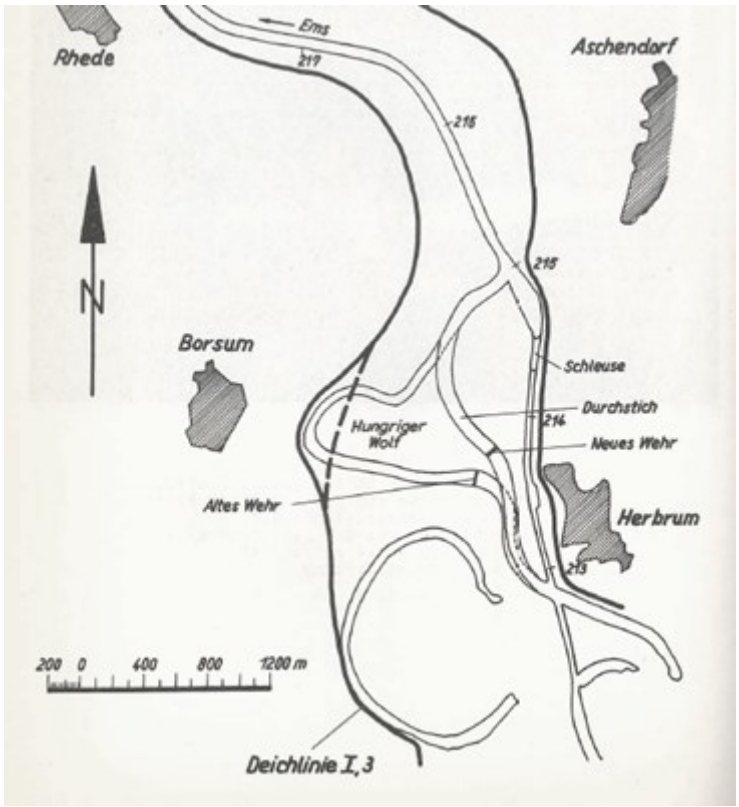

Figure 67: The old and new weir in Herbrum (Hensen 1954, Heft 6c, Figure311, 1954, Heft 6c, Figure 311).

Also in the Outer Ems a development has taken place, as can be seen when comparing Figure 65 and Figure 68. The islands Rottum, Borkum and Juist have deformed and moved, the connection between Westerems and Osterems became stronger and Nessersand almost vanished. (Lang 1954; Janssen 1968)

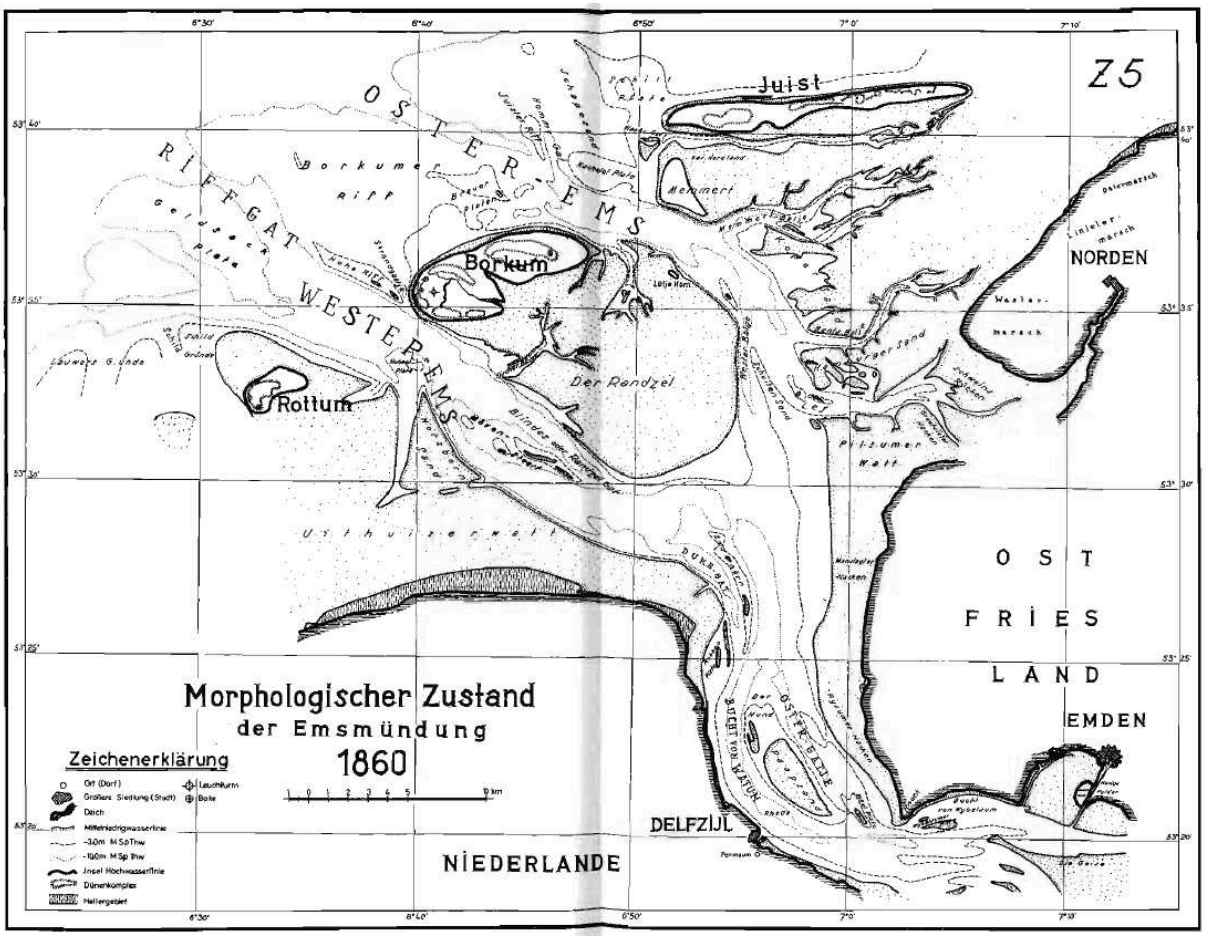

Figure 68: Morphological state of the Outer Ems in 1860 (Lang 1954).

12.1.3 First half of the 20th century

In the 19 hundreds then the main deepening and canalization took place. The Gatjebogen was deepened for the opening of the sea port Emden in 1901, also fully closing the meander at Emden. 1913 the large sea lock was finished, protecting the port from the tide. Between 1911 and 1929 a depth of -5.00 m MHW was assured between Emden and Leer and -4.00 to -4.50 m MHW between Leer and Papenburg (Krebs and Weilbeer 2008; Schubert 1970).
In 1911 (Mark-Hilkenborg), 1925 (Pottdeich) and 1928 (Coldam) further meanders were avulsed, as shown in Figure 69 (Herrling and Niemeyer 2008c).

In the 1930s a dam was built at Knock, later forming the Rysumer Nacken. The Geiseleitdamm was enforced, the Gatjebogen further deepened and the channel was deepened to -7.00 m SKN in the Outer Ems, -5.50 m MHW between Pogum and Leer and -4,20 m MHW between Leer and Papenburg (Krebs and Weilbeer 2008; Schubert 1970).

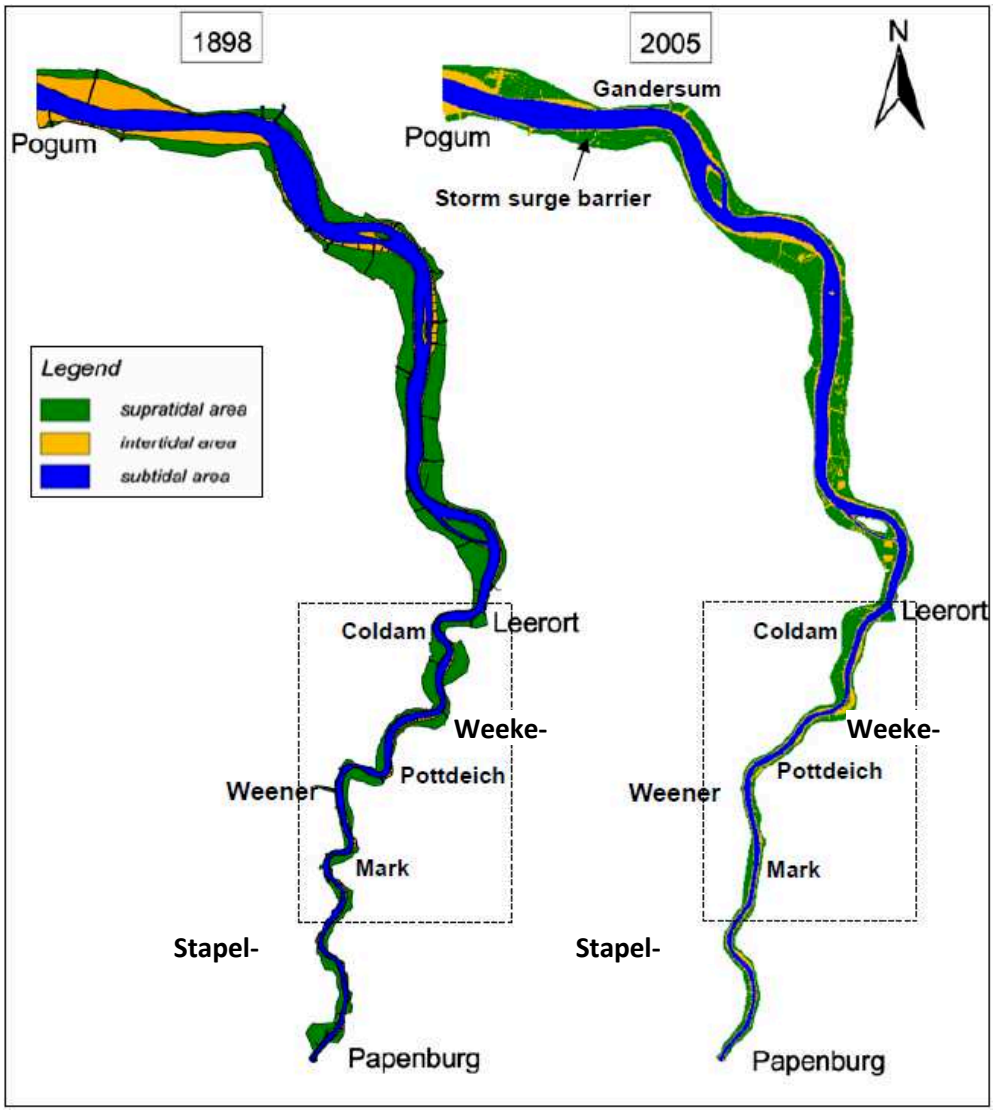

Figure 69: Straightenings between Pogum and Papenburg from 1898 to 2005 (Herrling and Niemeyer 2008c).

12.1.4 Second half of the 20th century until 1980

After 1950 even more severe changes were made. 1954 the Leda barrage was finished, 1958-1961 the Geiseleitdamm was connected and lengthened and the channel in the Outer Ems was further deepened (Emden: -8.00 m SKN, Outer Ems: -8.50 m SKN, seaward: -12.50 m SKN) (BAW 2010).

Winter dykes were built between Papenburg and Herbrum in the 50's and 60's. Therefore the meander at Herbrum was avulsed and a new weir had to be built as can be seen in Figure 67 ("Neues Wehr"). Also a second chamber was added to the lock in Herbrum. (Wasser- und Schifffahrtsamt Meppen; Eckholdt et al. 1998; Hensen 1954; Grabau 2004)

In 1968 construction began for the deep-sea port of Delfzijl, being finished in '73 including a new entry at Oterdum. This new entry made the dredging of the bight of Watum redundant, which

was therefore stopped. The port of Eemshaven opened in 1973 and the port of Emden was also extended in the 70's (Groningen Seaports 2015; Krause and Hoogland 1995).

1968 and '69 a sewer and a pumping station were built at the southern edge of the Rysumer Nacken. Before that the dykes surrounding it were closed and filled with dredged material from the ems (G. Klaassen 2018).

12.1.5 After 1980

At the end of the 20th and in the first years of the 21st century the last major changes took place. In 1984 the last sections of the lower ems were straightened, mainly in the area of Weekeborg and Stapelmoor (see Figure 69). Furthermore the lower Ems was once again deepened, to -5.70 m MHW in 1985/85 and to -6.30 m MHW in 1991 between Emden and Papenburg (maintenance depth). After that the lower Ems was only deepened further when a ship from the shipyard in Papenburg had to be transferred (demand depth). The maximum depth was set to -6.80 m in 1991 and -7.30 m MHW in 1994 (BAW 2010; Lange 2006; Krebs and Weilbeer 2008).

Starting in 1998 the Luke ("Langfristiges Unterhaltungskonzept Ems", long-term maintenance concept Ems), a program to stabilize the sediment transport in the lower Ems, was implemented (BAW 2010).

The Emssperrwerk, a large barrage near Gandersum, was taken in operation in 2001. It is used to protect the river from higher storm surge levels caused by the straightening and deepening of the river, but also to dam up the river if necessary for deep going (Herrling and Niemeyer 2008c; Talke and de Swart 2006).

12.1.6 21st century

After the construction of the Emssperrwerk in 2001, not many large projects have been realized. Some of the ports have been extended. The storm surge barrier also allowed the river to be dammed up in order to enable even deep-going ships to pass from the shipyard in Papenburg out to the sea. (Herrling and Niemeyer 2008c)

In that time it was not accepted anymore, that the ecological condition of the Ems estuary had changed. The sediment concentrations increased, while the oxygen levels decreased severely. Therefore, dredging and straightening/deepening activities have been considered critically and projects like the "Masterplan Ems 2050" on the German side and "Eems Dollard 2050" in the Netherlands have been initiated.

12.2 Dredging

In order to provide the respective depths in the channel, maintenance dredging is necessary in the Ems. One focus lies on the brackwater zone in the Emder fairway, but also in the outer and lower Ems regions sediment transport makes dredging necessary.

Figure 70 shows dredging volumes between 2000 and 2014. The amount dredged from the Outer Ems is much larger than in the lower Ems due to the turbidity zone in the Emder fairway but also since here mostly maintenance dredging is conducted every two to four weeks. The depth maintained is called *maintenance depth*. From 1945 to 1994 the dredged material was dumped at agricultural sites on land and on the Rysumer Nacken. However, due to high costs and ecological concerns, later the material was dumped on sea dumping sites, leaving the material in the estuarine system (Krebs and Weilbeer 2008).

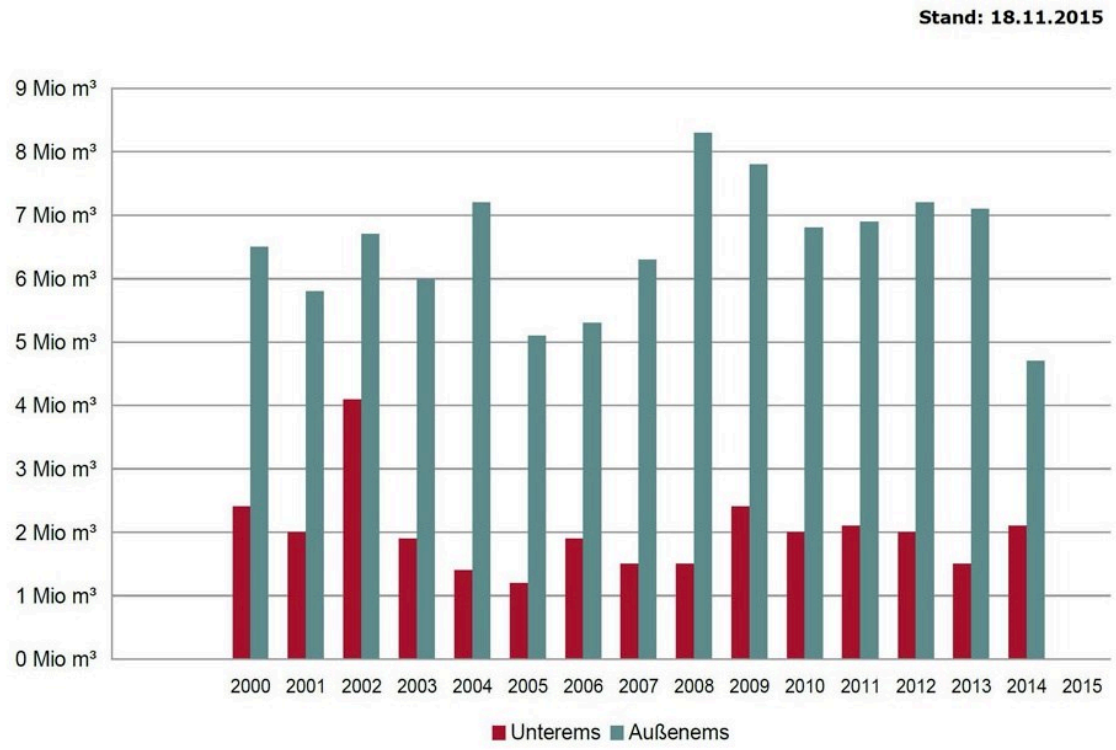

Figure 70: Dredging amounts in the lower and Outer Ems from 2000 – 2014 (Wasser- und Schifffahrtsamt Emden 2015).

Before the 1990s also in the Emder fairway and port a lot of sediment was dredged and dumped on land. Thus, the sediment was taken out of the system, before it could reach the lower Ems (Winkel 2017).

The lower Ems, however, is mainly dredged as needed when, for example, a deep-going vessel from Papenburg has to be transferred. This is called *demand depth*. By these occasional dredgings, also the maintenance depth in the lower Ems can be provided. The material upstream of Leer is mainly dumped on dumping sites on land, downstream it is brought to dumping sites in the estuary. Since the construction of the storm surge barrier, the lower Ems can also be dammed up in order to provide water depths necessary for the transfer of deep-going yard ships and thus less dredging is necessary (Krebs and Weilbeer 2008).

A more detailed history of dredging amounts in the lower Ems is also shown in Figure 71, including a few major reasons.

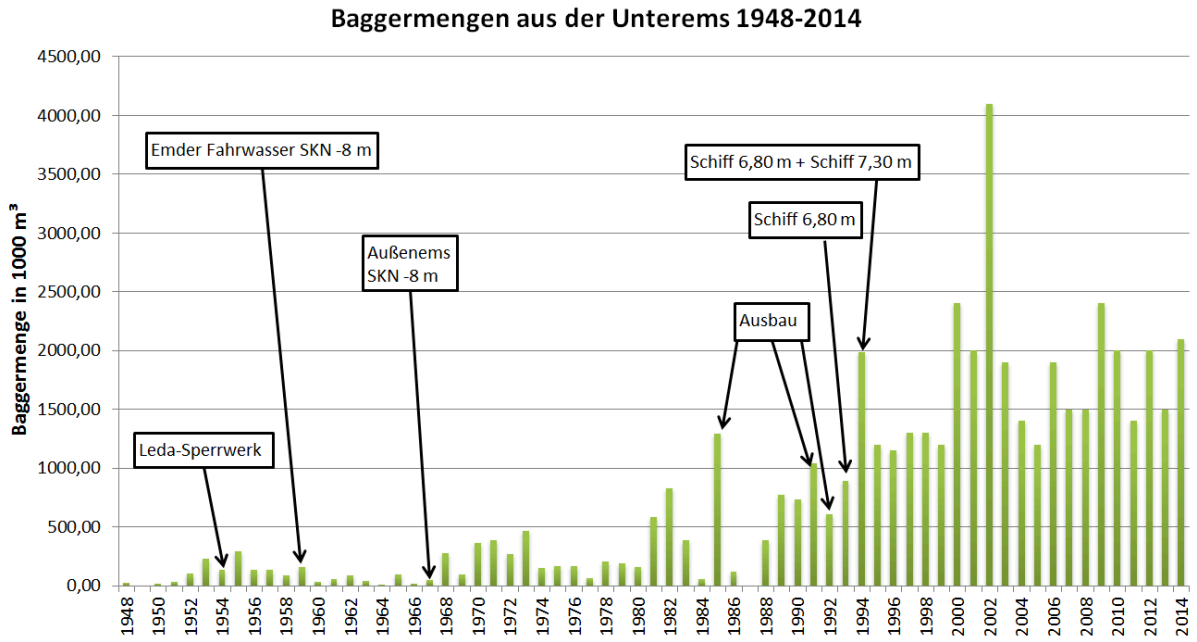

Figure 71: Dredging volumes from the lower Ems between Herbrum and Emden from 1948 to 2014 and major interventions.
(data from Wasser- und Schifffahrtsamt Emden 1995, 2015; Lange 2006)

Mainly due to dredging and deepening, the depth of the fairway in the Ems estuary has changed immensely. But not only the depth, but also the alignment of the river was modified, straightening and widening it. This results in a development of the channel depths in the lower Ems shown in Figure 25. There it can be seen, that the differences between the depth profiles from 1992 to 2015 are small compared to the difference between 1981 and 1992, when major deepening has taken place.

12.3 Hydrological measurements

12.3.1 Discharge

The discharge at Versen (last gauge before the beginning of the estuary) is usually used to estimate the discharge at Herbrum (model boundary and tidal barrier). The discharge at Herbrum is assumed to be approximately 10 % higher than at Versen due to accumulation from the catchment area.

Furthermore the rivers Leda and Jümme (flow into the Ems at Leer) as well as Westerwoldsche Aa (inflow into the Dollard) add discharge to the estuarine system and are included in the model. The mean discharge has not changed significantly during the last 70 years. The discharge between 1941 and 2014 can be seen in Figure 72, the peaks being winter discharge values. The yearly hydrograph is typical, with high discharges in winter and low discharges in the summer months (Krebs and Weilbeer 2008).

High and low (mean) discharges for 1941-2014 are listed in Table 6.

Furthermore, the water level and discharge at Versen were evaluated for the chosen simulation time (Section 8.3.2, Figure 37). The discharge is only available starting in 1951, the water level is also available earlier.

Table 6: Discharge at Versen 1941-2014 (Gewässerkundliches Jahrbuch 2014; Deutsches Gewässerkundliches Jahrbuch 1951)

		1941-1950	1951	1981	2014	1942-2014
NQ [m³/s]	Low water discharge	5.2	9.6	36.2	26.2	5.2
MNQ [m³/s]	Mean low water discharge	9.4				16.9
MQ [m³/s]	Mean discharge	74.2	80.1	146	59.9	79.3
MHQ [m³/s]	Mean high water discharge	439				360
HQ [m³/s]	High water discharge	1200	295	539	147	1200

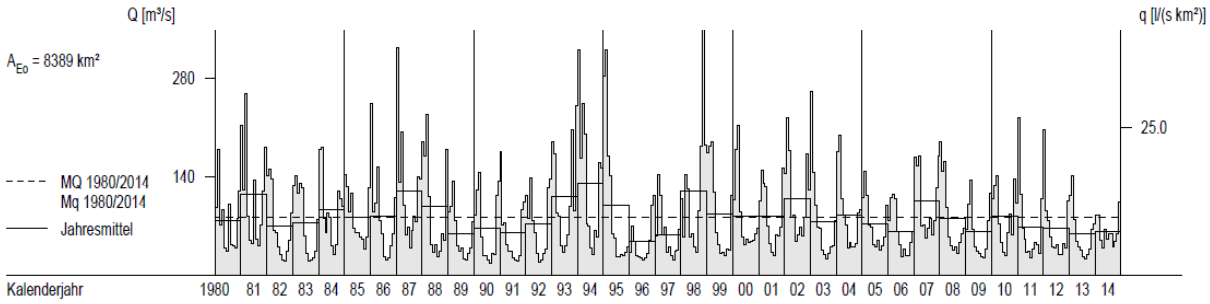

Figure 72: Discharge at Versen 1941-2014 (Gewässerkundliches Jahrbuch 2014).

Jensen et al. (2003) investigated the correlation between the mean low water in the estuary and the mean discharge at Versen. They regarded three different time spans, from 1936-1959, 1962-1980 and 1986-1999, separating the time into spans with similar correlations. The results are shown in Table 7 and Figure 73. They found, that the mean low water decreased by about 34 cm at Papenburg and 66 cm in Herbrum between 1958 and 1962 due to the enlargement measures. (Jensen et al. 2003)

Table 7: Correlation between MLW (estuary) and MQ (Jensen et al. 2003)

	increase of MLW	time span
Herbrum (Ems)	1.2 cm per 1 m³/s at Versen	1936 to 1965
	1.4 cm per 1 m³/s at Versen	1962 to 1980
	1.1 cm per 1 m³/s at Versen	1986 to 1999

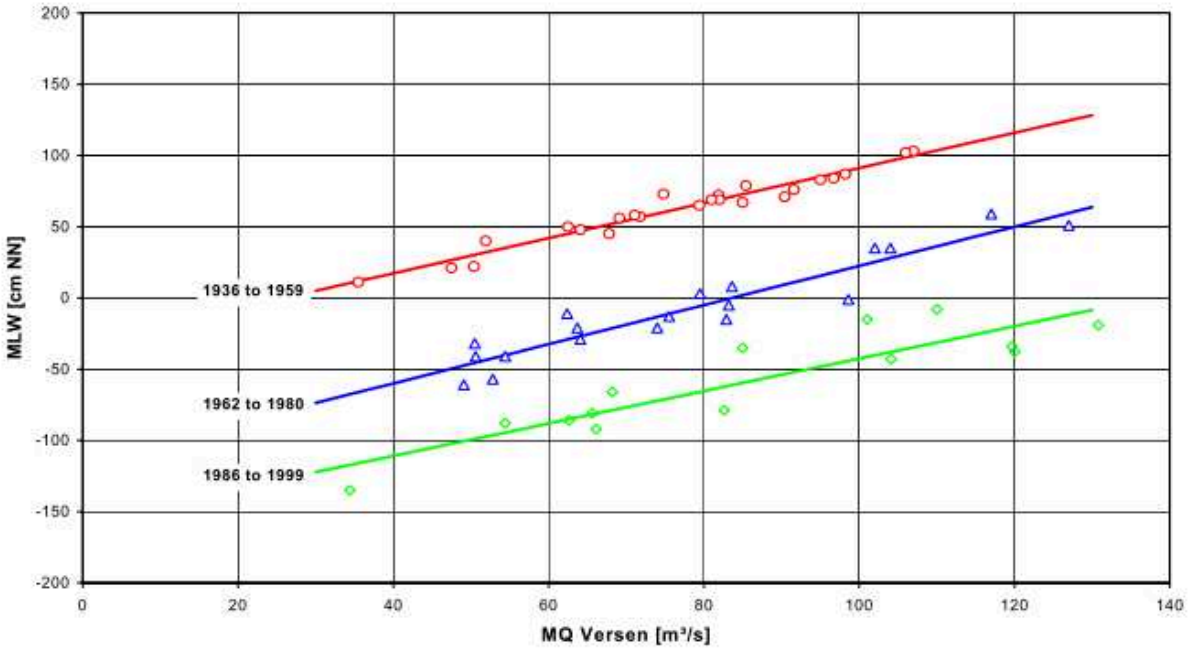

Figure 73: Correlation between MLW (estuary) and MQ between 1936 – 1999 (Jensen et al. 2003).

12.3.2 Sea level

Jensen et al. (2003) describes a mean sea level rise of approximately 0.01 cm/year for the mean low water and approximately 0.30 cm/year for the mean high water between 1942 and 1999. He evaluated data for gauges in the North Sea at Borkum, Helgoland, List and the Lighthouse "Alte Weser".

Figure 74 shows the yearly average of the measured water levels at Huibertgat (since the 70's), Eemshaven (since 1980), Delfzijl (since 1880) and Nieuwe Statenzijl (since 1980). All curves show a very similar increase in the mean water level around the sea boundary and inlet of the Ems estuary of more or less 0.2 m from 1880 to 2017. This would correspond to 0.14 cm/year, which is of the same order of magnitude as the values from Jensen et al. (2003), considering that here all water levels are averaged.

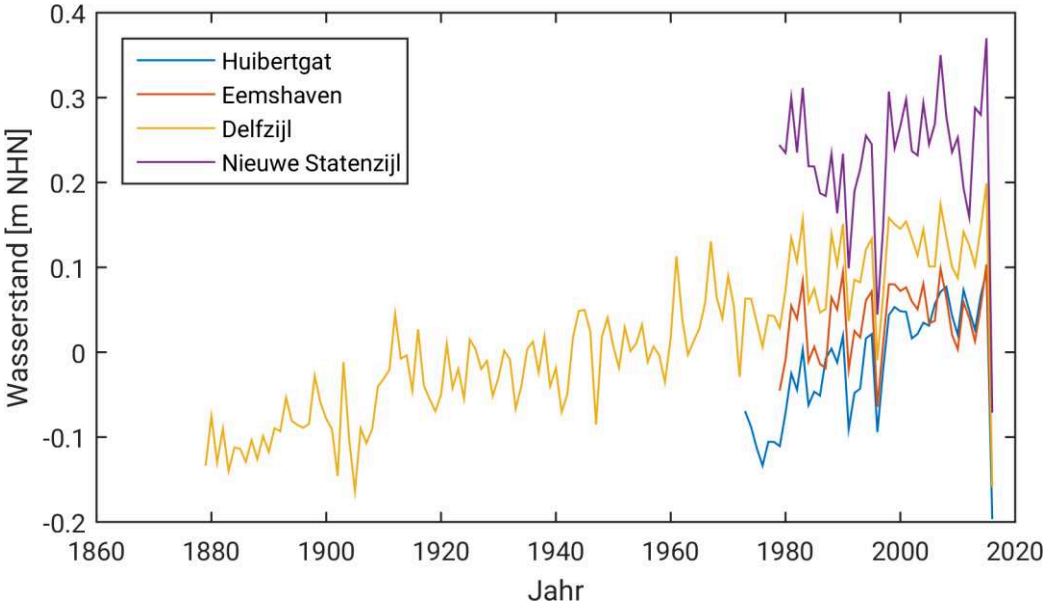

Figure 74: Measured yearly averaged water levels at the Ems inlet since 1880.

12.3.3 Tidal characteristics

The mean tidal range along the complete German coastline is shown in Figure 75. It can be seen, that from the 50's, the development changed. Before, the mean tidal range was more or less constant, while after that time, it increased strongly by about 25 cm in 50 years.

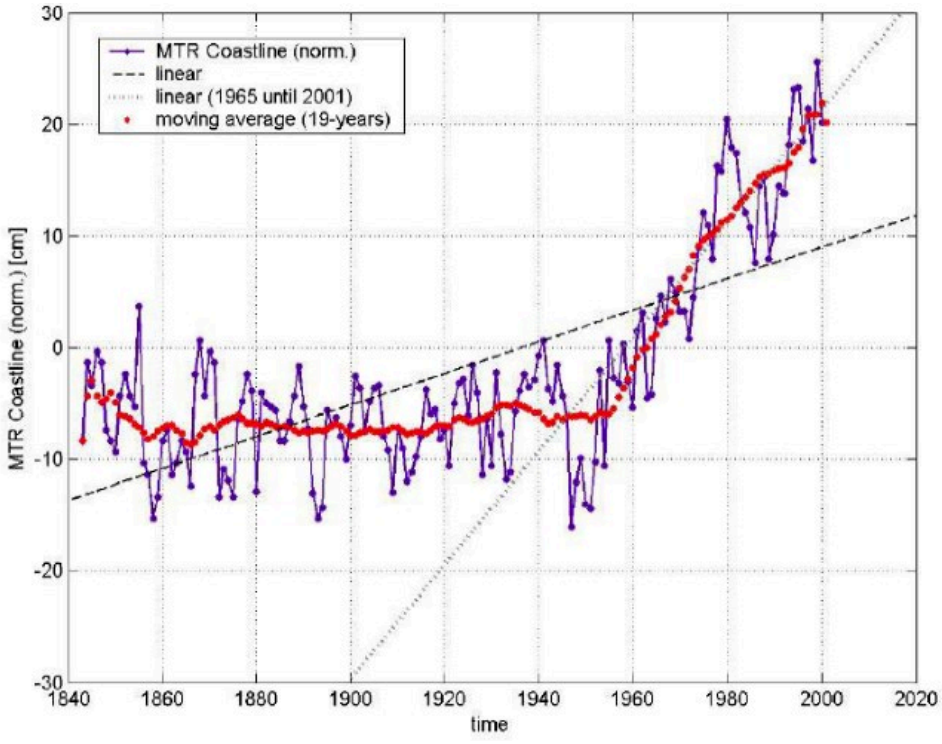

Figure 75: Mean tidal range observed at tidal gauges along the German coastline. The red line is a 19 year average. Adapted from Jensen and Mudersbach, 2005 by (Talke and de Swart 2006).

Therefore, this development is not just estuary specific, but can be observed across all of the North Sea and is not yet completely explained (Talke and de Swart 2006).

Figure 76 shows the yearly averaged high and low water levels at Borkum since the beginning of their recording in 1935. It can be observed, that, as mentioned by Jensen et al. (2003), the mean high water level (MHWL) rises more than the mean low water level. The MHWL increases by approximately 0.25 cm/year, which also is of a similar magnitude as mentioned by Jensen et al. (2003).

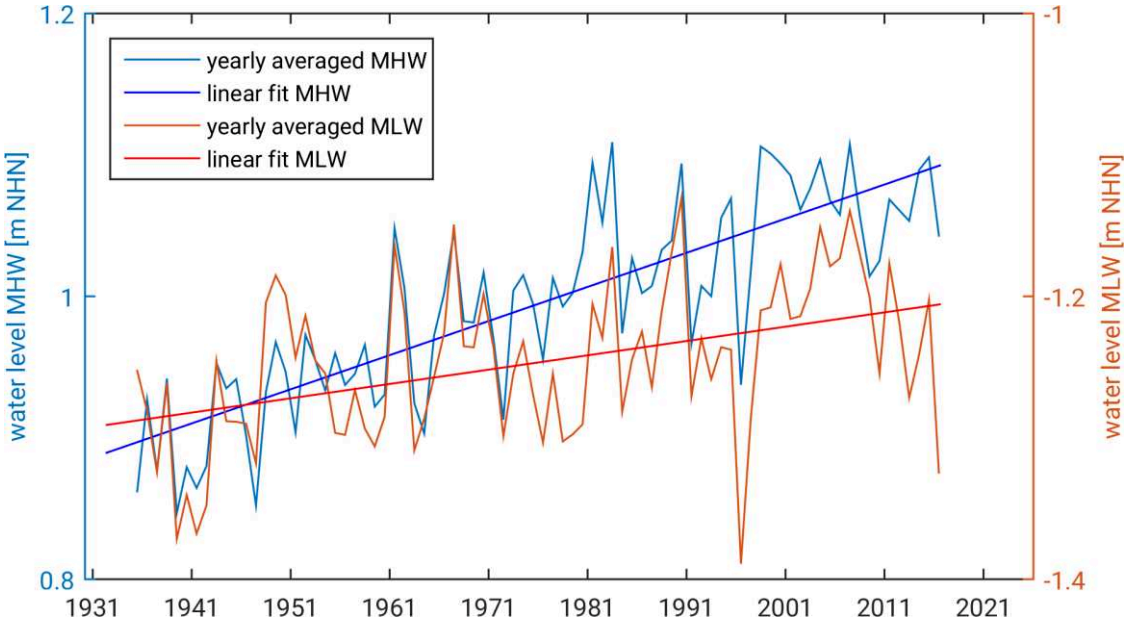

Figure 76: Measurements of MHW and MLW at Borkum 1935 – 2016.

The tidal range also varies within a spring-neap-cycle. This is presented in Figure 77. It shows the tidal range calculated from measurements of high and low water levels in the years 1958, 1981 and 2015 as well as the full and new moon in 2015. It shows the increased tidal range from 1958 until 2015, but also an increased spring-neap variability. While in 1958 the difference between spring tidal range and neap tidal range is between 0.5 and 1 m, in 2015 it is between 1 and 1.5 m. However, the lower tidal ranges in 2015 around neap tide are still higher than the tidal range in 1958, even at spring tide.

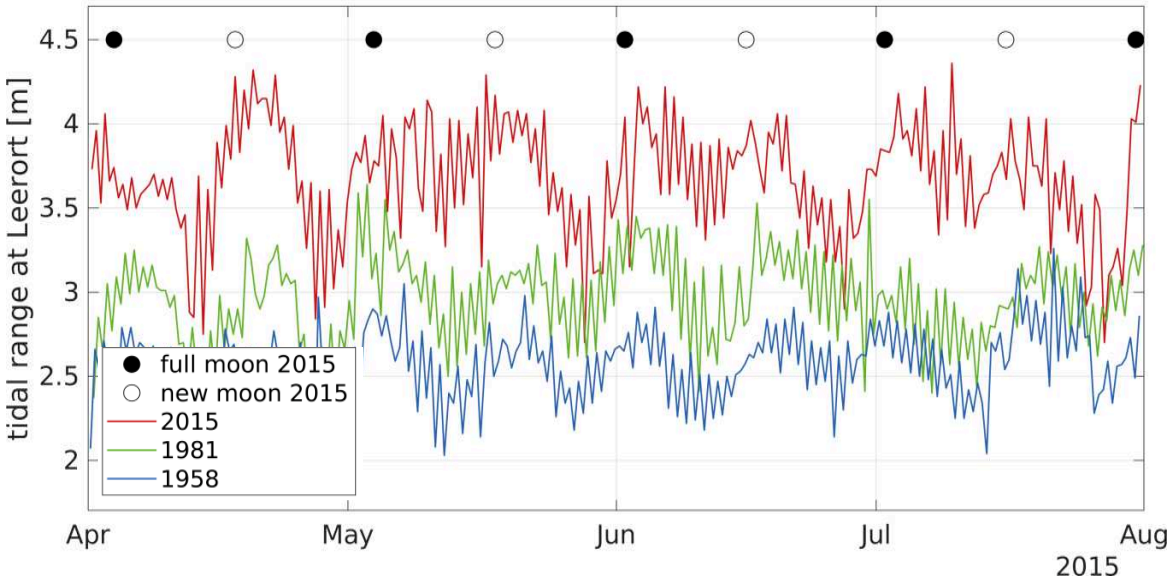

Figure 77: Measured tidal range at Leerort between April and August.

Besides the tidal range, also the propagation time of the tide has changed over the years. Krebs 2015 summarized the seasonal variations of several hydrological parameters. The historical development of the tidal range was also investigated, as shown in Figure 78. It is clearly visible, that the propagation time from Borkum to Papenburg decreased by about 100 % between 1950 and 1968 (~ 200 minutes) and 2000-2014 (~ 100 minutes). This can be explained by the straightening and deepening of the river, but also by the increased formation of fluid mud, causing the reduced bottom roughness.

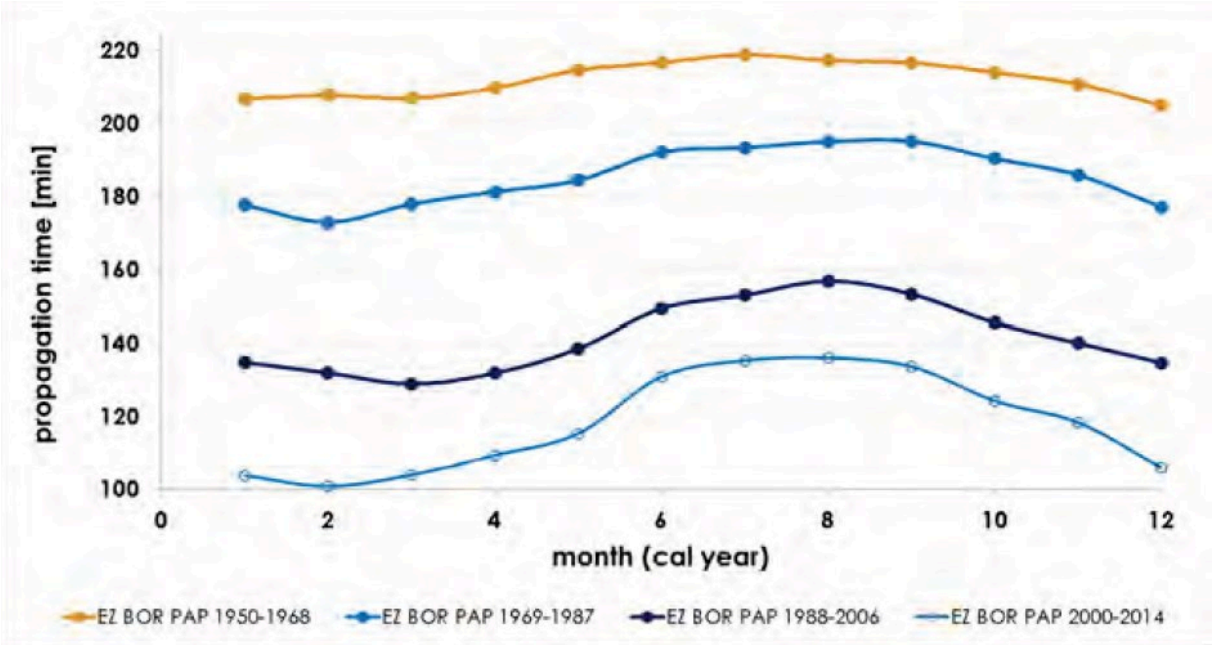

Figure 78: Development of the propagation time from Borkum to Papenburg from 1950 to 2014 (Krebs 2015).

12.3.4 Development of the salinity

Franzius (1986) describes a “present state” (meaning the state of 1986) of the salinity in the Ems estuary, which can be seen in Figure 79. It shows the salinity at flood-tide reversals and with mean discharge.

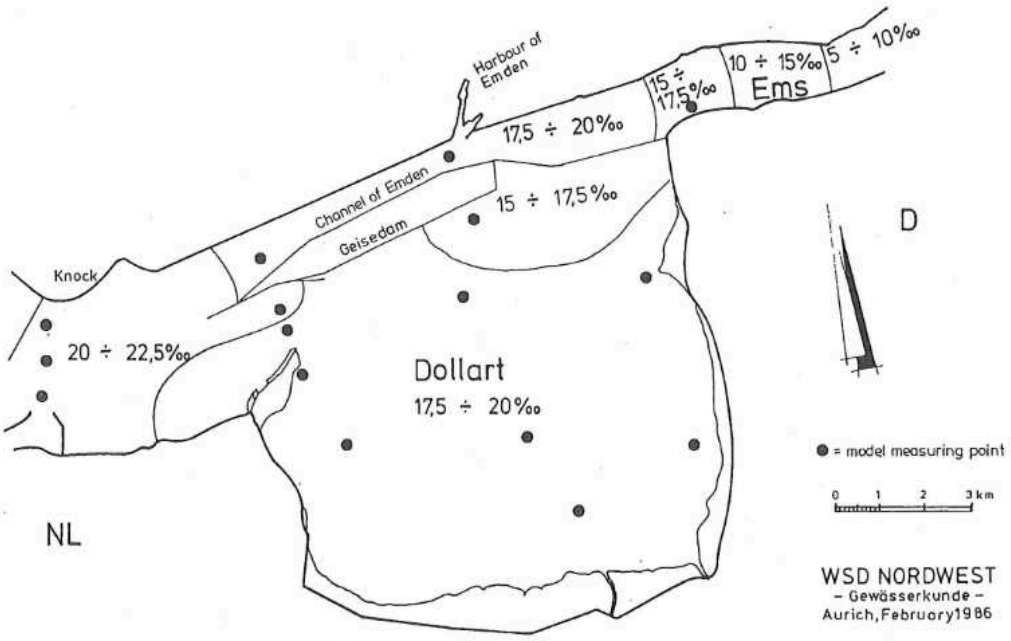

Figure 79: Salinity in the Dollard area in 1986 (Franzius 1986).

Engels (2015) presented developments of the salinity in the Lower Ems. The salinity at the measuring station Leer has increased rapidly since the beginning of the 21st century, as shown in Figure 80.

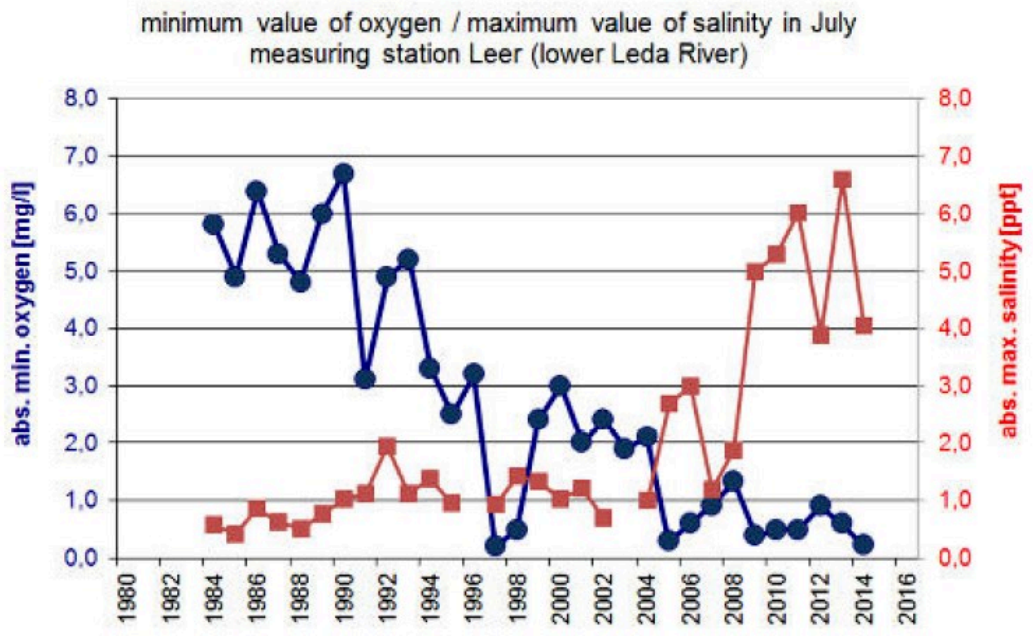

Figure 80: Development of salinity and dissolved oxygen at the measuring station Leer (Engels 2015).

Another aspect concerning the salinity is the brine discharge from natural gas caverns. Brine is pumped into the Ems estuary since the 1980's. Until 2013 brine was pumped into the estuary at Ditzum near the storm surge barrier. Later only fresh water was extracted there, while the brine was pumped in at Rysum (Engels 2017). The detailed consequences of this are not known, however the global influence on the hydrodynamics is expected to be insignificant.

12.3.5 Sediment concentration

At the same time, mainly since the amount of dredging increased, the soil composition changed. Uliczka (1997) described, how the soil on the riverbed changed from 1981 to 1996 from a sand and clay dominated bed to a mud dominated bed, as shown in Figure 81.

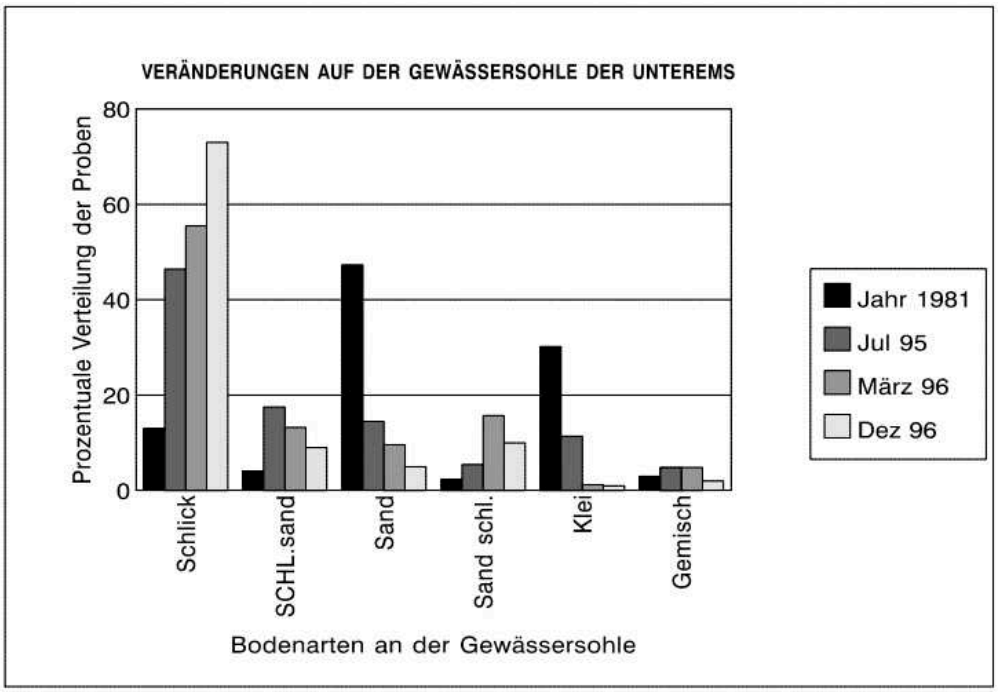

Figure 81: Changed in soil composition on the river bed between Papenburg and Emden 1981-1996, derived from soil mappings of the river bed (Uliczka 1997).

Borgsmüller et al. (2016) evaluated SSC measurements along the estuary from the 50's (not shown), late 70's/early 80's and 2013. The latter two are displayed in Figure 73.

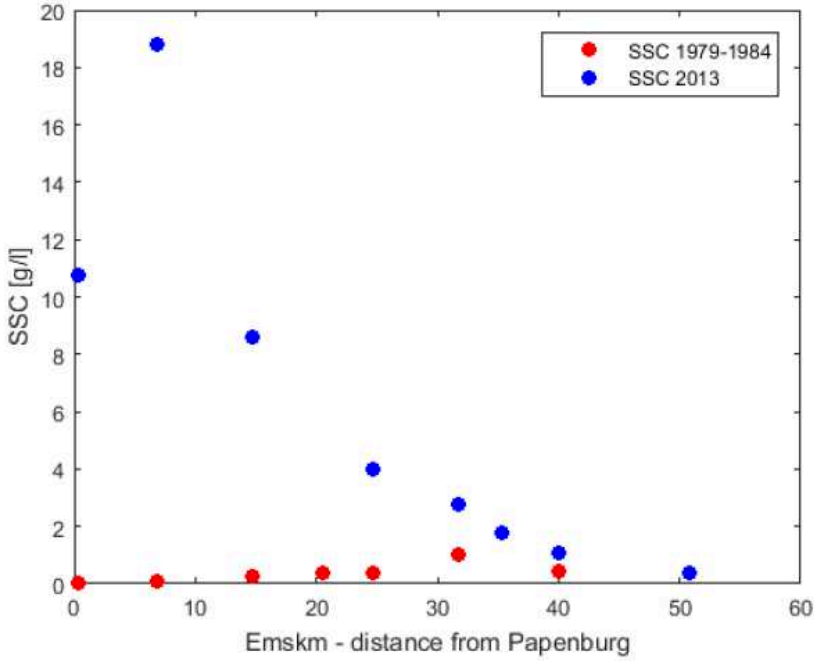

Figure 82: Longitudinal distribution of SSC along the tidal Ems between Papenburg (km 0,3) and Knock (km 50,1) for Q= 40 – 60 m^3/s based on data from WWA Aurich, NLWKN Aurich and BfG, reprinted from (Borgsmüller et al. 2016).

Furthermore, Jonge et al. (2014) collected measurements on bathymetry and SPM concentrations. Figure 83 shows longitudinal profiles of the mean annual suspended matter for the years 1954, 1975-1976, 1992-1993 and 2005-2006.

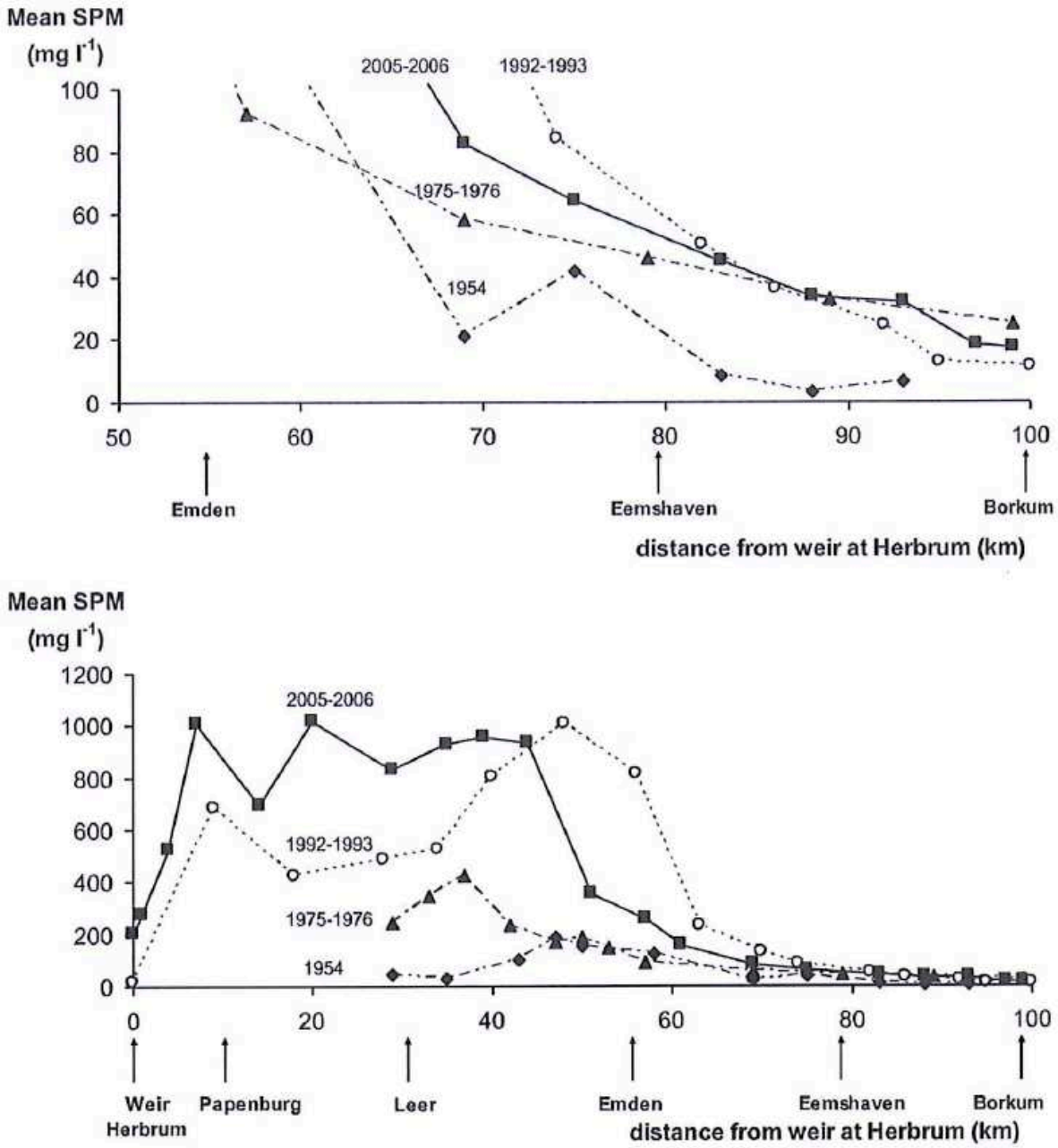

Figure 83: Longitudinal distributions of mean annual suspended matter since 1954 in the lower Ems (km 5 - 100) and the entire estuary from the weir to Borkum; reprinted from (Jonge et al. 2014).

Both Figure 82 and Figure 83, show a strong increase in SPM over the years with a greater influence in the Lower Ems.

The seasonal variation of discharge at Versen and SSC along the river is displayed in Figure 84 for 1992-1993 and 2005-2006. It shows that very high discharges are able to break up the regions of very high SSC quickly, while it takes a few months for them to reform in times of low discharges. In accord with the previous figures, the SSC values are much higher in 2005-2006 than they were in 1992-1993. This might, however, also be caused by the lack of really high discharges. In both time periods, double peaks can be observed at low discharge periods, with very high concentrations close to Herbrum and approximately 40-50 km from it (around Terborg).

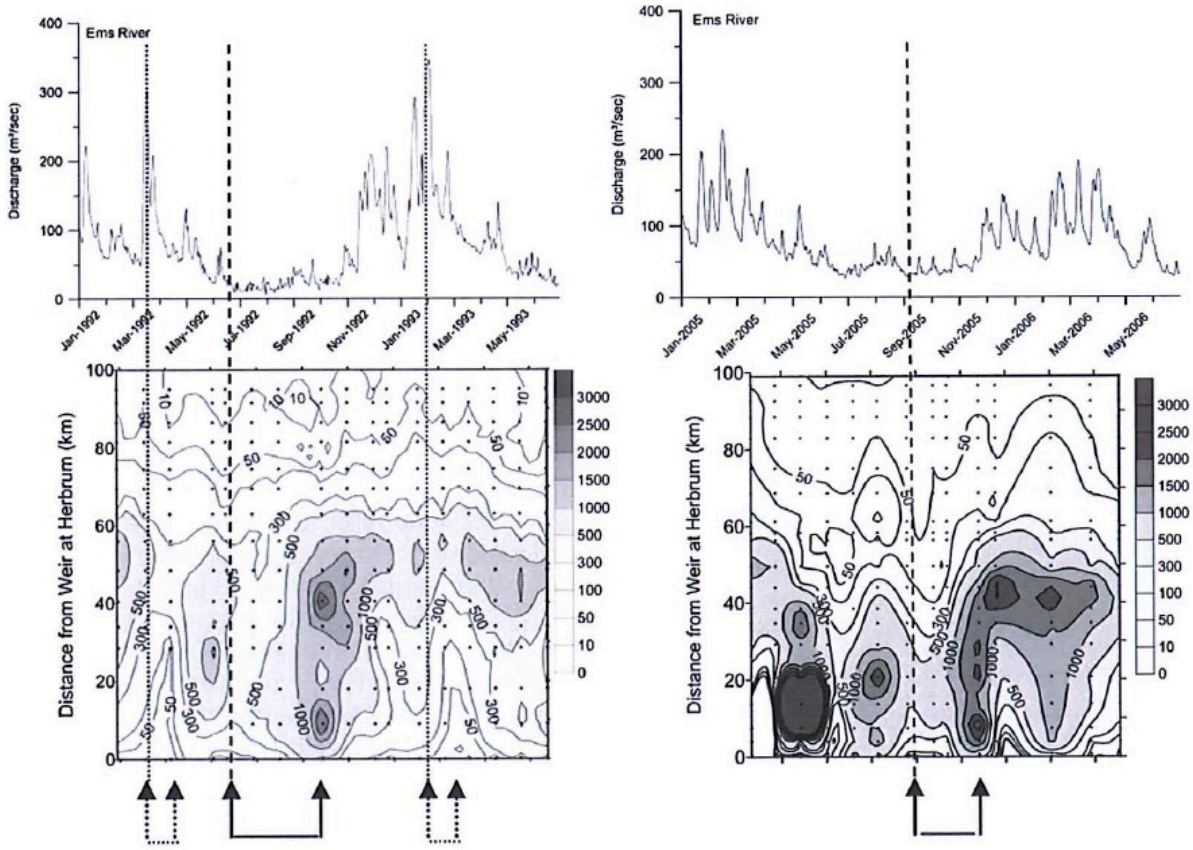

Figure 84: Seasonal variations in the Ems River discharge at Versen and the distribution of suspended matter between Borkum and Herbrum for 1992-1993 (left) and 2005-2006 (right), reprinted from (Jonge et al. 2014).

12.3.6 Oxygen

The increased sediment concentration has further effects, for example on the oxygen concentration. Between 1988 and 2005 the duration of oxygen minima (O_2 < 4 mg/l) has increased from nearly zero to up to 130 days per year in the lower Ems. (Uliczka 1997; Lange 2006)
Figure 80 also shows the dissolved oxygen level at Leer since 1984.

12.3.7 Further effects

Furthermore, the water quality has decreased rapidly. In 1993 the lower Ems upstream of Leer was categorized in the water quality category II according to the WRRL, which is exceptionally good, considering, that no other tidally influenced body of water has ever reached that category. However, starting in 1993, the conditions changed and in 2004 it is classified in category III-IV, due to the dying and migration of species caused by high suspended matter contents and low oxygen levels. The development is depicted in Figure 85 (Lange 2006).

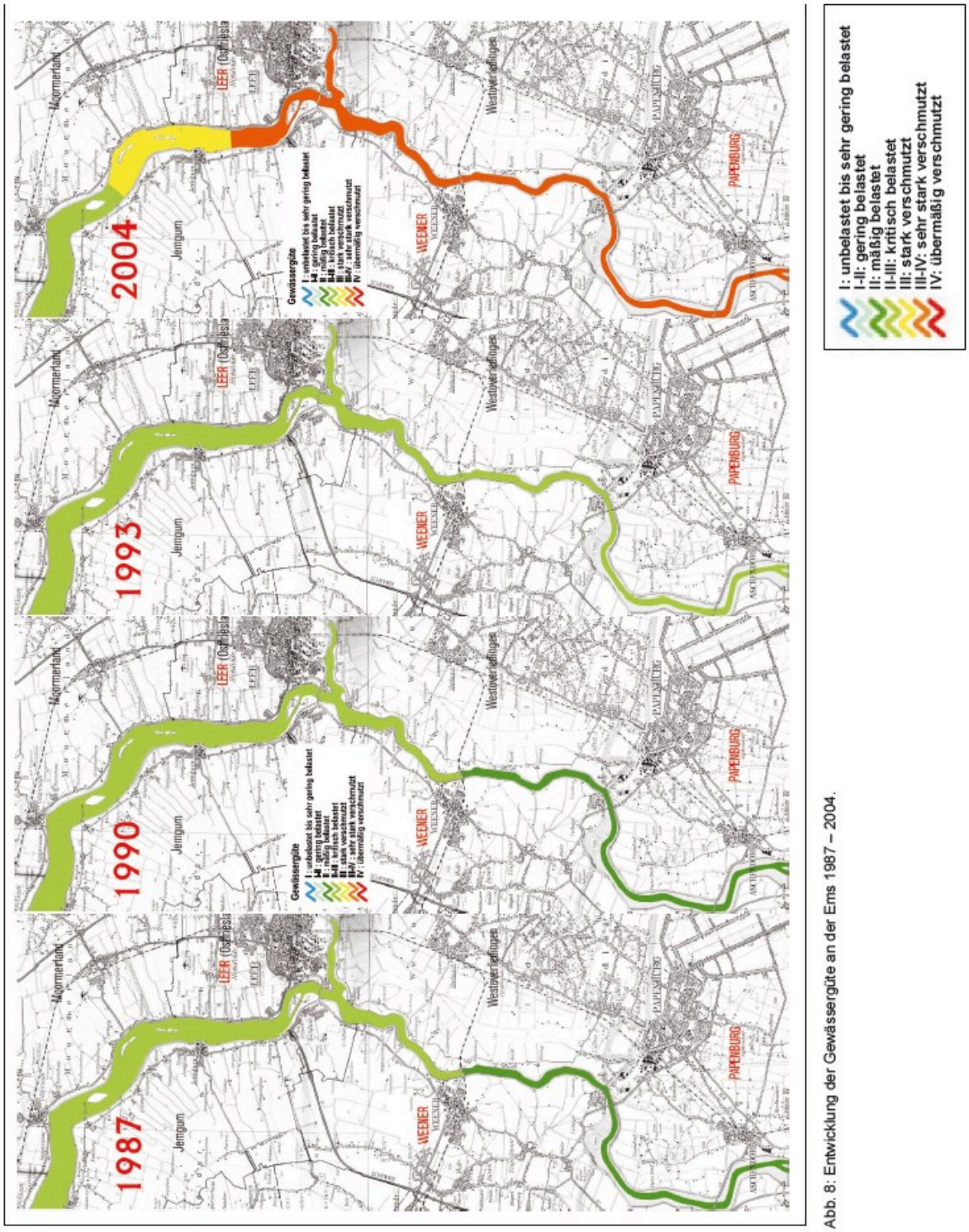

Figure 85: Development of the water quality 1987 – 2004 (Lange 2006).

BAW
Bundesanstalt für Wasserbau

Kußmaulstraße 17 · 76187 Karlsruhe
Tel. +49 (0) 721 97 26-0 · Fax +49 (0) 721 97 26-45 40

Wedeler Landstraße 157 · 22559 Hamburg
Tel. +49 (0) 40 81 908-0 · Fax +49 (0) 40 81 908-373

www.baw.de